SKB

TECHNICAL REPORT 90-45

Interim report on the laboratory and theoretical work in modeling the drained and undrained behavior of buffer materials

Lennart Börgesson

Clay Technology AB, Lund

December 1990

SVENSK KÄRNBRÄNSLEHANTERING AB
SWEDISH NUCLEAR FUEL AND WASTE MANAGEMENT CO

BOX 5864 S-102 48 STOCKHOLM

TEL 08-665 28 00 TELEX 13108 SKB S
TELEFAX 08-661 57 19

INTERIM REPORT ON THE LABORATORY AND THEORETICAL WORK IN MODELING THE DRAINED AND UNDRAINED BEHAVIOR OF BUFFER MATERIALS

Lennart Börgesson

Clay Technology AB, Lund

December 1990

Interim Report

on

The Laboratory and Theoretical Work in Modeling the Drained and Undrained Behavior of Buffer Materials

December 1990

Lennart Börgesson

Clay Technology AB
IDEON, 223 70 Lund

CONTENTS

SUMMARY

This report describes the continuous work of modeling the geotechnical properties of buffer materials. Some results of laboratory work with drained and undrained tests are described as well as the material models that these tests have yielded. The effective stress concept and its relevance is discussed. The technique to apply the models in calculations using the finite element program ABAQUS is described. Some calculations of laboratory verification tests are shown and the results compared. Finally two examples of scenario calculations are shown.

The work has led to three material models that can be used in ABAQUS calculations. All parameters for these models are not fully known and a continuation of the work is required. These models are not suitable for all situations and the relevance and need for further developments are presently investigated.

PREFACE

The work is part of the Swedish R&D for final disposal of nuclear waste and financed by SKB.

The ABAQUS calculations were performed at the office of FEMTECH AB in Västerås by Jan Hernelind in close cooperation with the author.

The laboratory work was done by Harald Hökmark, Ola Karnland, Stefan Backe and Torbjörn Sandén at Clay Technology AB in Lund. They have done the computer plottings as well. The hand made figures are drawn by Birgitta Hellström. The manuscript was edited by Irene Hansen.

The contributions from these persons are acknowledged as well as the support from Anders Bergström, SKB and Roland Pusch, Clay Technology AB.

SYMBOLS

ROMAN LETTERS

A	area
A_s	contact area
a	half the major axis in the CS model
B	bulk modulus
B_a	bulk modulus of air
B_s	bulk modulus of solid
B_w	bulk modulus of water
b	deviation factor in the effective stress theory
d	"cohesion" in the σ_j-p plane
e	void ratio
E	Young's modulus
F_a	attractive force
F_r	repulsive force
G_s	stiffness in sticks
K	parameter in the plastic models
M	tanβ for the critical state line
N	total force
n	factor describing the strain rate dependence
p	average stress or contact pressure
q	deviator stress
q_f	deviator stress at failure
S_r	degree of saturation
s^{el}	elastic stress path
s^{pl}	plastic stress path
u	pore water pressure
w	water ratio

GREEK LETTERS

α	parameter in CS model
α_w	coefficient of thermal exp. of water
α_s	coefficient of thermal exp. of solid
β	"angle of friction" in the σ_j-p plane
ε	strain
$\dot{\varepsilon}$	rate of strain
ε_e	elastic strain
ε_t	total strain
ε_y	yield strain
ϕ	angle of friction (in σ_n-τ plane)
ψ	angle of dilatancy
κ	porous bulk modulus
λ	parameter in CS model
ν	Poisson's ratio
ρ	bulk density
ρ_m	density at saturation
ρ_s	density of solid
ρ_w	density of water
ρ	total stress
ρ'	effective stress
σ_1	major principal stress
σ_2	intermediate principal stress
σ_3	minor principal stress
σ_j	von Mises' stress
σ_n	normal stress
τ	shear stress

1. INTRODUCTION

All Swedish concepts for disposal of radioactive waste involve a buffer and sealing material to protect the waste from external effects and prevent leakage. The principal buffer material candidate is sodium bentonite, but other clay materials, such as calcium bentonite and mixtures of bentonite and filler material, are considered as well.

The ultimate purpose of investigating the properties of the buffer material is of course to understand the processes in the buffer and the interaction between the buffer and the rock and canister and to be able to mathematically simulate processes and scenarios involving the buffer material. Such simulations can be used for performance calculations in the safety analyses and as sensitivity analyses for optimizations.

Investigations on the rheological properties of the buffer material, including water flow in the material, have been in progress for several years. The R&D program includes the following steps:

1. Development of a general rheological model applicable to:

   * Undrained total stress analyses
   * Drained total stress analyses
   * Effective stress analyses (incl. pore pressure)
   * Thermomechanical analyses
   * Influence of high temperature and saline pore water
   * Influence of clay type and additive mixtures

This step includes laboratory tests and applied theories on the performance of the material.

2. Verification tests

* Rock displacement
* Canister displacement
* Swelling tests
* Laboratory tests

This step includes laboratory small scale and large scale tests as well as field tests.

3. Calculations (ABAQUS)

* Development of material models in the finite element program ABAQUS
* Simulation of the verification tests to check and calibrate the material models and the program
* Applied calculations on the performance of the buffer

The research program aims at having complete verified material and calculation models at 1993.

This report will describe the status of the work today. It will show a conceptual model of the behavior of the buffer material according to the knowledge today. It will also show the models available and the relevance of these models.

The report will also show some laboratory test results leading to the conceptual model and some ABAQUS calculations of verification tests in order to illustrate the advantages and the disadvantages of the available models

Finally the report will present some examples of scenario calculations in order to illustrate the applicability of the models.

2. MATERIAL MODELS

The finite element program ABAQUS was considered at an early stage to be the program available that was best fitted for geotechnical calculations of the behavior of clay based buffer material. The program has many material models in its library and the program is well suited for modeling the complex non-linear elastic and plastic behavior of the extreme properties of bentonite based buffer material.

Three plasticity models are suited for describing the non-recoverable soil behavior:

Metal Plasticity
Drucker-Prager Plasticity
Critical State Plasticity

In some cases the simple Metal Plasticity model might be useful but the two most important elastic-plastic soil models that have been developed in the recent 30 years are the Drucker-Prager model and the Critical State model. They primarily describe the non-recoverable plastic behavior of the material and the conditions for yielding.

The recoverable elastic part of the behavior can be described in several ways:

Linear Elasticity
Porous Elasticity
Hypoelasticity
Hyperelasticity

The linear elasticity model might be useful in some cases together with the Metal Plasticity model but a model that seems to fit the behavior of buffer

materials very good is the Porous Elasticity model. The three plasticity models and the two first mentioned elasticity models will be shortly described in this chapter.

2.1 METAL PLASTICITY

For some calculations the simple Metal Plasticity model is sufficient. In this model the yielding starts at a defined value of Mises stresses (von Mises yield criterion):

$$\sigma_j = \frac{1}{\sqrt{2}}((\sigma_1-\sigma_3)^2+(\sigma_1-\sigma_2)^2+(\sigma_2-\sigma_3)^2)^{1/2} \qquad (2:1)$$

The stress-strain relation at yielding is described with a function:

$$\varepsilon_y = f(\sigma_j) \qquad (2:2)$$

The model is illustrated in Fig 2-1 which shows that yielding starts at one value of σ_j and failure occurs at another value independently of the total average stress p.

This model can only be used for water saturated clays which are exposed to quick undrained strains. As soon as the clay drains or is allowed to change volume, the average stress will change, which results in a change in yield stress.

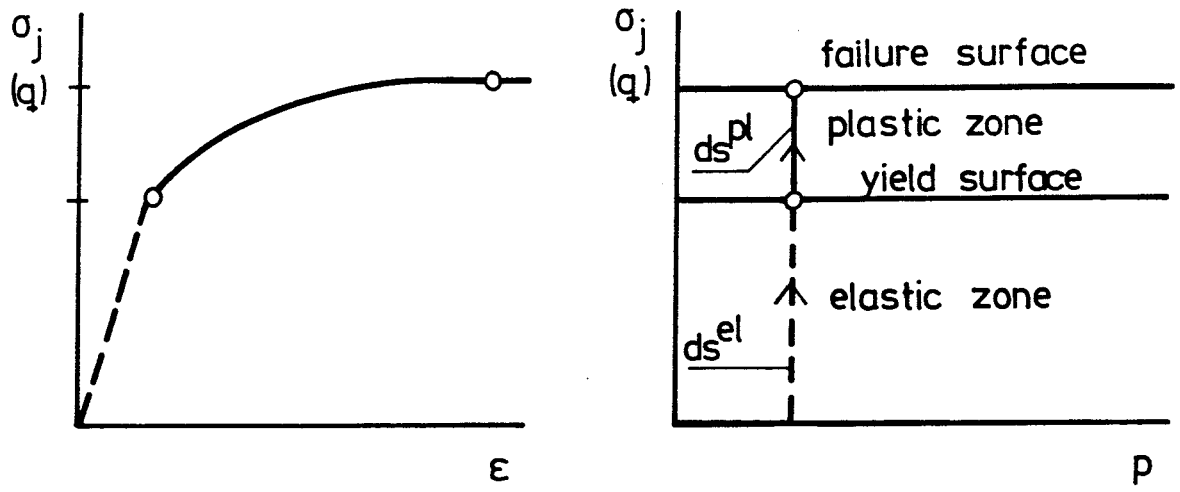

Figure 2-1: The Metal Plasticity model

2.2 DRUCKER-PRAGER PLASTICITY MODEL

In the Drucker-Prager model the influence of the average stress (friction angle $\phi \neq 0$) can be taken into account. A possible cohesion can also be simulated.

The model is illustrated in Fig 2-2 which shows that the stress dependence is caused by the "friction angle" β in the σ_j-p plane and the parameter d illustrating the "cohesion". If the plastic flow $d\varepsilon^{pl}$ is associated, the angle $\psi=\beta$ and the flow is perpendicular to the yield surface. In order to decrease the resulting dilation it can be necessary to assume non-associated flow by putting $\psi<\beta$.

When the stress path enters the plastic region ds^{pl} the yield surface is moved upwards until it reaches the failure surface.

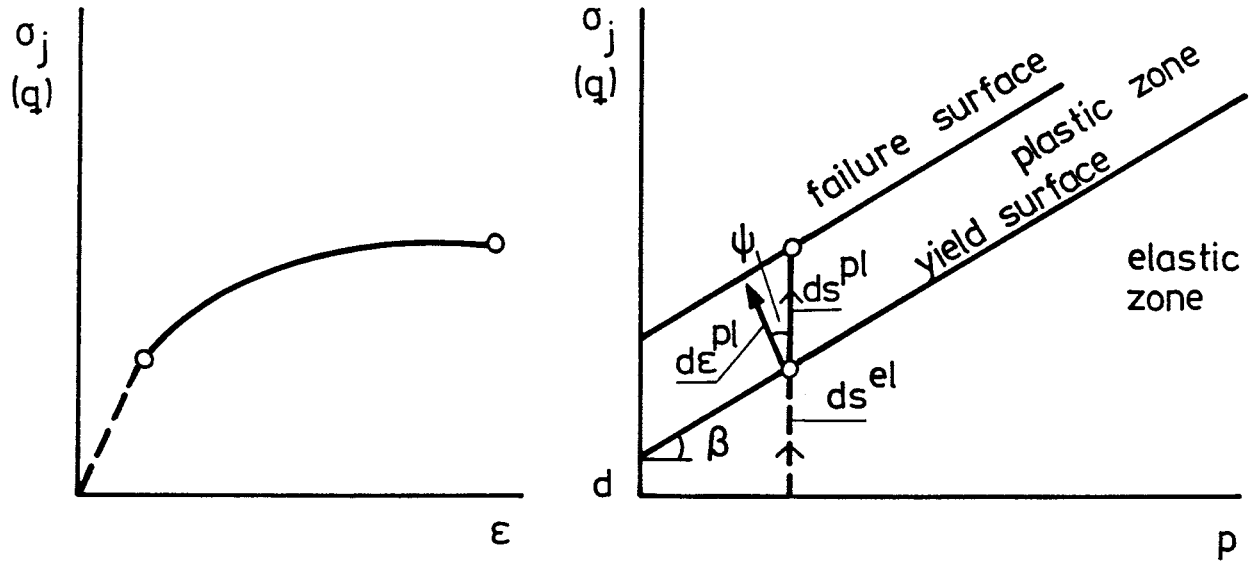

Figure 2-2: The Drucker-Prager model

The model also includes a constant K which controls the dependence of the yield surface on the intermediate principle stress. The yield surface is defined so that K is the ratio of the yield stress in triaxial tension to the yield stress in triaxial compression. The classical Drucker-Prager model is available when K=1.0 and ψ=β.

The parameters needed for the extended Drucker-Prager model are thus

β, d, K, ψ and the yielding function f

2.3 CRITICAL STATE PLASTICITY MODEL

While Drucker-Prager has a straight yield surface parallel to and always below the failure surface the critical state model includes an elliptic yield

surface which also can go above the original failure surface. The models that include such a yield surface are called cap models since the yield surface is limited in extension and can also be reached by isotropic compression. Fig 2-3 illustrates the model.

The critical state line is a failure line where the failure occurs without volume change. The plastic flow is always associated (normal to the yield surface). The yield surface is an ellipse inside which the behavior of the material is elastic. When the stress path reaches the yield surface the plastic flow begins and the yield surface starts changing its size.

Two types of plastic flow may occur in this model. If the stress path is located on the so-called wet side, illustrated by the upper half of Fig 2-3, the yield surface grows until it reaches the critical state line, where a smooth failure occurs. The material is then strain-hardening.

If, on the other hand, the stress path is located on the so-called dry side, illustrated by the lower part of Fig 2-3, the yield surface shrinks until it reaches the critical state line from above. The failure is then brittle with maximum shear stresses at maximum pure elastic strain, which is followed by plastic strain softening.

The critical state line passes through origo with the inclination $M=\Delta\sigma_j/\Delta p$, which means that there is no cohesion. The initial size of the yield surface must be determined. It is defined by the value of the parameter a_0, which is half the major axis in the ellipse on the "dry" side. While the form of the yield surface on this side is determined by the

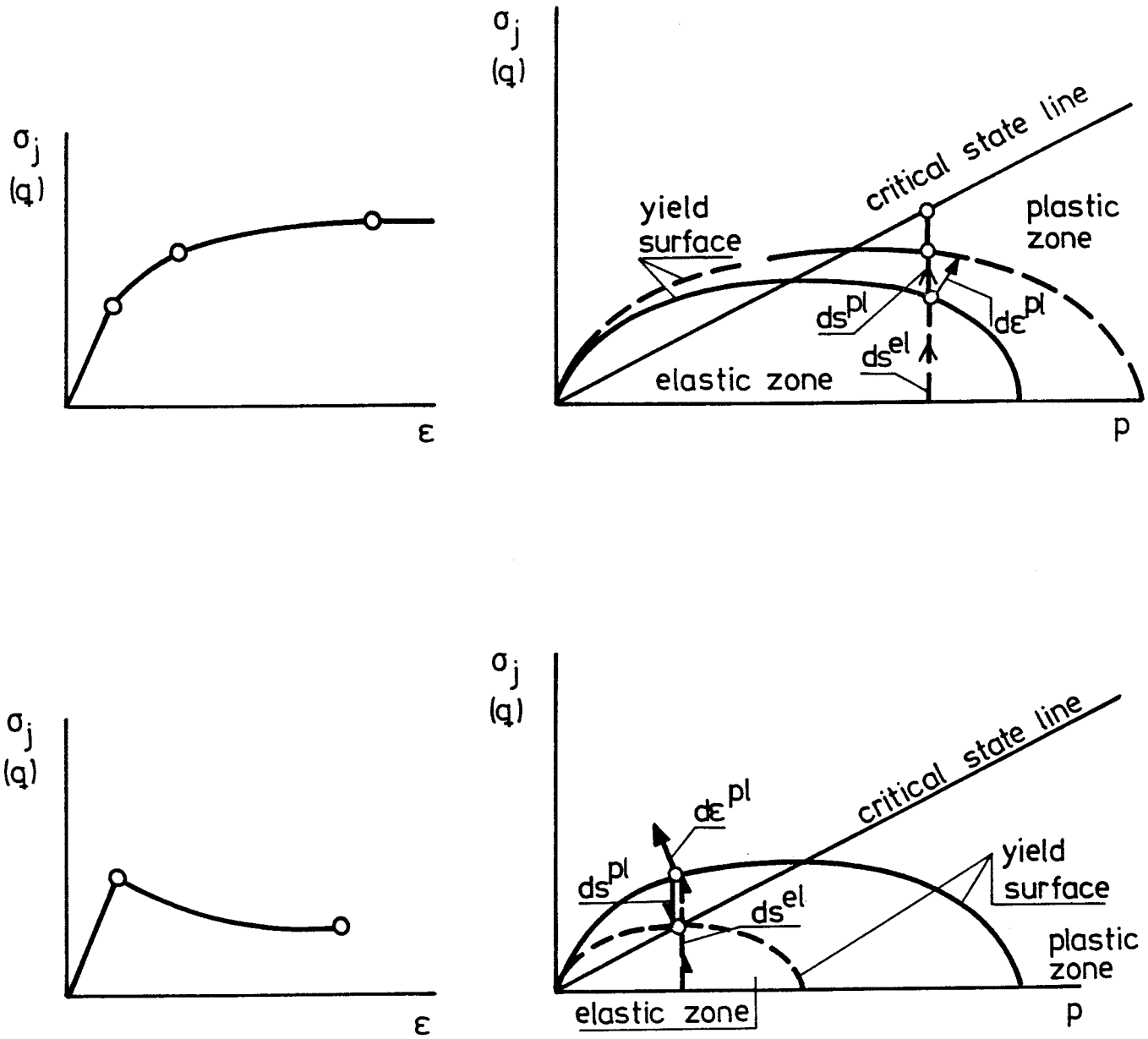

Figure 2-3: The Critical State model

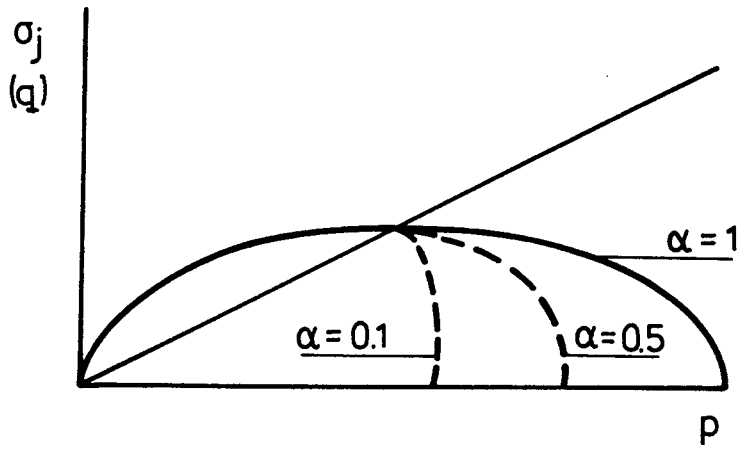

Figure 2-4: The shape of the yield surface on the wet side is a function of the parameter α.

M-value the model offers the possibility of changing the shape on the "wet" side. A factor $\alpha \leq 1.0$ can reduce the extension of the yield surface according to the examples in Fig 2-4. The model includes the factor *K* as well with the same meaning as in the Drucker-Prager model.

The volume change in the plastic zone is controlled by the inclination of the plastic strain, and a given relation between the void ratio *e* and the average stress *p*. *e* is assumed to be the straight line function of ln*p* implied by Eqn 2:3

$$e=-\lambda \ln p+A \qquad (2:3)$$

The inclination λ must thus be determined and given, while A is indirectly given by the position of the yield surface (a_0).

The equation of the yield surface is shown in Eqn 2:4

$$\frac{1}{\alpha^2}\left(\frac{p}{a}-1\right)^2+\left(\frac{t}{Ma}\right)^2-1=0 \qquad (2:4)$$

where initially $a=a_0$. $t=\sigma_j$ if $K=1$. $\alpha=1$ on the dry side of the yield surface.

The parameters needed for the Critical State model are thus:

M, a_0, α, K and λ

2.4 LINEAR ELASTICITY

Linear elasticity is the simplest form of elastic behavior. It can be modeled according to Eqn 2:5.

$$\sigma=D^{el}\varepsilon^{el} \qquad (2:5)$$

where σ is the total stress, D^{el} is the elasticity matrix and ε^{el} is the total elastic strain. If the material is isotropic only the two parameters Young's modulus E and Poisson's ratio ν are needed.

This model can be used together with the metal plasticity model and is only suitable for quick, undrained strain.

2.5 POROUS ELASTICITY

In a porous material, the volume or void ratio can be changed. The stress/void ratio relation can be modeled with the porous elasticity model in which the volumetric behavior is defined according to Eqn 2:6

$$\frac{\kappa}{1+e_0}\ln(p_0/p) = J^{el}-1 \qquad (2:6)$$

where
e_0= initial void ratio
p_0= initial average stress
κ= the inclination of the e-log$p$ relation (as λ in Eqn 2:3)
J^{el}=the elastic volume ratio

The parameter κ, which is the essential parameter, is thus the logarithmic bulk modulus. Except for this parameter Poisson's ratio is also needed.

If the porous elasticity model is combined with the critical state plasticity model, the relation between e and p can be illustrated as in Fig 2-5.

Isotropic consolidation from the initial state e_0 and p_0 follows the plastic relation. Unloading at e_1 and p_1 means that the elastic relation is followed at unloading as well as reloading until e_1 and p_1 is reached again, after which the plastic relation is followed once again. Repeated unloading and reloading at e_2 and p_2 yields a similar result but another level of e-values.

Two things can be seen from Fig 2-5:

1) κ must be smaller than λ
2) The plastic e-p relation does not change while the elastic e-p relation is changed when the material is plasticized although the angle is the same.

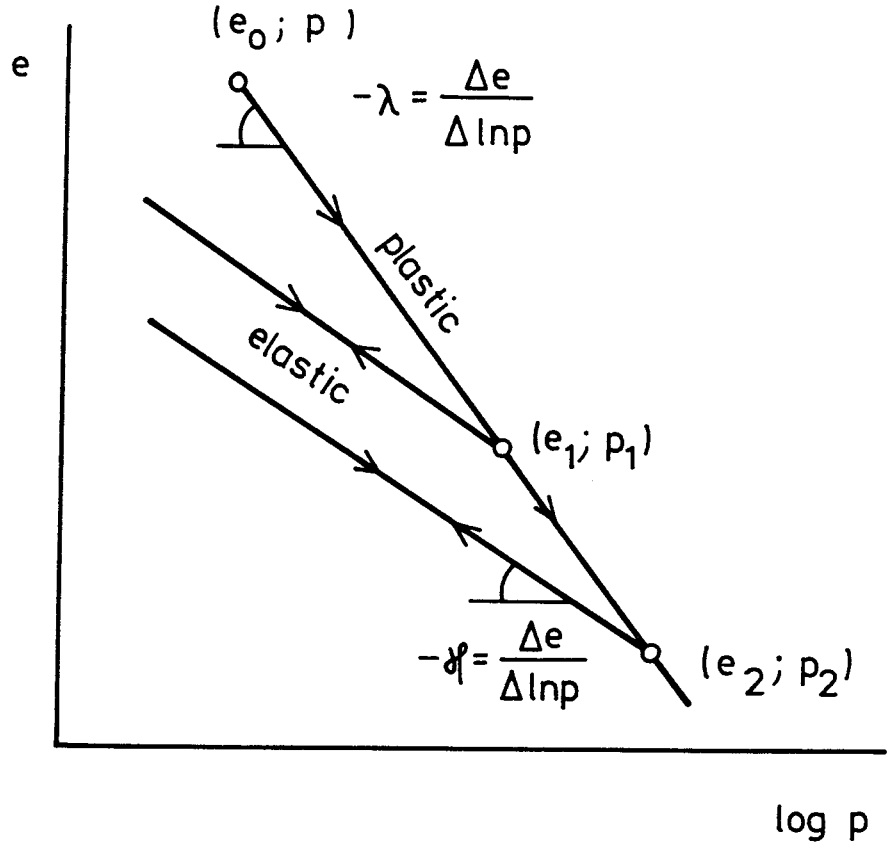

Figure 2-5: Illustration of the behavior of the Porous Elasticity model in combination with the CS model

The parameters necessary for the porous elastic model are thus:

κ and ν (plus e_0 and p_0)

2.6 PORE WATER MODELING

2.6.1 Effective stress

All the models presented require that the effective stress concept is valid. The effective stress concept says that all behavior of the water saturated soil

is controlled not by the total stress in the soil but by the effective stress σ':

$$\sigma'=\sigma-u \qquad (2:7)$$

where σ=the total stress
u=the pore water pressure in the soil

Even the combination of linear elasticity and metal plasticity requires that the effective stress concept is valid since the metal plasticity model is unaffected by a change in total stress. This is in agreement with the effective stress concept under certain conditions, e.g. when the stress change is quick and thus undrained. An undrained change in average stress will result in an almost equal change in pore pressure in a water saturated material and thus no change in effective stress.

However, if future investigations will show that the effective stress concept is not completely valid it is possible to change the rule according to Eqn 2:8:

$$\sigma'=\sigma-(1-b)u \qquad (2:8)$$

where b is a constant or a function of the void ratio e close to the value 0.

2.6.2 Water phase/solid phase

In a water saturated porous material there are two phases regulating the behavior (except for the structure stiffness that is described by the porous bulk modulus according to chapter 2.5):

* The water phase with the properties:
-density ρ_w

-bulk modulus B_w
-coefficient of thermal expansion α_w

* The solid phase (the grains) with the properties:
-density ρ_s
-bulk modulus B_s
-coefficient of thermal expansion α_s

The density values are dependant on the definition. If the solid is defined to be the remainder after 1 days exposure to 105°C, the following density values can be used for montmorillonite:

$\rho_w = 1.00$ t/m^3
$\rho_s = 2.79$ t/m^3

The other parameters can be achieved from standard tables:

$B_w = 2.1 \cdot 10^6$ kPa
$B_s = 2.1 \cdot 10^8$ kPa
$\alpha_w = 3.8 \cdot 10^{-4}$ 1/°K
$\alpha_s = 5.0 \cdot 10^{-6}$ 1/°K

Some of these values can be questioned. The state and form of the pore water in compacted bentonite is not fully known which means that the values can be somewhat erroneous. However, these possible errors do not affect the results of the calculation very much unless the sample is poorly water saturated.

2.6.3 Unsaturated material

Air bubbles in the pore water will strongly affect the compressibility. The average bulk modulus of an unsaturated pore water can be calculated according to Eqn 2:9

$$\frac{1}{B}=\frac{1}{B_a}(1-S_r)+\frac{1}{B_w}S_r \qquad (2:9)$$

where B is the resulting bulk modulus and B_a is the bulk modulus of air. B_a is very low or equal to the absolute pressure (e.g. at atmospheric pressure B_a=100 kPa).

If the degree of saturation is S_r=0.98 the resulting bulk modulus will be

$B=5.0\cdot10^3$ kPa

or a decrease by 240 times. If there is a back pressure
on the pore water the degree of saturation will increase according to Eqn 2.10:

$$S_r^p=1-(1-S_r)\frac{p}{p_a} \qquad (2:1)$$

where p = absolute pressure on the porewater
p_a = atmospheric pressure
S_r^p = degree of saturation at p

If the back pressure is 500 kPa and the absolute pressure on the pore water thus 600 kPa, S_r will increase from 0.98 to

S_r=0.996

and the corresponding bulk modulus will be

$B=1.4\cdot10^5$ kPa

which means that the decrease will be reduced to 15 times. These examples show that the degree of saturation is very important.

However, the solubility of gas in water is quite high. At atmospheric pressure and room temperature the solubility of air in water is about 1.5% meaning that theoretically a sample with an initial degree of saturation of S_r=98.5% will be completely saturated if all the water in the sample is deaired and can solve air. It is reasonable to believe that only one third to one half of the water can dissolve air, since only the deaired water added to the sample can dissolve air and probably only the part of the water that remains free water.

The conclusion is that about 0.5% air of the total water volume can be dissolved at atmospheric pressure. Since the the solubility is nearly a linear function of the absolute pressure, a back pressure of 500 kPa added to the atmospheric pressure means that 3% air can be dissolved (where 3% corresponds to the volume at atmospheric pressure).

2.6.4 Hydraulic conductivity

The rate of pore pressure dissipation is not only a function of the properties of the water, particles and structure but also of the hydraulic conductivity k of the material. Since k varies with the void ratio e a complete model must also include the relation between k and e:

$$k=f(e) \qquad (2:11)$$

In ABAQUS any possible function f might be given.

2.7 GENERAL COMMENTS

Since the Drucker-Prager model and especially the Critical state model are quite complicated models they are not easily handled in the calculations. The plastic flow has been especially difficult to handle and in numerous calculations it has not been possible to pursue the calculations until after several trials due to bad convergence or errors in the program.

The use of the material models and the finite element program has been stretched to its limits (or sometimes beyond that) when applied to the properties of smectitic clays or when simulating the extremely large strains involved in some of the tests. Since the program cannot handle too oddly deformed elements, such problems can only be solved by complete remeshing of the structure. Thus the computer work is not limited to putting parameters into a model but much effort has to be made on adapting the models and program to the special properties and behavior of the studied buffer materials.

3. EFFECTIVE STRESS CONCEPT

3.1 DEFINITION

The effective stress theory (Eqn 2:7) is the basis of all soil mechanics. It has been proven to be valid for a variety of different inorganic soils from sand to illitic clay as well as for organic soils ranging from peat to mud. In all calculations and analyses made so far Eqn 2:7 has been assumed valid. However, the complex micro structure of and unknown consistency of the interlamellar water in smectitic clays makes the validity of Eqn 2:7 somewhat uncertain.

The total stress is according to the classical view:

$$\sigma=\frac{N}{A}=p\frac{A_s}{A}+u\frac{A-A_s}{A} \qquad (3:1)$$

where N=the total force on one side of a cube of clay
A=the total area of one side of the cube
A_s=the horizontal area of the particle contacts in a cross section through only contacts
p=the contact pressure
u=the pore water pressure

Fig 3-1 shows the cross section through a cubical sample. The contact pressure p is very high due to the very small contact area A_s. pA_s is thus the total force over the area A that is transmitted through the cross section by the structure and that force divided to the total area $p\frac{A_s}{A}$ is the so called effective stress σ'_c in the sample (index c stands for contact). The rest of the horizontal area in the cross section

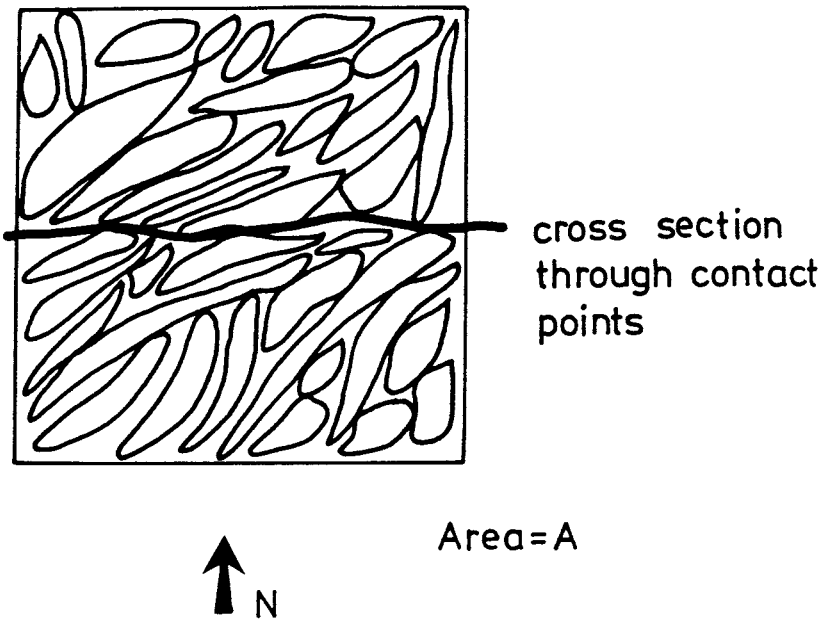

Figure 3-1: Detail of a soil structure illustrating Eqn 3:1

$A-A_s$ is thus the area of water. If $\frac{A_s}{A}=b$ the equation is written

$$\sigma=\sigma'_c+u(1-b) \qquad (3:2)$$

If A_s is very small compared to the total area and thus $b\approx 0$ the effective stress theory is valid.

3.2 RELEVANCE FOR SMECTITIC CLAYS

In smectitic clay the question is not whether the contact area A_s is small since it is generally considered that there is no direct particle to particle contact in such clay. The question is rather: in what

state is the water between the lamellar stacks and how are the stresses transferred between the stacks. The particles in Fig 3-1 may represent stacks of smectite clay flakes in stead of particles. If the water between the stacks have a viscosity that is Newtonian and distributes stresses in the same way as free water (ν=0.5) it is probable that the effective stress theory is valid and b=0 in Eqn 3:2. However, such a water can not distribute the stresses in the structure. These stresses must instead be balanced by electro-chemical forces of the electrical double-layers between the stacks and perhaps also between the flakes in a stack.

In such a system it is logic that Eqn 3:2 is substituted to Eqn 3:3.

$$\sigma=\frac{F_r-F_a}{A}+u(1-b) \qquad (3:3)$$

where F_r = the sum of the horizontal repulsive forces in a cross section according to Fig 3-1

F_a = the sum of the horizontal attractive forces in a cross section according to Fig 3-1

In such a model b=0 since A_s=0. $\frac{F_r-F_a}{A}$ is in this system regulating the behavior in the same way as the effective stress except for shear resistance which is not achieved from friction. Thus the stress in the structure over the cross section area A can be considered an effective stress σ'_e (where index e stands for electro) and Eqn 3:3 turns into Eqn 3:4

$$\sigma=\sigma'_e+u \qquad (3:4)$$

which means that the effective stress concept is valid. In a commercial bentonite the content of non-smectitic minerals is 20-50% depending on the quali-

ty. This "contamination" means that, especially at high densities, there is also a large amount of mineral contacts. The resulting effective stress is thus probably a combination of Eqns 3:1 and 3:3 as shown in Eqns 3:4 and 3:5

$$\sigma=\frac{N}{A}=p\frac{A_s}{A}+\frac{F_r-F_a}{A}+u\frac{A-A_s}{A} \qquad (3:4)$$

$$\sigma=\sigma'_c+\sigma'_e+u(1-b) \qquad (3:5)$$

A fictive effective stress is thus the sum of the "contact" and the repulsive electrical double-layer stresses:

$$\sigma'=\sigma'_c+\sigma'_e \qquad (3:6)$$

The parameter b is thus important for making the correct calculations or analyses of the buffer behavior. The question is if b is so close to zero that the classical effective stress theory is valid or if a correction factor must be taken into account. Water saturation is required since otherwise $b\neq0$ on that reason.

3.3 REQUIREMENTS FOR VALIDITY

There is a key question that must be answered when evaluating the effective stress theory:

* *Does a change in pore pressure change the effective stress if the void ratio is kept constant?*

This question is partly answered if a change in pore pressure in a sample with a constant volume results in an equal change in total stress or if a change in total stress in a confined volume results in an equal

change in pore pressure or if a parallel equal change in total stress and pore pressure does not change the void ratio. One can write:

$$\Delta\sigma=\Delta\sigma'+\Delta u(1-b) \qquad (3:7)$$

$$b=1-\frac{\Delta\sigma}{\Delta u}+\frac{\Delta\sigma'}{\Delta u} \qquad (3:8)$$

$\Delta\sigma=\Delta u$ means $b=\frac{\Delta\sigma'}{\Delta u}$.

$\Delta\sigma=\Delta u$ could mean that b and $\Delta\sigma'$ are zero and that the effective stress theory is valid but it could also mean that the effective stress has been changed by the amount $\Delta\sigma'=a\Delta u$.

Two types of tests are thus required. In the first (type A) the cell pressure is changed on an undrained sample and the pore pressure change is measured. In the second (type B) the stress-strain relation is measured in a triaxial test after an undrained change in cell pressure. If the change in pore pressure is equal to the change in cell pressure in the first test and the stress-strain relation is not changed in the second test, the effective stress theory should be valid. Such tests have been performed on samples with rather high density.

3.3.1 Test-type A

Two tests of this type were performed. In both tests a saturated sample of rather high density was mounted in a triaxial cell. After a period of 50 to 100 days a fairly good equilibrium was established. The pore pressure was measured in the top as well as in the bottom.

After mounting, a high cell pressure (about double the swelling pressure) was applied to the sample

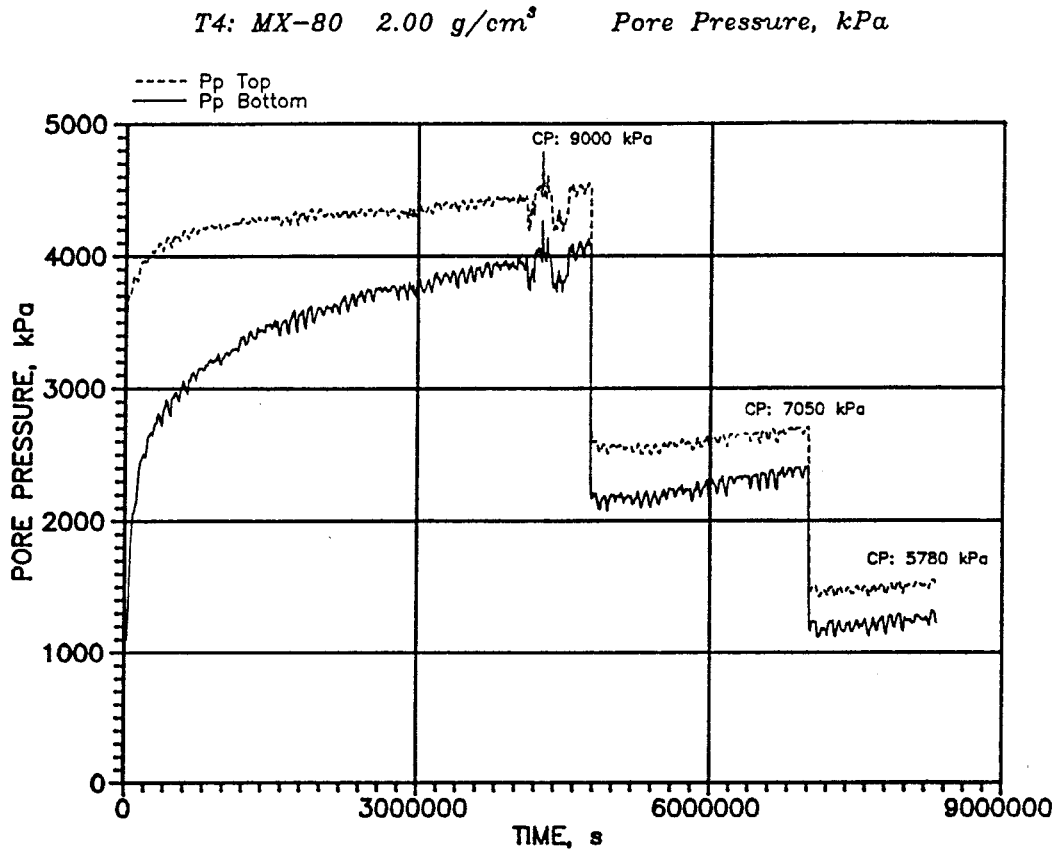

Figure 3-2: The pore pressure response on a change in cell pressure measured in the first test

Since no drainage was allowed the pore pressure matched the cell pressure and the resulting pressure $\sigma'=\sigma-u$ was assumed to be the swelling pressure.

After "equilibrium" the cell pressure was decreased in steps. The pore pressure response was measured in each step and each step was allowed to rest for 15 to 30 days.

Test 1

Fig 3-2 shows the result from the first test. The sample was Mx-80 Na-bentonite with the following data:

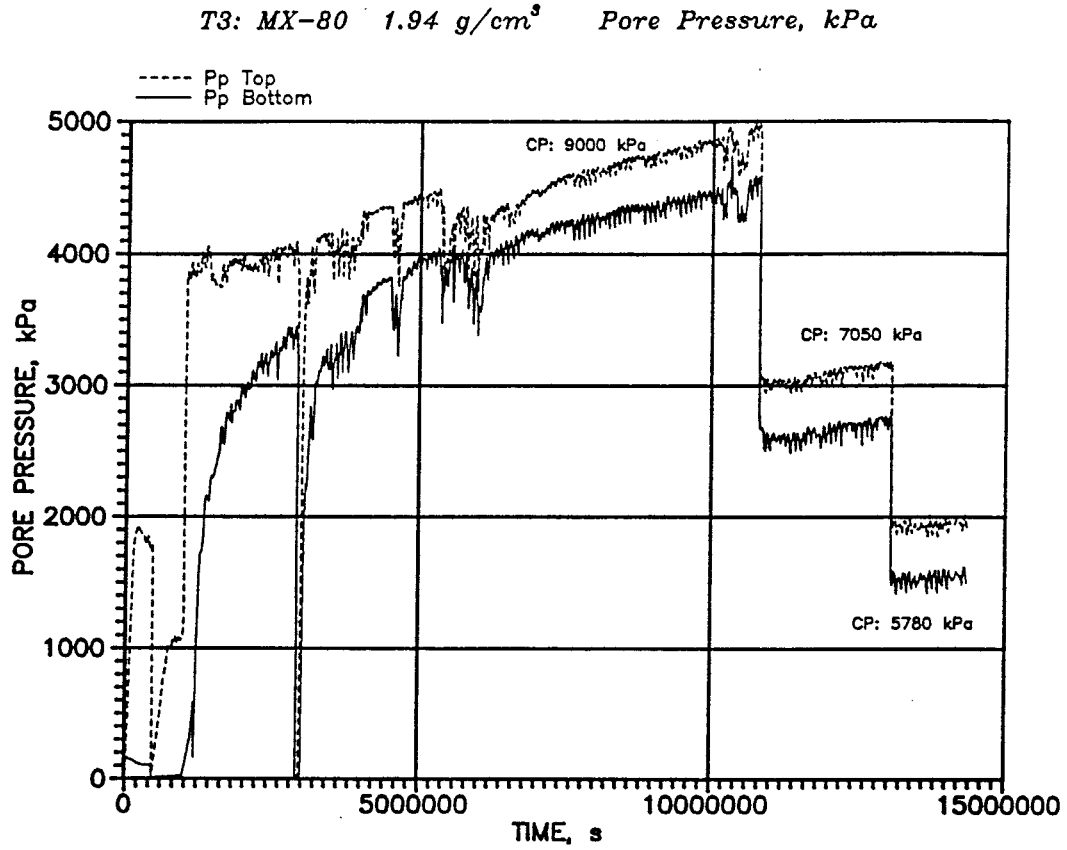

Figure 3-3: The pore pressure response on a change in cell pressure in test 2

Density at saturation ρ_m=2.00 t/m^3
Water ratio w=27.4%
Degree of saturation at atmospheric pressure S_r=98.8%

The degree of saturation was calculated using the densities accounted for in chapter 2.6.2.

Thus the degree of saturation should be high enough to assure complete saturation at the high pore pressure used in the tests.

Test 2

The results from the second test is shown in Fig 3-3. The data for this test was:

Mx-80 Na-bentonite with ρ_m=1.99 t/m^3
w=29.1%
S_r=99.6%

The figures show that the pore pressure is not equal in the top and the bottom in neither test. They also show that the pore pressure is increasing slowly even after a very long time. The difference in pore pressure can be explained by the difference in water ratio (and thus density and swelling pressure) between the lower 10% and the upper 10% of the sample. Table 3-1 shows the relations:

Table 3-1 Difference in pore pressure and water ratio between the top and bottom of the samples

Test	$w_{top}-w_{bot}$	$u_{top}-u_{bot}$
Test 1	0.7%	230 kPa
Test 2	1.6%	400 kPa

A higher density at the bottom of the samples gives a higher effective stress and thus a lower pore pressure. The increase in pore pressure with time is probably either some leakage phenomenon or a creep effect.

Figs 3-2 and 3-3 show that the change in pore pressure is very close to the change in cell pressure. A closer evaluation of the effect of a pressure change is shown in Table 3-2.

Table 3-2 The relation $\frac{\Delta u}{\Delta \sigma}$ measured at the two tests

Test	$u_{average}$	$\frac{\Delta u}{\Delta \sigma}$
Test 1	1.93 MPa	0.96
	3.32 MPa	0.99
Test 2	2.33 MPa	0.97
	3.79 MPa	0.98

The relation between the increase in pore pressure and total pressure is only a few per cent from 1.00.

3.3.2 Test type B

After having observed that the changes in total stress and pore pressure are almost equal at constant void ratio, the question is whether the mechanical properties are equal as well. This can be tested if samples are sheared to failure under different total stress but equal void ratio.

An example of a test in which the total stress has been changed during a triaxial test is shown in Fig 3-4. The density of the sample is ρ_m=1.98 t/m^3. Originally the total stress is σ=4.5 MPa and the pore pressure u=0.16 MPa. After about 2.5% strain the total stress was increased to σ=9.0 MPa. This resulted in a pore pressure increase of Δu=4.5 MPa and a stress-strain curve in which no effect of the total stress change could be observed. Other tests of a similar type yielded corresponding results [4].

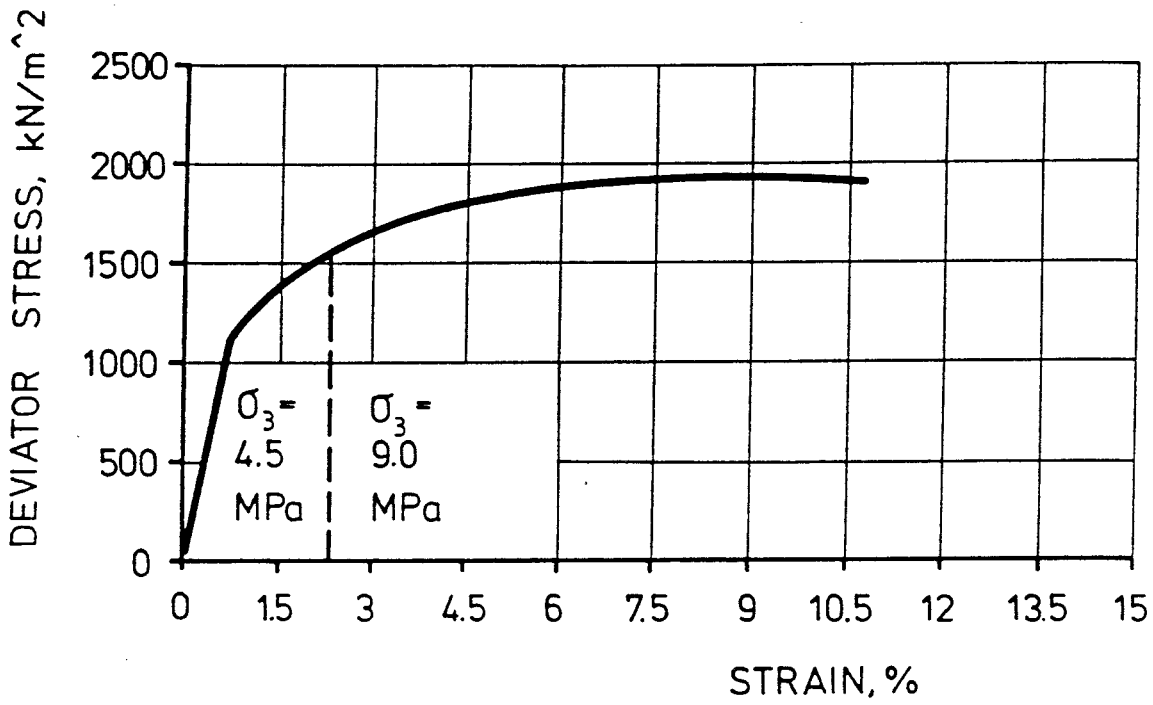

Figure 3-4: Stress strain relation in an undrained triaxial test with a change in cell pressure during the test

3.4 CONCLUSIONS

Thus, the mechanical properties seem to be unchanged if the total stress is changed without changing the void ratio. Since it seems as $\Delta\sigma' \approx 0$ and $\Delta\sigma \approx \Delta u$ in Eqn 3:7, the conclusion must be that $a \approx 0$, which indicates that the effective stress theory is applicable.

Although additional tests, including drained ones, must be performed at different densities in order to fully prove the validity of the effective stress concept for dense smectite clays, no results obtained so far contradict this basic concept. It will therefore be applied in the subsequent calculations.

4. DERIVED MODELS

The material models shown in chapter 2 and a lot of laboratory tests have yielded some real buffer material models. Some of the tests and some of the the derived models will be presented in this chapter.

4.1 TOTAL STRESS MODELS

Short time scenarios can be modeled without considering pore pressure changes. The requirements are that the event takes such a short time that no pore water movements will take place in the material, and that the undrained behavior is independent of the stress path. The smectite-rich buffer materials actually seem to be independent of the stress path under completely undrained conditions due to the validity of the effective stress theory. Since a change in average stress results in an almost equal change in pore pressure, the stress-strain behavior is only a function of the Mises' stresses.

4.1.1 Laboratory tests

Numerous triaxial tests and shear tests have been performed and are presented in earlier reports [2], [4]. These results can be summarized as follows:

- The deviatoric stress at failure q_f is a function of the average stress p according to Fig 4-1.

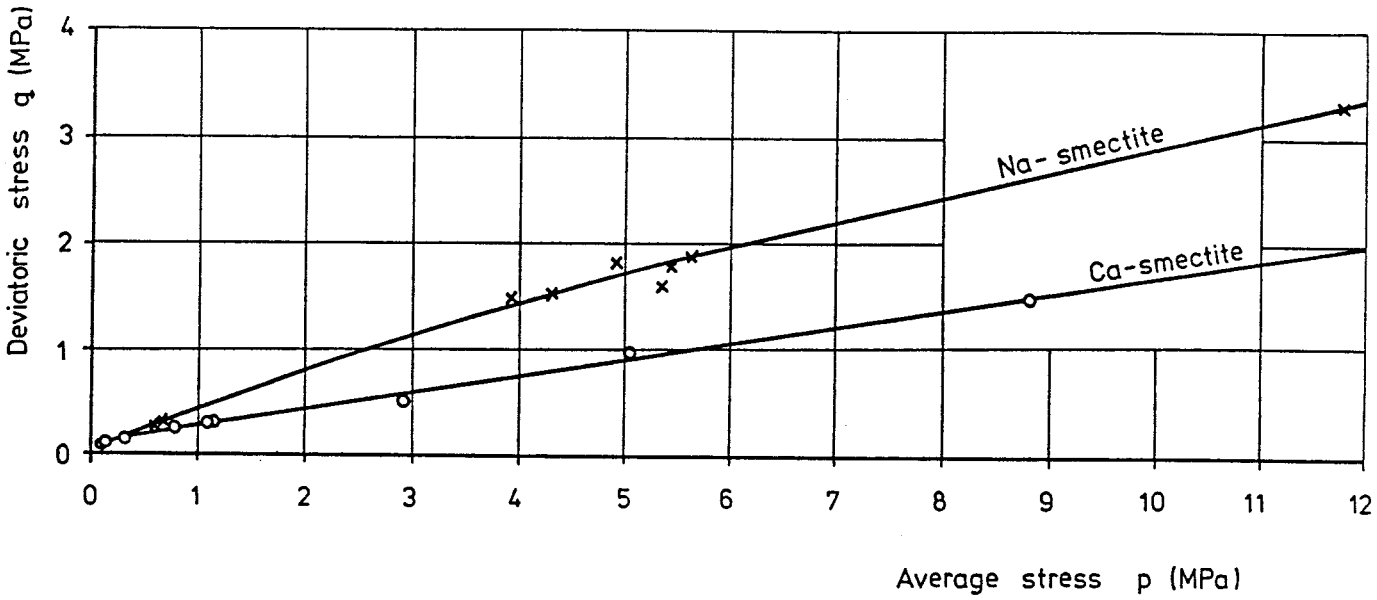

Figure 4-1: Measured deviatoric stresses at failure as a function of the total average stress for two different smectite-rich clays

- The stress-strain relation (q-ε) can be normalized with respect to the deviatoric stress at failure q_f. Fig 4-2 shows the normalized stress-strain relation ($\frac{q}{q_f}$-ε).

- A small strain rate dependence of the failure stresses seems to exist. It can be described according to Eqn 4:1.

$$q_f(\dot{\varepsilon}) = q_f(\dot{\varepsilon}_0)\left(\frac{\dot{\varepsilon}}{\dot{\varepsilon}_0}\right)^n \qquad (4:1)$$

where n=0.065

- The influence of temperature up to ≈90°C is small

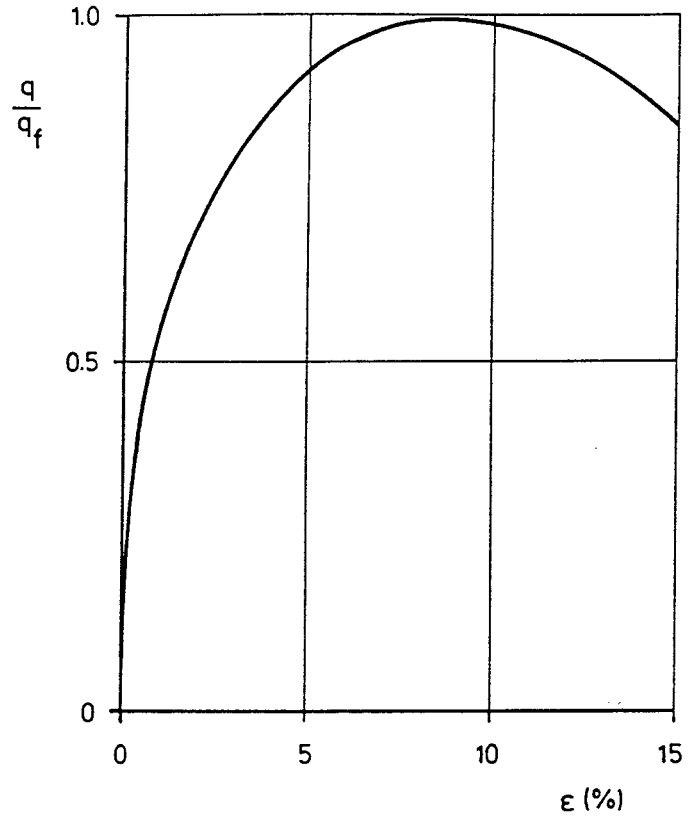

Figure 4-2: Normalized deviatoric stress-strain relation at undrained triaxial tests

- The behavior of Ca-bentonite is similar to the behavior of Na-bentonite except for the shear strength which is 50-60% lower. (The behavior of Ca-bentonite refers to the French reference clay).

4.1.2 "Metal" elasticity-plasticity model

The undrained behavior can be modeled, without considering the pore pressure, with the metal plasticity model in the plastic region (as described in chapter 2.1) and with the linear elasticity model in the elastic region (as described in chapter 2.4).

The model is a function of the void ratio and it is

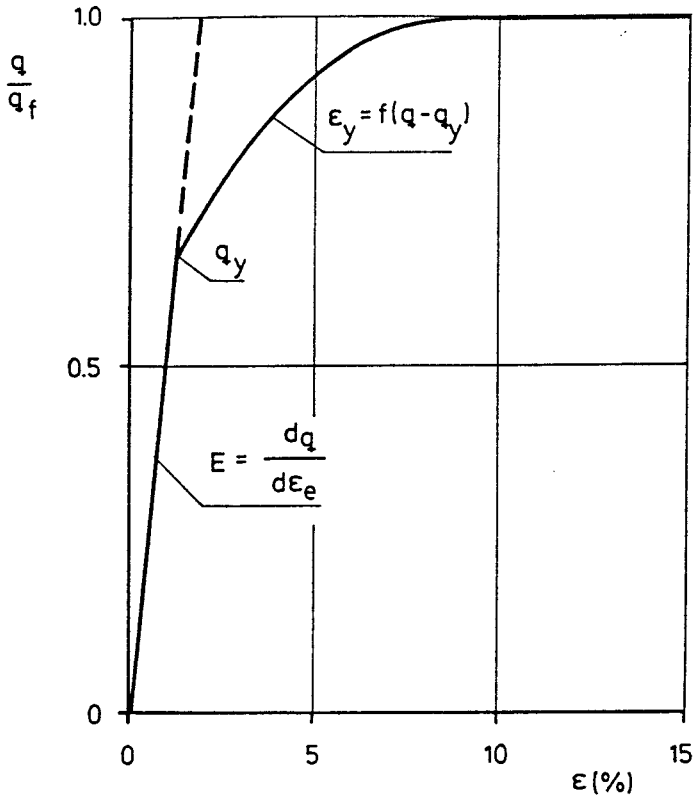

Figure 4-3: Elastic-Plastic material model at the total stress analyses

only valid at one void ratio. If the void ratio is changed during some process studied, the model is no more valid but must be changed. Input data are:

E, ν and $\varepsilon_y = f(\sigma_j)$

These data can be taken from Fig 4-1 and Fig 4-3. The swelling pressure at the actual density or void ratio determines q_f according to Fig 4-1. The module of elasticity E and the plastic stress strain relation can then be determined from Fig 4-3. $\sigma_2 = \sigma_3$ means that $q = (\sigma_1 - \sigma_3) = \sigma_j$. The total strain ε_t at a change in q from q_1 to q_2 is calculated as the sum of the elastic and plastic strains:

$$\varepsilon_t = \varepsilon_e + \varepsilon_y = \frac{q_1 - q_2}{E} + f(q_2 - q_y) \qquad (4:2)$$

Fig 4-3 differs somewhat from Fig 4-2 in 2 ways. Firstly, the "elastic" part is made linear and assumed to reach 70% of the failure stress in order to simplify the modeling. Secondly, no strain softening is assumed after failure, because the post failure behavior is not perfectly clear.

4.2 EFFECTIVE STRESS MODELS

As soon as there is pore water transport or a change in void ratio involved in the process, an effective stress model must be used. These models can also be a combination of one elastic model and one plastic model. The elastic and plastic behaviors can only be investigated by laboratory tests in which the void ratio and the pore pressure are known.

4.2.1 Laboratory tests

The required laboratory tests, to make an effective stress model, are much more complicated than the tests needed for making a total stress model:

- The correct measurements of the pore pressure requires a high back pressure on the pore water.

- The time for equilibrium, before the test can start, is very long.

- The test must be very slow, especially if it is drained.

The difficulties are primarily caused by the very low hydraulic conductivity of the clays. A very slow test

is a problem, not only by taking a long time and thus occupying the equipment, but also by secondary effects taking place. Such secondary effects can be: temperature variations, transducer drifting, evaporation, membrane leakage and creep phenomena.

The following tests have primarily been done in order to determine the effective stress behavior of the smectite rich clays:

- Undrained triaxial tests
- Drained triaxial tests
- Isotropic consolidation tests
- Oedometer tests with stepwise consolidation and swelling
- Hydraulic conductivity tests
- Thermomechanical tests
- Friction tests

Some of these tests especially the isotropic consolidation tests and the drained triaxial tests caused tremendous problems. The results of these tests are uncertain.

Many of the tests are used as verification tests as well, since none of them were conducted on samples with homogeneous stresses and strains.

Other tests which will not be accounted for in this report have been performed as well e.g. creep tests.

4.2.1.1 Triaxial tests

Undrained triaxial tests were performed on samples with the diameter 5 cm and the height 10 cm. In these tests pore pressure were measured at the top as well as at the bottom of the samples. The strain rate for most of these tests was 0.06% per hour which means

that each test took about 2 weeks. Some tests have been run with the strain rate 0.6% per hour. Between mounting the samples and the start of the tests the samples were allowed to rest 1-3 months to assure equilibrium.

Most samples were compacted directly in a saturation device at the natural water ratio $w \approx 10\%$. In that device the sample is surrounded by filter stones to minimize the required time to saturation. Before filling up the filters with water the whole device is deaired by a vacuum pump. By this procedure no air is trapped in the sample. After saturation the sample is taken out, trimmed and mounted in the triaxial cell.

In the drained tests the samples were 5 cm high and 3.5 cm in diameter. A system for radial drainage was mounted on the samples as well. The strain rate of the three tests accounted for was 0.012% per hour, meaning that a complete test took 5-10 weeks.

In Fig 4-4 the results from 10 different triaxial tests are summarized in a q-p diagram. Tests 7, 9 and 10 were drained tests and the other tests were undrained. Test 3 was step wise loaded and each step (marked with a dot in the figure) was allowed to rest for 10 days. 10 days was long enough as indicated by the pore pressure measurements.

All drained tests were preceded by isotropic consolidation. All undrained tests, except test 6, were tested at the same void ratio as they were compacted to. Test 6 was allowed to swell uniaxially from $\rho_m = 2.10$ t/m^3 to $\rho_m = 1.85$ t/m^3. Tests 5, 8 and 11 were preceded by undrained creep test under constant q corresponding to 30-60% of q_f for 10 days.

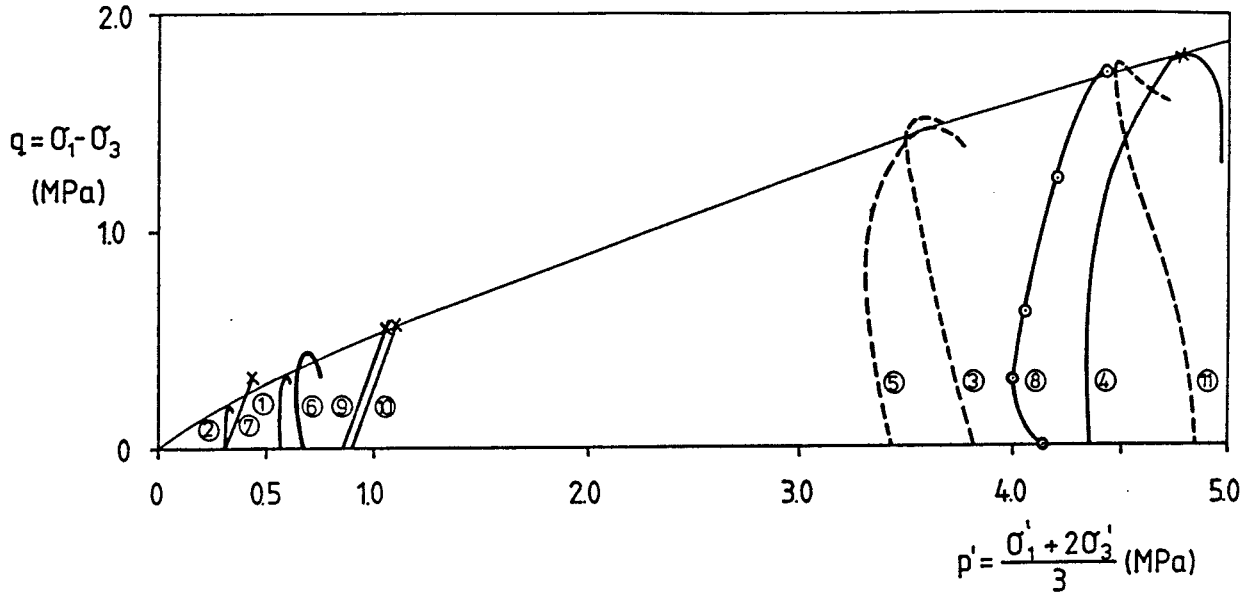

Figure 4-4: Stress path diagram for 8 undrained and 3 drained triaxial tests

All tests were conducted at room temperature except for test 5 which was done at the temperature 60°C.

The figure shows the following:

- All undrained specimens dilate at failure meaning that the average stress increases at and after failure.

- The failure envelope from the undrained normally consolidated tests is very well defined with surprisingly little scatter.

- The specimens in the drained tests and the undrained test 6 failed at stresses slightly above the failure envelope that was derived from the other tests.

- q was in average kept fairly constant during the tests until failure, meaning that the pore pressure increase balanced the increase in average stress. The maximum deviation for single tests was $\mp$ 8%.

4.2.1.2 Consolidation and swelling tests

3-dimensional isotropic consolidation tests and 1-dimensional oedometric consolidation and swelling tests have been performed. Since the results from the isotropic consolidation tests are somewhat unclear, probably due to drainage problems, only the oedometer tests will be reported here.

Earlier tests [4] have shown that the swelling pressure measured in an oedometer after swelling and compression are different and deviates from the swelling pressure measured at constant volume. Since the radial stresses inside an oedometer are unknown in ordinary tests, an oedometer was built in which these stresses could be measured. The equipment is shown in Fig 4-5. The radial stress is measured by a small piston that passes through the oedometer ring. The force on the piston is measured by a very stiff transducer outside the wall. The radial piston is kept in the center of the sample by having a balanced movable axial piston in the bottom of the sample as well as in the top. The measured radial force is transformed to stress by dividing it by the area of the radial piston.

The results of stepwise unloading and reloading are shown in Fig 4-6 (Mx-80 sodium bentonite) and Fig 4-7 (Moosburg calcium bentonite). The axial and radial pressures are plotted as a function of the void ratio. Both tests were made on samples with an initial void ratio of $e \approx 0.65$. They were unloaded in steps to an axial pressure of 100 kPa and then re-

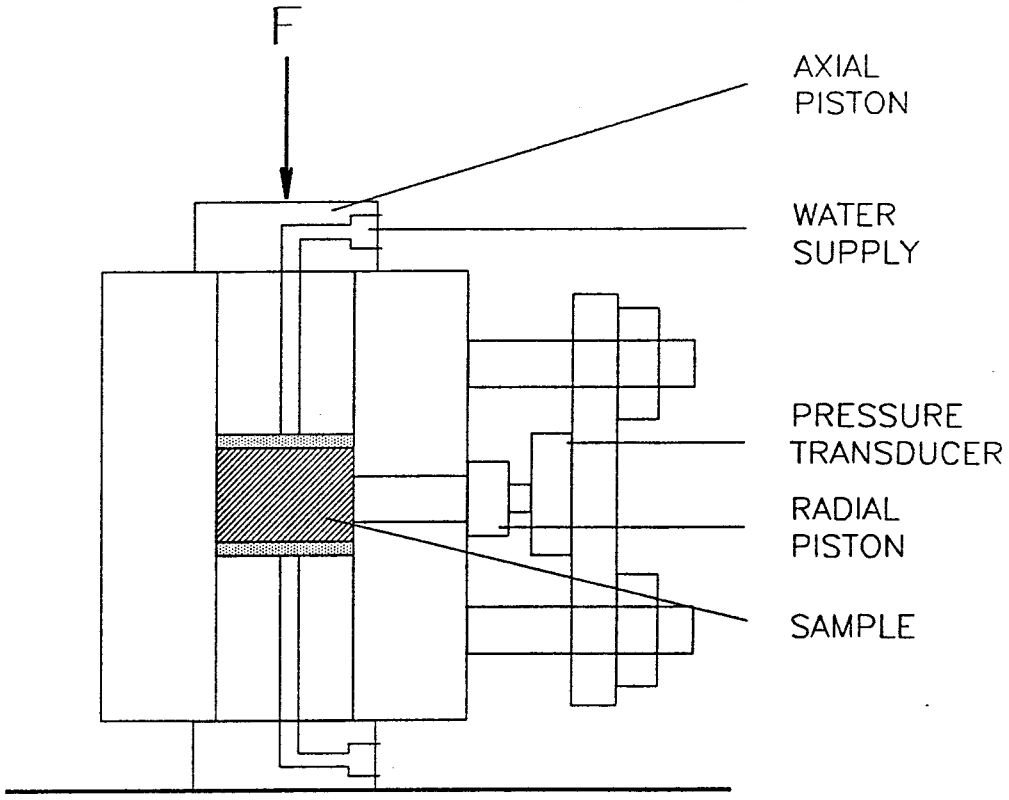

Figure 4-5: Schematic drawing of the oedometer with measurement of radial stress. The figure shows a situation in which only swelling can take place

loaded to 10 000 kPa. The following observations were made:

- The hysteresis effect of the axial stress is very high for both materials. At high void ratio the stress is strongly decreasing with increased void ratio and the ability to expand seems to be small even for the sodium bentonite.

- The hysteresis effect of the radial stresses is small.

- The radial pressure plotted versus the void ratio is a straight line in a semi-logarithmic diagram.

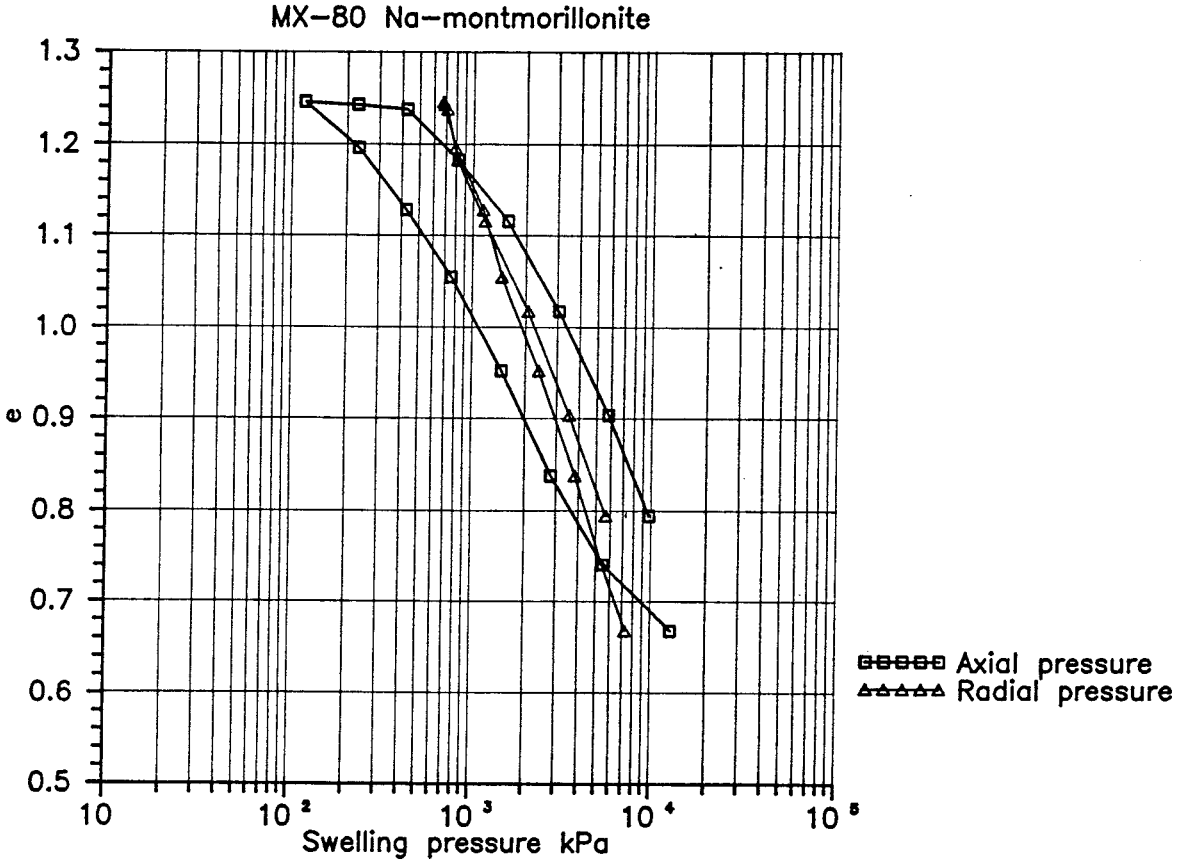

Figure 4-6: The void ratio as a function of the measured axial and radial pressure at stepwise unloading and reloading (Na-bentonite)

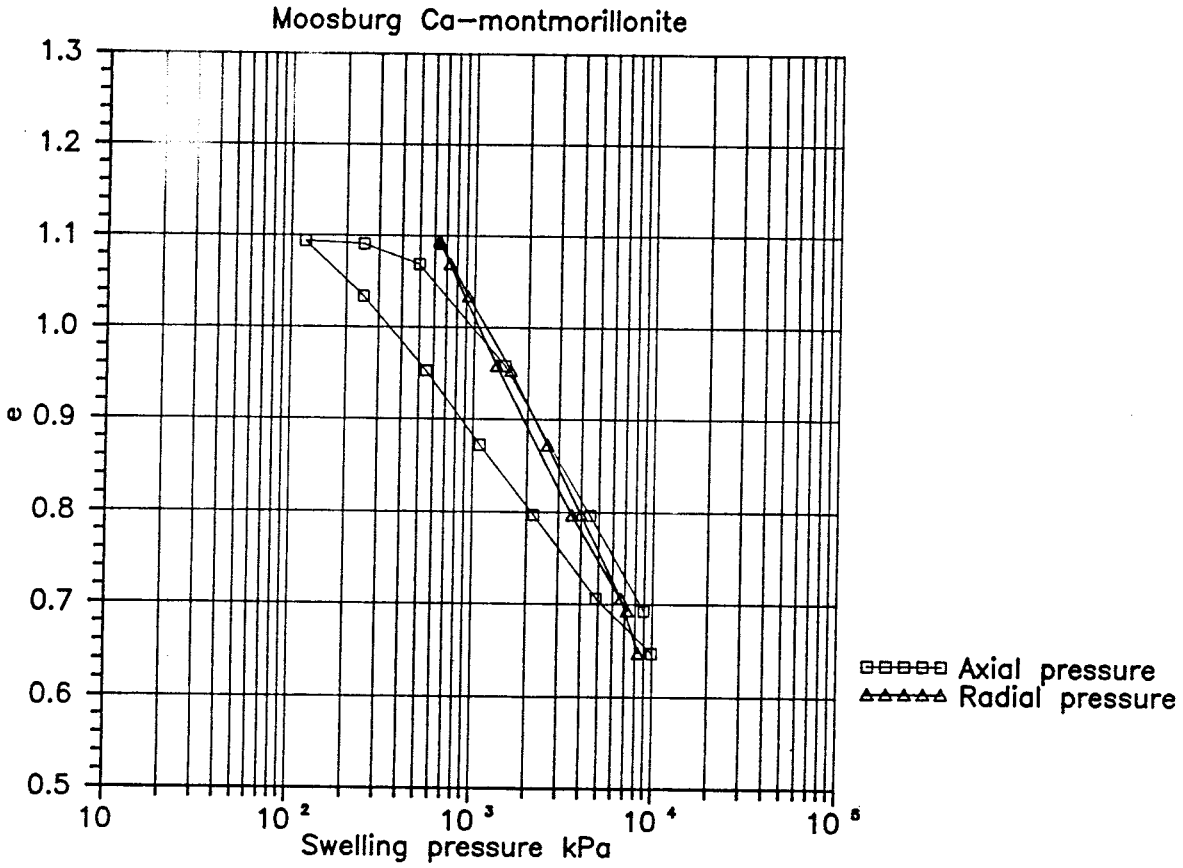

Figure 4-7: The void ratio as a function of the measured axial and radial pressure at stepwise unloading and reloading (Ca-bentonite)

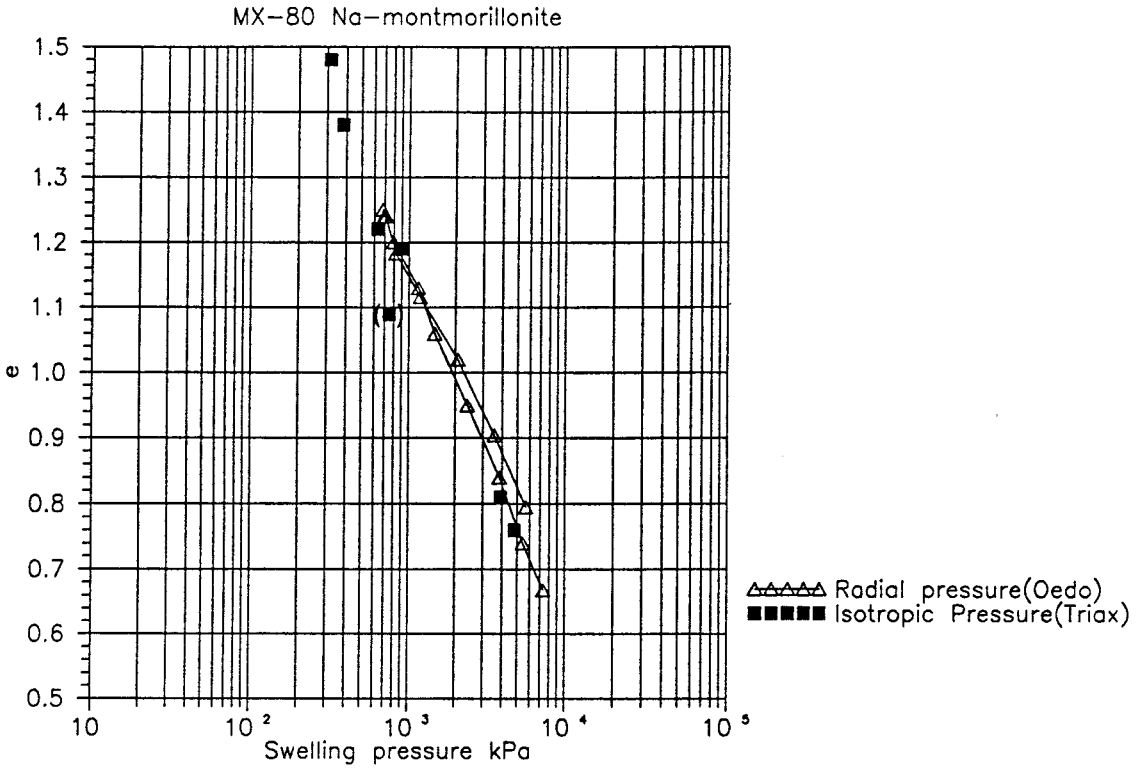

Figure 4-8: The void ratio as a function of the measured radial pressure at stepwise unloading and reloading compared to the isotropic swelling pressure measured in the triaxial cell

- A comparison shows that the radial pressure is almost exactly the same as the swelling pressure measured from constant volume tests.

The last conclusion is confirmed in Fig 4-8 which shows the swelling pressure evolved under undrained conditions in some of the triaxial tests. Only those tests in which the void ratio and the pore pressure could be controlled (long time equilibrium) are shown. The figure shows a very good concordance between the swelling pressure measured in the triaxial cell and the radial pressure measured in the oedometer. The only exception is test 6 which gave too

low swelling pressure. The reason could be that the sample in test 6 has been allowed to swell from $e \approx 0.65$ to $e=1.09$.

Each load step was maintained for about 10 days. The deformation and the radial pressure were recorded as a function of time. These results are shown in Figs. 4-9 to 4-12.

Fig 4-9 shows the height of the sample as a function of the time elapsed after the load decrease or load increase for each step in the tests on sodium bentonite. The shape of the curves is typical for consolidation tests, showing that 10^6 seconds are enough to ensure completed consolidation but just about enough to ensure complete swelling.

Fig 4-10 shows the recorded radial stresses during the same process. The figure shows that the entire radial stress at consolidation is achieved almost immediately, while, at expansion, half the radial stress was reached after a long time. The first 100 seconds were used for adjusting the weight.

Figs 4-11 and 4-12 show the same recordings for the calcium bentonite. As can be seen the rate of consolidation is higher for the calcium bentonite due to the higher permeability and smaller expandability.

4.2.1.3 Measurements of hydraulic conductivity

The hydraulic conductivity k is a function of the void ratio and temperature. k has been measured in several test series by one-dimensional flow in a swelling pressure oedometer [2],[4]. Fig 4-13 shows a summary of recent results for Mx-80 Na-bentonite.

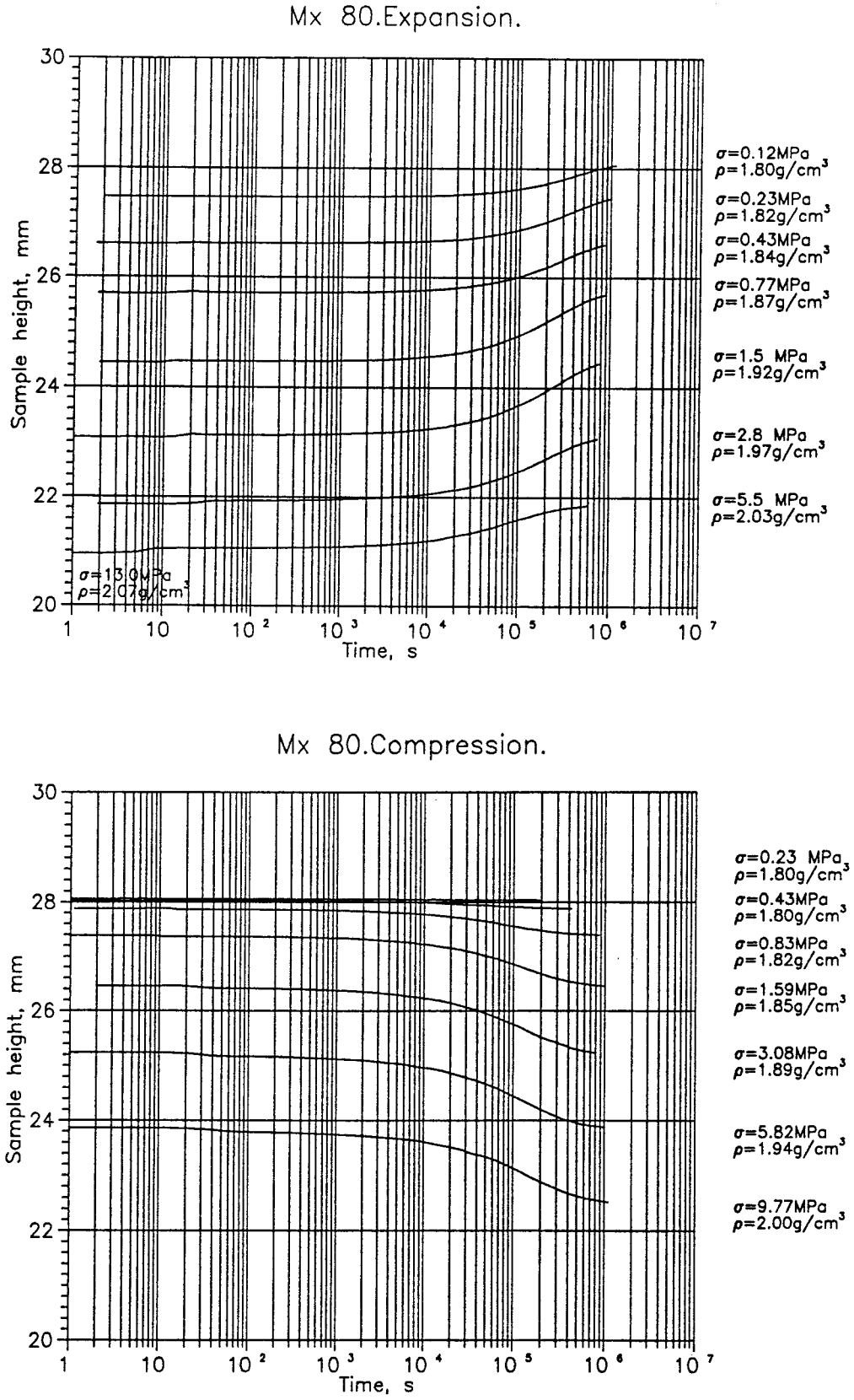

Figure 4-9: Swelling and consolidation curves from the test in Fig 4-6. The stresses at each load step refer to the axial load

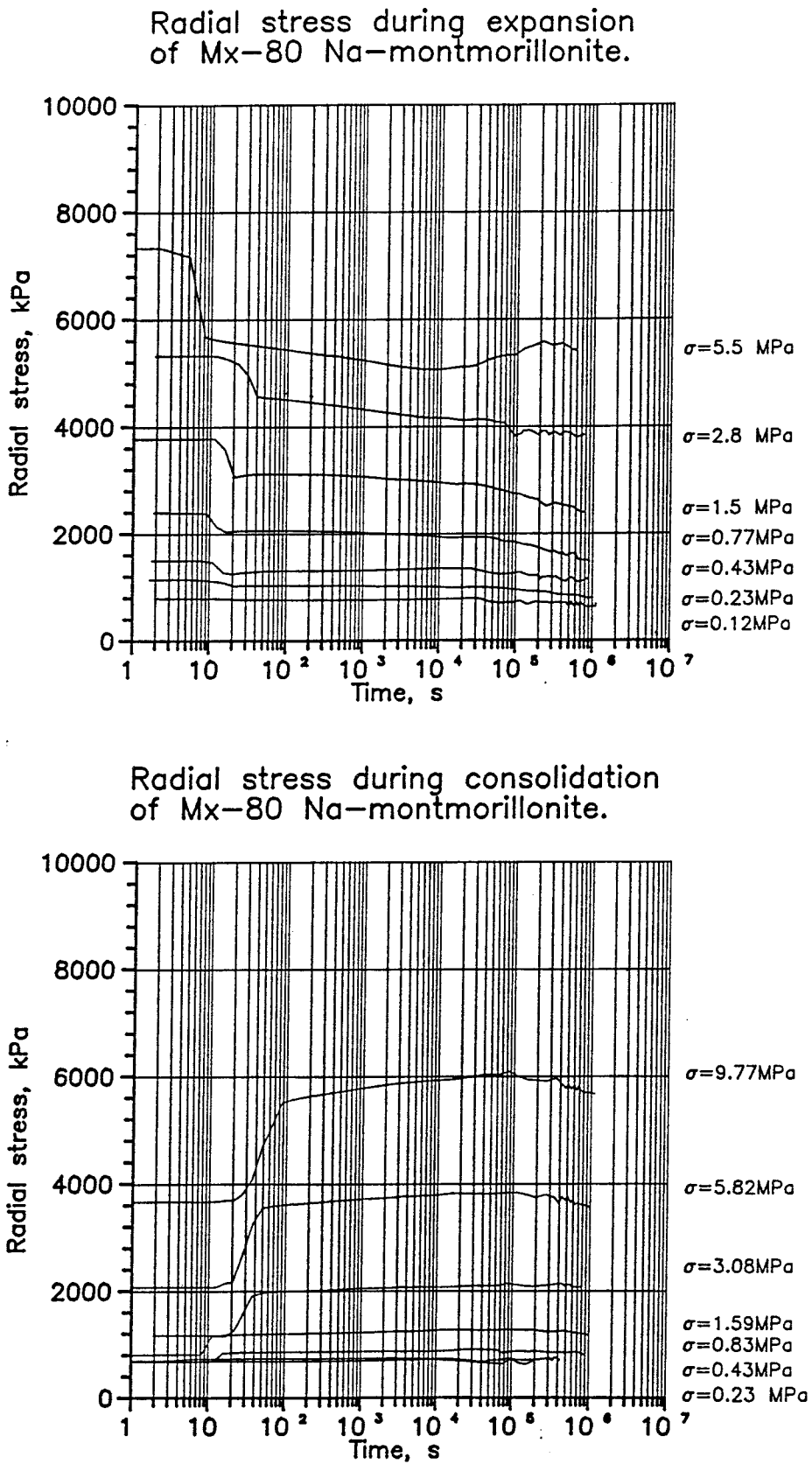

Figure 4-10: The radial stresses measured at each load step

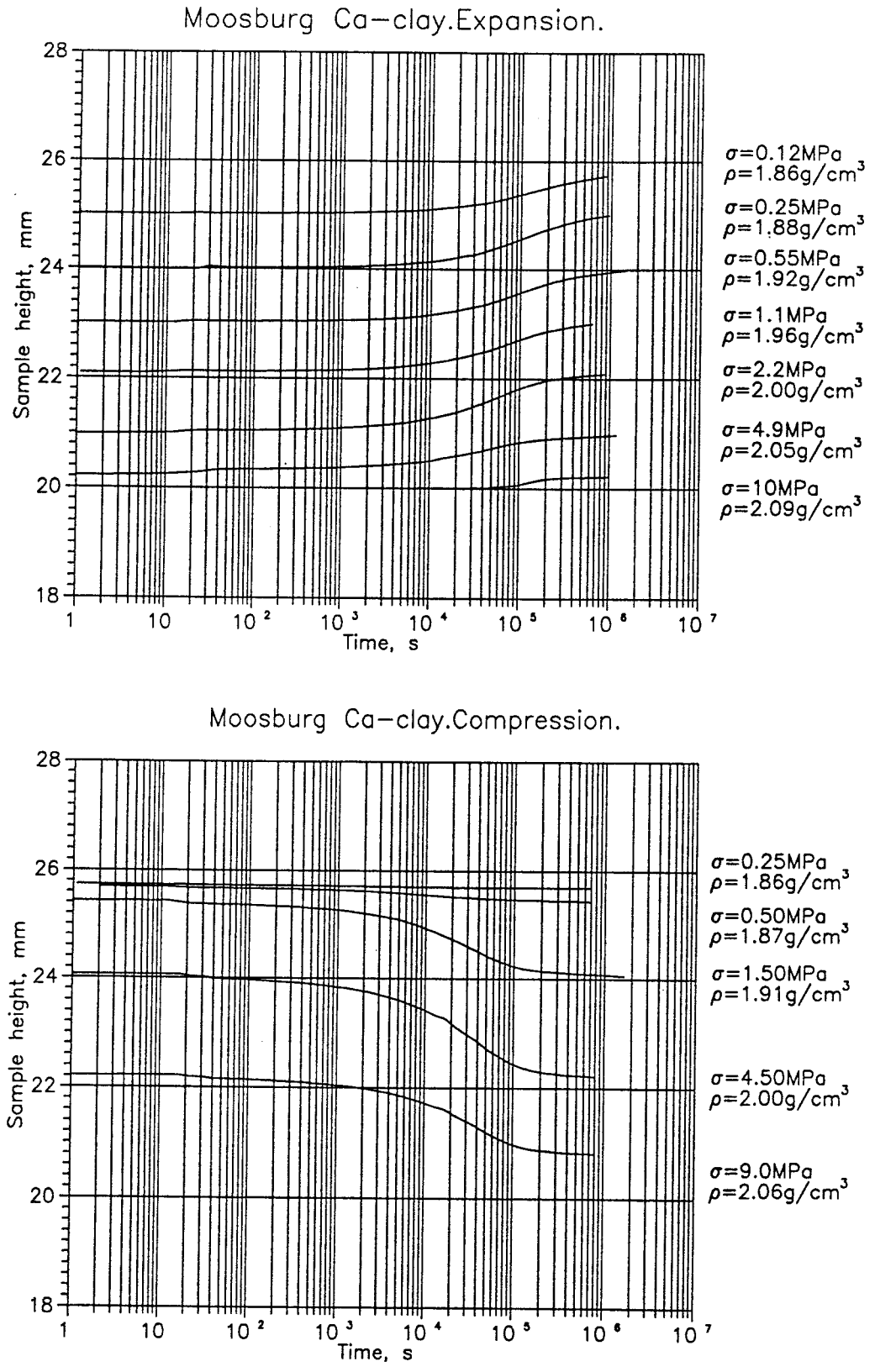

Figure 4-11: Swelling and consolidation curves from the test in Fig 4-7. The stresses at each load step refer to the axial load

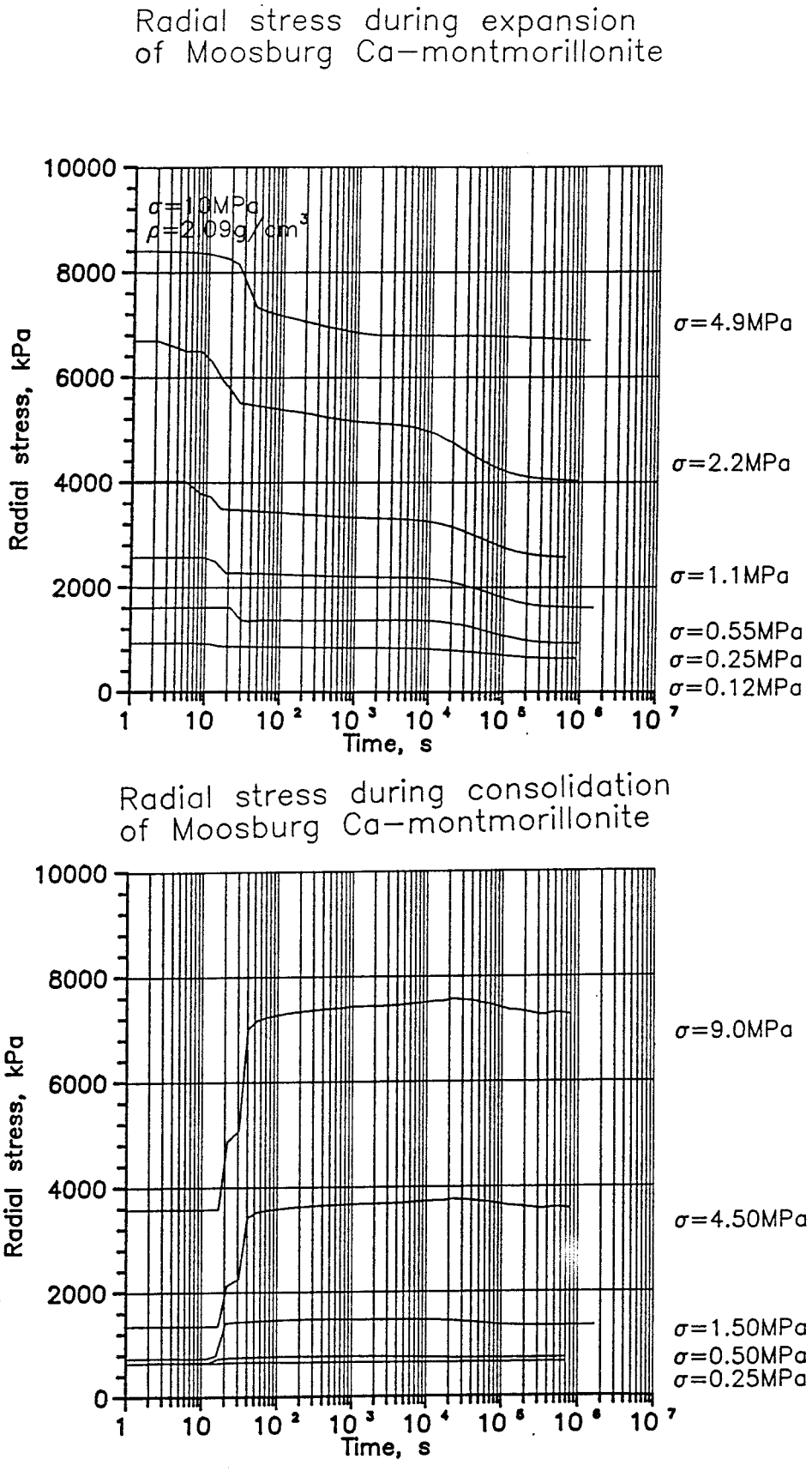

Figure 4-12: The radial stresses measured at each load step

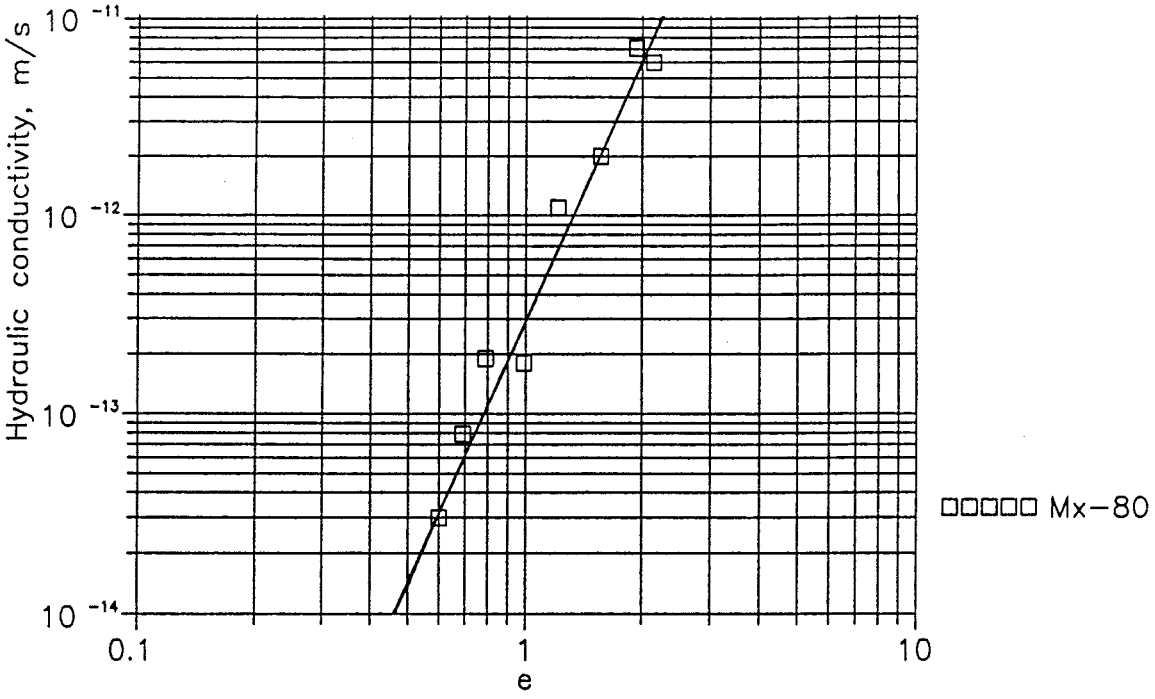

Figure 4-13: Hydraulic conductivity of Na-bentonite Mx-80 as a function of the void ratio

An increased temperature means that the permeability is increased, the temperature dependence being explained by the heat-affected viscosity of water. The permeability-void ratio relation at three temperatures is shown in Fig 4-14. The measured influence of the temperature is actually smaller than what could be expected by the decrease in viscosity, which may be explained by a heat-induced improvement of the microstructural homogeneity.

4.2.1.4 Thermomechanical tests

The thermomechanical response can be divided into three mechanisms:

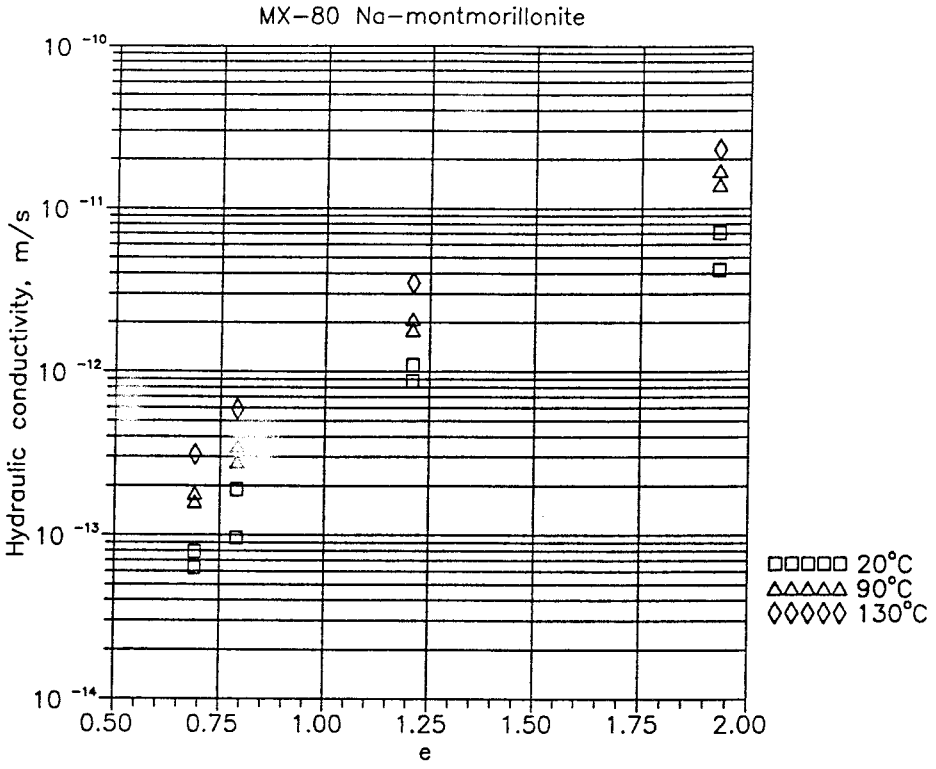

Figure 4-14: The hydraulic conductivity as a function of the void ratio measured at three temperatures

1) Thermal expansion of the pore water
2) Thermal expansion of solids
3) Change in structure (temperature-induced swelling pressure)

The high thermal expansion of the pore water will result in an immediate increase in swelling pressure due to an increase in pore pressure, if the sample is confined. With time the pore pressure will dissipate if drainage is allowed for and after equilibrium the swelling pressure will return to either the original or some new value (caused by mechanism 3). If the sample is exposed to a constant outer pressure it will instead undergo an increase in void ratio and the new swelling pressure will be controlled by the new void ratio and the temperature induced swelling pressure (mechanism 3).

Mechanism 3 is the only mechanism that needs to be considered since the expansion of the pore water and the grains are controlled by the coefficients of thermal expansion.

Preliminary measurements have shown that there is no evident influence of temperature on the swelling pressure at void ratios lower than 1.0 (ρ_m>1.8 t/m^3). At higher void ratios there seems to be a small increase in swelling pressure at increased temperatures for sodium bentonite (0.5-1.0% per °C) while the swelling pressure for calcium bentonite seems to decrease a little with increasing temperatures.

A series of thermomechanical tests have been performed to study the behavior. These tests are not primarily needed for developing the thermomechanical model and could be considered as verification tests.

Three samples with different densities were investigated with the following technique: The samples, having a height of 50 mm and a diameter of 50 mm, were compacted and saturated in a swelling pressure oedometer. A back pressure of 100 kPa was applied and the samples heated to 90°C. Drainage was allowed at both ends of the samples and the resulting "swelling pressure" was measured as a function of time until equilibrium was reached.

After equilibrium, the heat was turned off and the subsequent change in swelling pressure recorded.

The results of these tests are shown in Figs 4-15 to 4-17. The axial swelling pressure recorded by the transducer is plotted as a function of time after the heat was switched on or switched off.

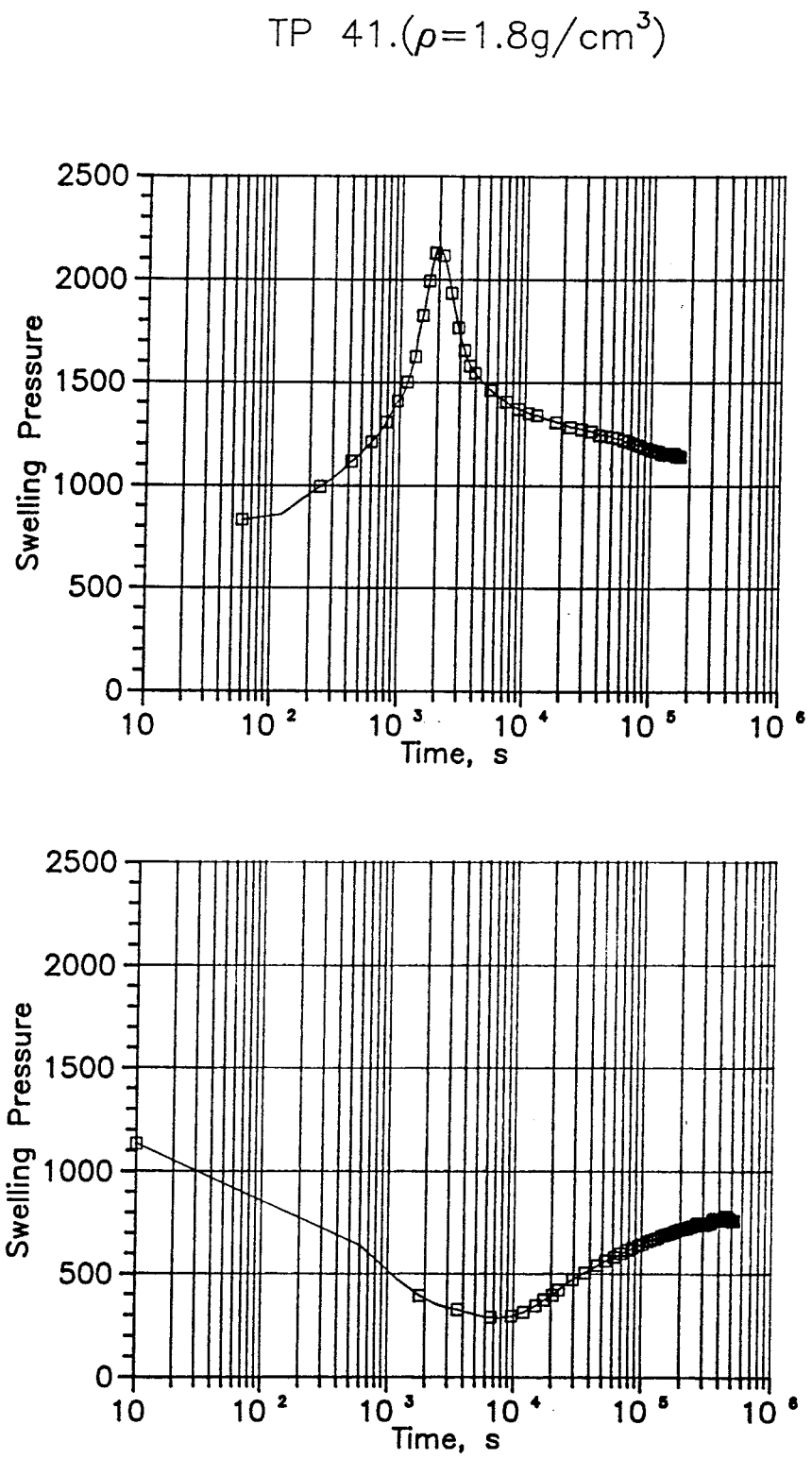

Figure 4-15: The measured axial pressure as a function of time after the start of the temperature increase (above) and after the start of the temperature decrease (below)

TP 21.(ρ=2.0g/cm^3)

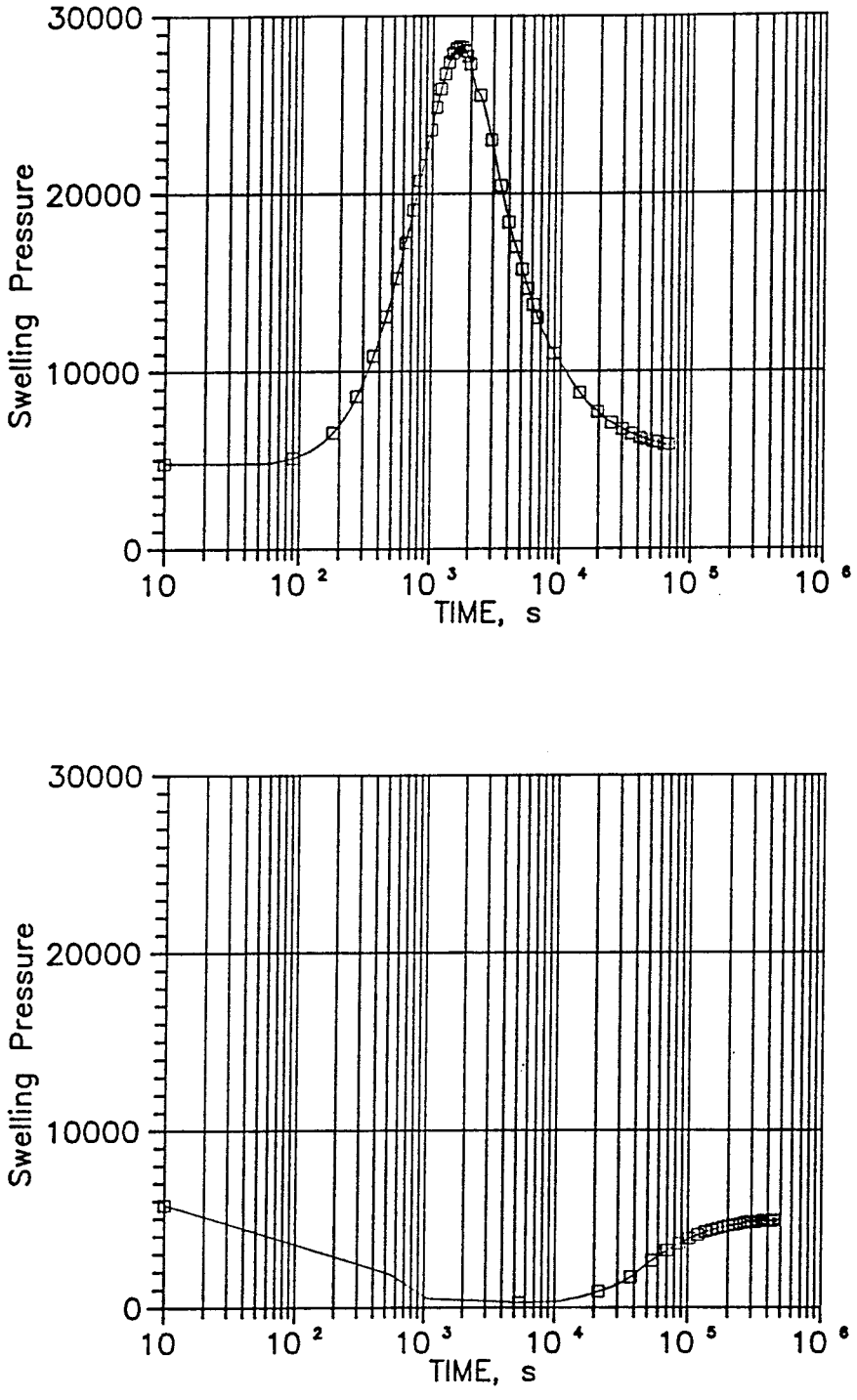

Figure 4-16: The measured axial pressure as a function of time after the start of the temperature increase (above) and after the start of the temperature decrease (below)

TP 31.(ρ=2.1g/cm^3)

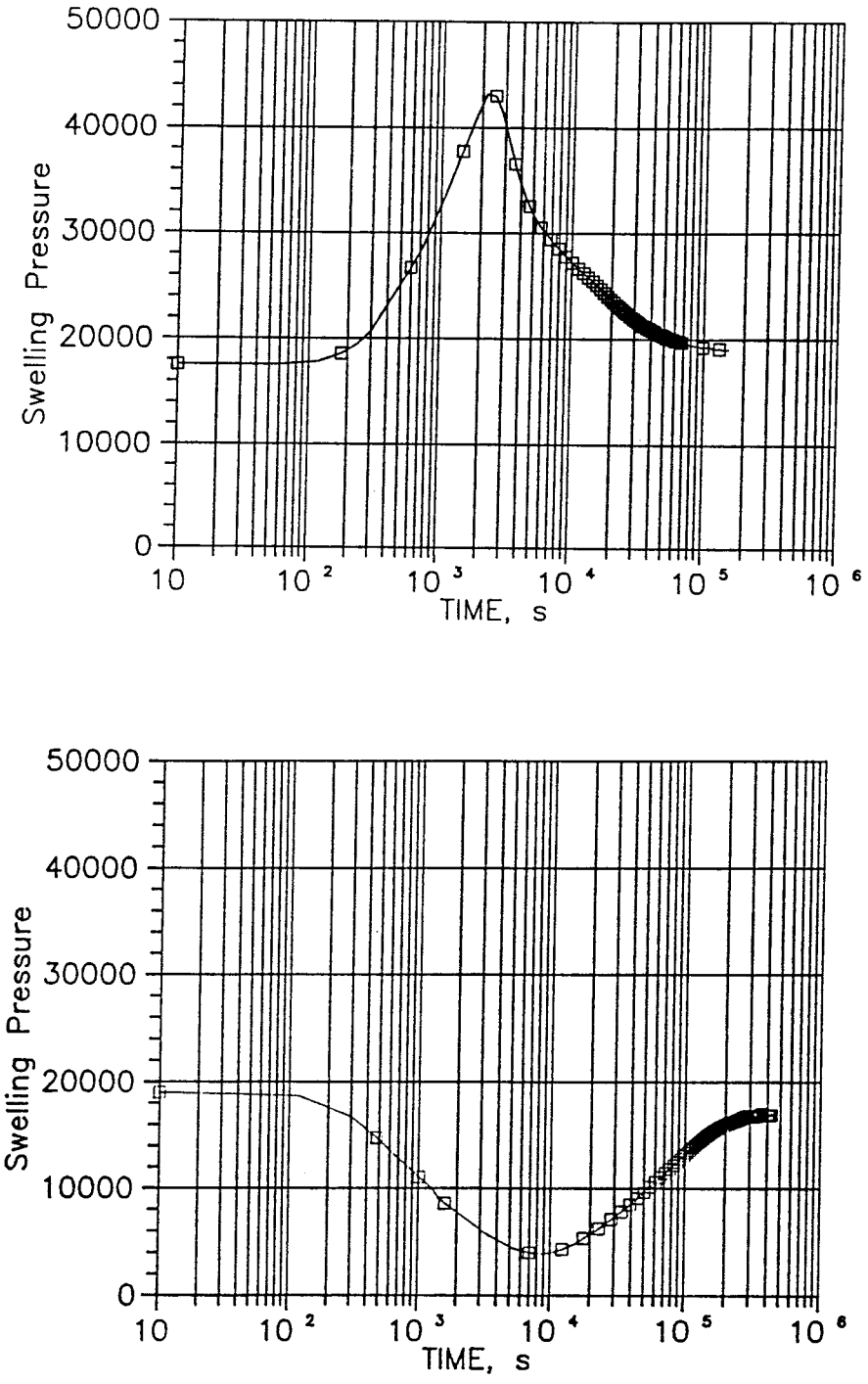

Figure 4-17: The measured axial pressure as a function of time after the start of the temperature increase (above) and after the start of the temperature decrease (below)

Temperature increase

The figures show that the pressure increased rapidly until a maximum was reached after 1000 to 2000 seconds, which corresponds to the time at which the new temperature was reached. After that the pressure was slowly dropping until equilibrium was reached after about 10^5 seconds.

Temperature decrease

After cooling to room temperature the change in pressure was less dramatic, i.e. with a smaller pressure change and a longer time for arriving at minimum pressure and equilibrium. The longer time to reach minimum pressure was caused by lack of cooling device, while the long time to reach equilibrium was caused by the lack of back-pressure on the pore water which prevented and equally high decrease in prepressure.

The results of these tests will be used for comparison with calculations accounted for later in the report.

4.2.1.5 Friction tests

A necessary parameter for the modeling is the friction between the clay buffer or backfill and the surrounding materials. Two major types of behavior can be identified:

- Slip at the interface between the clay and the contact material. This means that a special model for the interface is needed.

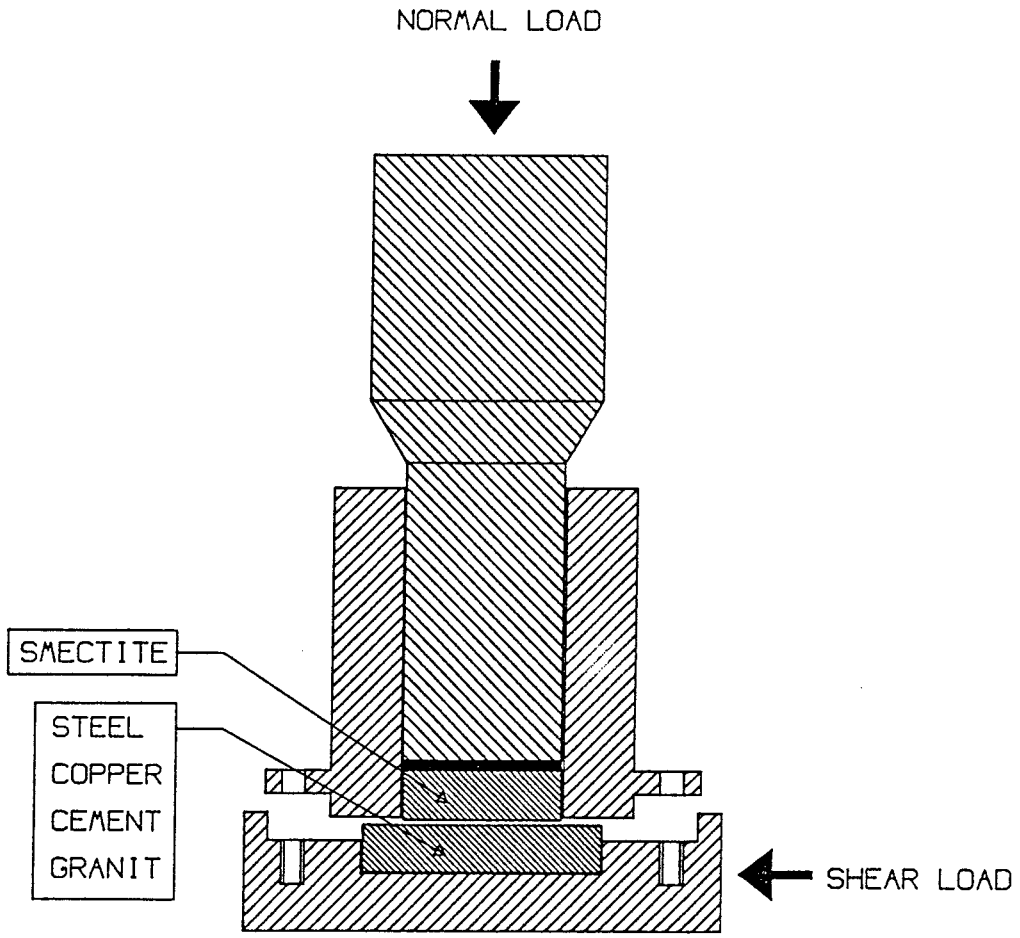

Figure 4-18: Schematic drawing of the shear box used for the friction tests

- The friction is so high, due to interaction with the contact material that slip will not occur at the interface but in the clay.

Friction tests have been performed on four different materials in contact with saturated Mx-80 sodium bentonite. One comparative test with only clay has also been performed. The density of the clay was ρ_m=2.0 t/m^2 and ρ_m=1.8 t/m^2 and the applied normal stress $\sigma_n \approx$5.0 MPa and $\sigma_n \approx$0.5 MPa.

The set up of the tests is shown in Fig 4-18. The sample was fixed in an oedometer ring in a direct shear apparatus and brought in direct contact with

the friction material. The oedometer ring was lifted 0.1 mm just before the test to ensure that there was no direct contact between the ring and the friction material.

The following four materials have been tested:

- Cement
- Stainless steel
- Copper
- Rock

The cement was cast with a smooth upper surface. The stainless steel and copper were also smooth but not polished. The rock surface was prepared by sawing.

Fig 4-19 shows the shear stress - deformation curves (τ-δ) from the five tests at two different clay densities. The tests were undrained and run as fast tests with failure achieved in about 10 minutes. The figure shows that only the cement/clay contact has a shear resistance that is higher than or equal to that of the clay. Copper, steel and granite have a similar and clearly lower contact strength. The brittleness is small with a residual strength of at least 90% of the peak value.

The measured values are quite high due to the high rate of deformation, i.e. 10^3-10^4 times faster than in common other shear tests.

The high shear resistance of the contact between clay and cement is probably caused by chemical reactions. Traces of that were found in the contact region.

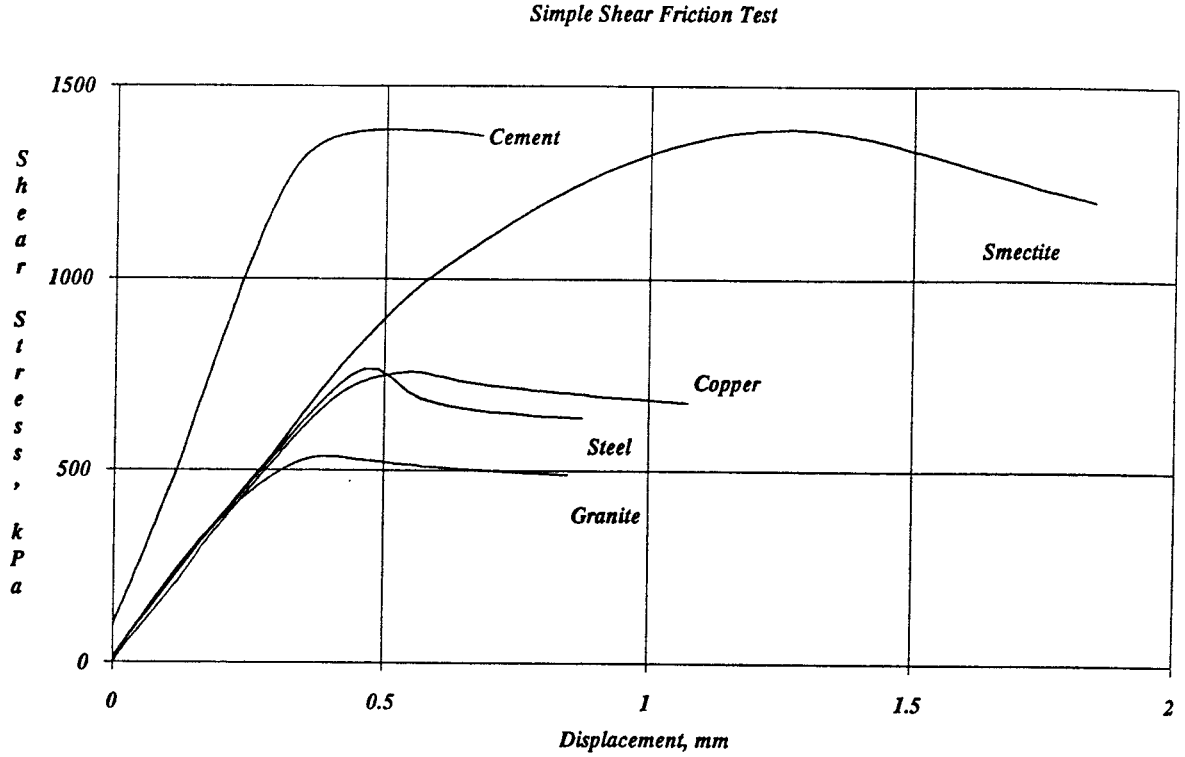

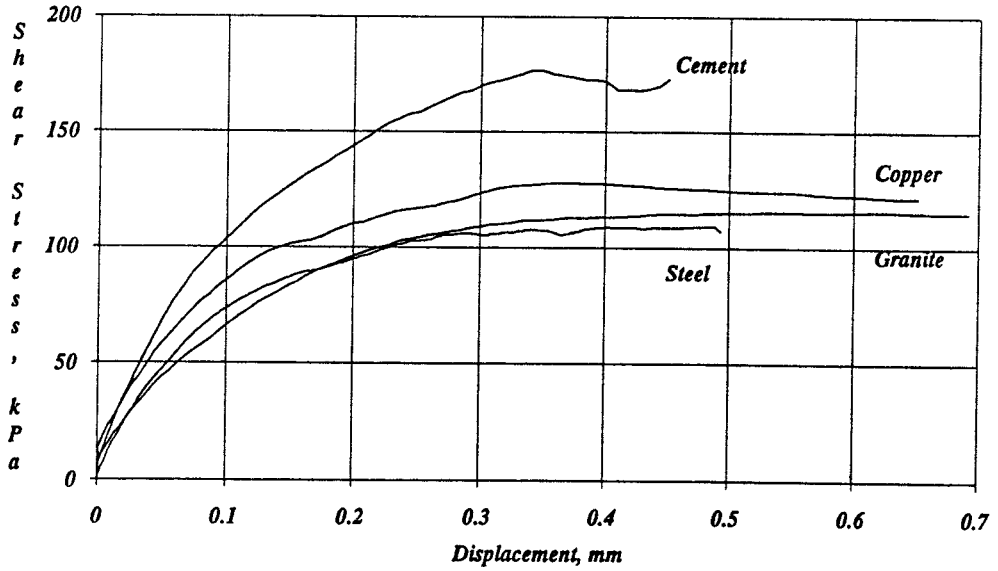

Figure 4-19: Results from the friction tests. The normal stress was 5 MPa in the tests shown in the upper diagram and 0.5 MPa in the lower diagram.

4.2.2 Porous elasticity model

Since the effective stress models involve changes in void ratio and pore pressure, the elements and the material models must contain these parameters. For modeling the elastic part of the behavior the porous elasticity model is very useful, as will be shown below.

The parameters needed for this model is the logarithmic bulk modulus κ and Poisson's ratio ν. The relation between the void ratio and the swelling pressure measured at isotropic constant volume tests is a straight line in a semi-logarithmic diagram as was shown in Fig 4-8. Thus, κ is easily determined as the inclination of the e-ln$p$ relation.

This yields for Mx-80 Na-bentonite:

$$\kappa=-\frac{\Delta p}{\Delta \ln e}=0.21$$

This expression is valid between $0.65<e<1.4$. At higher porosities, κ is higher while at lower porosities, κ seems to be somewhat lower.

If the measured radial pressure from the oedometer tests is used (which apparently is correct) the κ-value for Moosburg Ca-bentonite can be evaluated from Fig 4-7 which yields:

$$\kappa=0.17$$

It is not known within what limits this value applies, but it is assumed that it does not increase at high porosities as for Na-bentonite.

A determination of Poisson's ratio ν requires drained triaxial tests, performed under constant average stress p. Such tests have not yet been conducted, but

the general behavior observed at the drained and undrained tests indicate that ν is quite high and a probable value is

$\nu \approx 0.4$

4.2.3 Drucker-Prager plasticity model

Input data for the Drucker-Prager model can be taken from the triaxial tests. The yield surface and failure surface can be modeled according to Fig 4-20, in which they are plotted together with the results from the triaxial tests.

This evaluation gives the parameters (see chapter 2.2):

$\beta = 20^{\circ}$
$d = 100$ kPa

The parameters K and ψ have not been determined. They require that more drained triaxial tests must be performed. The tests made so far indicate that $K<1.0$ (≈ 0.9) and that the flow is non-associated and thus $\psi<\beta$ but due to the lack of information the classical Drucker-Prager has been applied in the calculations which yields

$K = 1.0$
$\psi = 20^{\circ}$

What remains to be determined is the yielding function f. This function describes the plastic strain ε_y as a function of the Mises stresses in the plastic region. The yield function can be given in the form of a table containing $\sigma_j - \sigma_j^y$ and ε_y where σ_j^y is the Mises stress at the yield surface. The yield function is derived from a stress path with

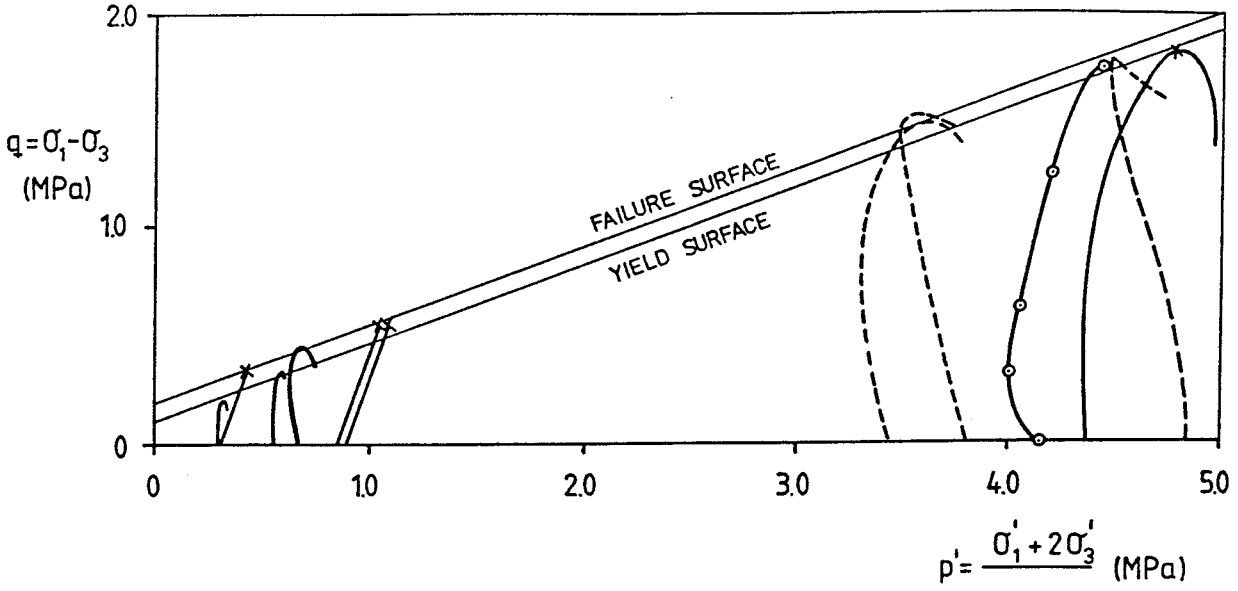

Figure 4-20: Evaluated yield surface and failure surface in the Drucker-Prager model

constant minor principal stress $\sigma_3=\sigma_2$ and an increased deviatoric stress p $(=\sigma_j)$, which means the same stress path as a drained triaxial test.

Considering that failure in drained triaxial tests occur after about 10% strain it is reasonable to use the following yield function, which is based on Fig 4-20 assuming a very thin plastic zone:

Table 4-1 Yield function for the Drucker-Prager model

$\sigma_j-\sigma_j^y$ (kPa)	ε_y
0	0
25	0.005
50	0.02
75	0.04
100	0.1

The advantage of this model is that it fits well with the behavior of smectite-rich clay in the sense that it has a large elastic zone with recoverable strain and insignificant cohesion. The lack of a "cap" is positive because the strong expansibility seems to destroy most of the over consolidation effects.

The disadvantage of the model is that the plastic zone has the same thickness irrespective of the average effective stress. This is not correct since it means that the stress-strain curve has a shape that strongly depends on the void ratio,which contradicts all measurements. Another behavior, that does not agree with experience, is that once the yield surface has been moved it cannot be removed in spite of the swelling properties.

A technique to overcome these disadvantages would be to make the plastic zone very small and almost non-existent from the beginning, but this means that the stress-strain relation will have a sharp corner at yielding.

An improvement of the model would be to allow the failure surface and the yield surfaces to have different inclinations in the p-q plane.

4.2.4 Critical State model

The Critical State theory, including the Cam Clay model, is a compromise between the actual behavior of a non-swelling clay and the possibility to make a model that works with respect to plasticity theory. Like the Drucker-Prager model this model cannot be adapted without care to the properties of a swelling clay.

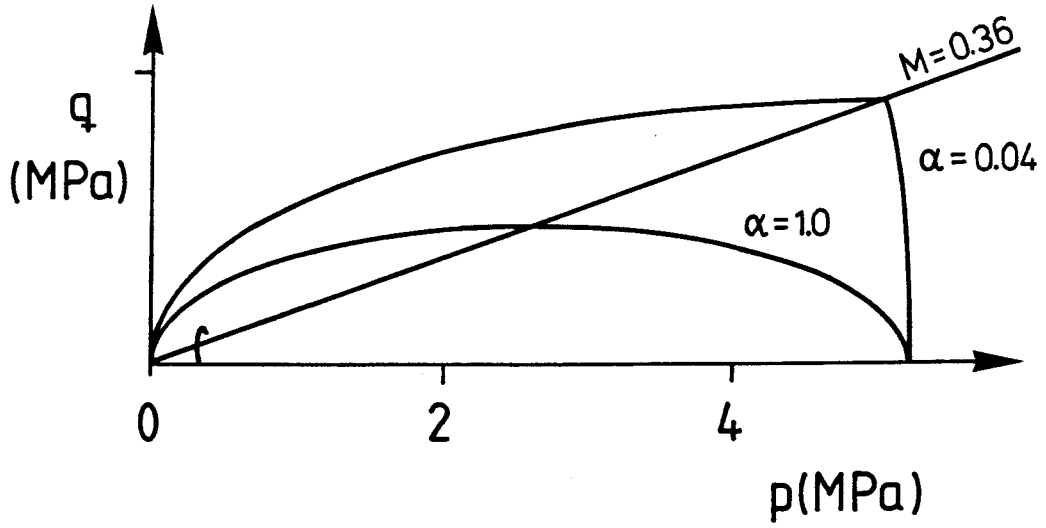

Figure 4-21: Illustration of two different yield surfaces in the Critical State model

The critical state line is determined by the parameter *M*. Since it is a straight line through origo in contrast to the measured curved failure line, *M* cannot be determined as a general value but must be adapted to the stress level. At the average effective stress p'=5.0 MPa the *M*-value is

M=0.36

The yield surface is determined by the parameters a_0 and α. Fig 4-21 shows two possible appearances of the yield surface:

a_0=5.0 MPa
α=0.04

or

a_0=2.5 MPa
α=1.0

None of these is very satisfactory. As was seen in triaxial test No. 6, in which the sample was allowed to swell from an initial pressure of 10 MPa to 0.67 MPa and then sheared to failure, the effect of an over consolidation is strongly overestimated in this model. If α=0.04 the yield surface is extremely high at lower stresses. On the other hand if α=1.0 the behavior at normal consolidation seems to be somewhat incorrect. Tests are being conducted in order to find the optimum character of the yield surface.

The volume change behavior at increasing p' in the plastic region is determined by the parameter λ. Since the swelling and consolidation properties seem to be similar it is logical to use $\lambda \approx \kappa$. This yields

λ=0.22

K is given the same value as in the Drucker-Prager model:

K=1.0

This model obviously does not behave very well at high over consolidation ratios. An improvement would be to change the shape of the yield surface on the dry side and make it run close to the critical state line.

4.2.5 Thermomechanical model

The thermomechanical model is a combination of the porous elasticity model and one of the plasticity models presented. A change in k-e relation should be made at higher temperatures as shown in Fig 4-14. The bulk modules and the coefficient of thermal expansion can be given the values shown in chapter 2.6.2.

4.2.6 Friction models

The laboratory friction tests show that there is a slip between the clay and the surface of most smooth materials. The contact area can accordingly be modeled with friction elements. These element are given the property of allowing no slip at all until the shear stress exceeds a value determined by the friction angle, after which the shear resistance is constant, provided that the normal stress does not change.

The friction angle ϕ_f at shear between a smectite clay and a smooth material can be given the following values in relation to the friction angle ϕ_f of the clay according to the measurements shown in Fig 4-19:

- Cement/clay: $\phi_f=\phi_c$ (no slip)
- Stainless steel/clay: $\phi_f=0.6\phi_c$
- Copper/clay: $\phi_f=0.6\phi_c$
- Granite/rock: $\phi_f=0.6\phi_c$

In the friction element the shear stiffness of the contact also needs to be described. This is done by the parameter "stiffness in sticks" defined as the required shear stress at slip divided by the deformation at slip:

$$G=\frac{\tau}{\delta_s} \qquad (4:3)$$

This parameter is not well known but a very high stiffness is assumed, meaning that almost no shear takes place before slip.

4.3 General comments

The models are under development and laboratory tests are being conducted to further develop them. The models and data presented are based on the knowledge today and should be treated as preliminary.

The models are developed for Na-bentonite but can can be applied to Ca-bentonite as well with the following changes:

- κ=0.17 in the porous elasticity model
- β in Drucker-Prager and M in Critical state models can be taken from Fig 4-1
- λ=0.18 in the Critical state model

The influence of temperature seems to be small. The influence is significant on the hydraulic conductivity (Fig 4-14) and on the e-p relation at high void ratios.

The influence of the rate of deformation on the strength can be considered using Eqn 4:1.

5. VERIFICATION TESTS

Primarily, three models, one total stress model and two effective-stress models for simulating the geotechnical behavior of buffer material have been worked out. The total stress model has been treated and verified in earlier reports [3],[5]. The more complex effective stress models are not fully developed but the preliminary versions presented in chapter 4 have been used in finite element calculations with the program ABAQUS.

Some of the more advanced laboratory tests have been used as verification tests. The tests are simulated by establishing a finite element model with identical dimensions, applying relevant boundary conditions, assigning to the elements, proper combinations of material models and then finally changing the boundaries in a way that simulates the test procedure.

Most of the tests simulated in these calculations are not true verification tests since the tests themselves have contributed to the material models. The thermomechanical tests are an exception since they have not contributed to the indata of the model.

The models and the calculation techniques need thus to be further tested in true verification tests (like the rock shear and settlement tests). The calculations presented in this chapter have been done during the development work and will to some extent show the applicability and the limitations of the technique and whether changes or further developments are required.

5.1 UNDRAINED TESTS

The undrained triaxial test No. 4 has been simulated using the two different effective stress models:

GEOMETRY
- Diameter: 5 cm
- Height: 10 cm

BOUNDARIES
- Filter stones at both ends
- Stiff ends
- Completely raw ends
- Equal pore pressure along end surfaces
- Free expansion axially

SAMPLE
- MX-80 Na-bentonite

CONDITION
- ρ_m=2.00 t/m^3
- e=0.79

The following test procedure is selected:

STEP 1
- external constant pressure σ'=4.4 MPa
- initial pore pressure u=0

STEP 2
- Axial displacement of end surfaces
- Strain rate $\dot{\varepsilon}=1.43\cdot10^{-7}$ 1/s

The geometry is modeled using axisymmetric elements according to Fig 5-1. The lower end is a symmetry plane. The calculation was done with the two effective stress models.

5.1.1 Critical State model (CS-model)

The indata for this model is

Plasticity:
- λ=0.22
- M=0.37
- α=0.04

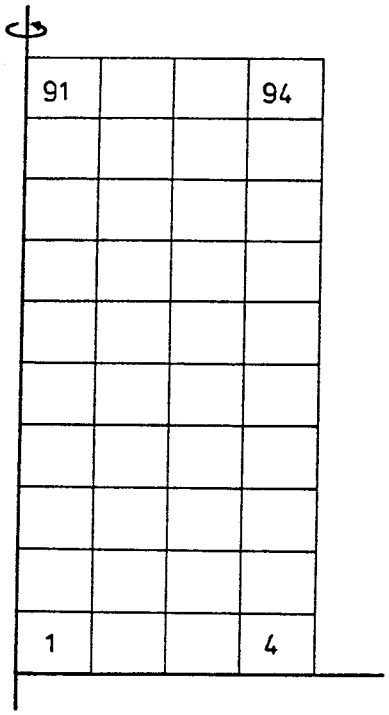

Figure 5-1: Element mesh used in the triaxial test calculations. The left boundary is a symmetry axis and the lower boundary is a symmetry plane.

a_0=4200 kPa
K=1.0

Porous elasticity: K=0.21
ν=0.4

Pore properties: $k=1.0\cdot10^{-13}$ m/s
ρ_w=1.0 t/m^3
$B_w=2.1\cdot10^6$ kPa

Initial conditions: e_0=0.79
p_0=4400 kPa

One element test (idealized)

The indata are checked by making an idealized simulation of the test using only one axisymmetric element. This is the way the triaxial test originally is assumed to perform. In such a calculation no end friction and no variation in pore pressure distribution in the sample can occur. The results of the one-element calculation are shown in Fig 5-2.

The stress-strain relation is in this idealized example very simple with a linear increase in deviatoric stress q accompanied by a linear increase in pore pressure u, which corresponds to a constant effective average stress p until the critical state line (CSL) is reached, where the material fails under constant u and q.

This behavior is idealized, but, as will be seen in the subsequent presented "realistic calculation", the end friction and the variation in pore pressure in the sample will change the behavior.

40 elements test (realistic calculation)

The calculation using the element mesh shown in Fig 5-1 implies simulation of an axial compression of 10 mm, corresponding to ε=20 %. The following relations, derived in the calculations, are shown in Figs 5-3 and 5-4:

- pore pressure/deformation u-ε
- void ratio/deformation e-ε
- deviator stress/deformation q-ε
- deviator stress/average stress q-p

Fig 5-3a shows the pore pressure development in the filter stone as a function of the axial compression,

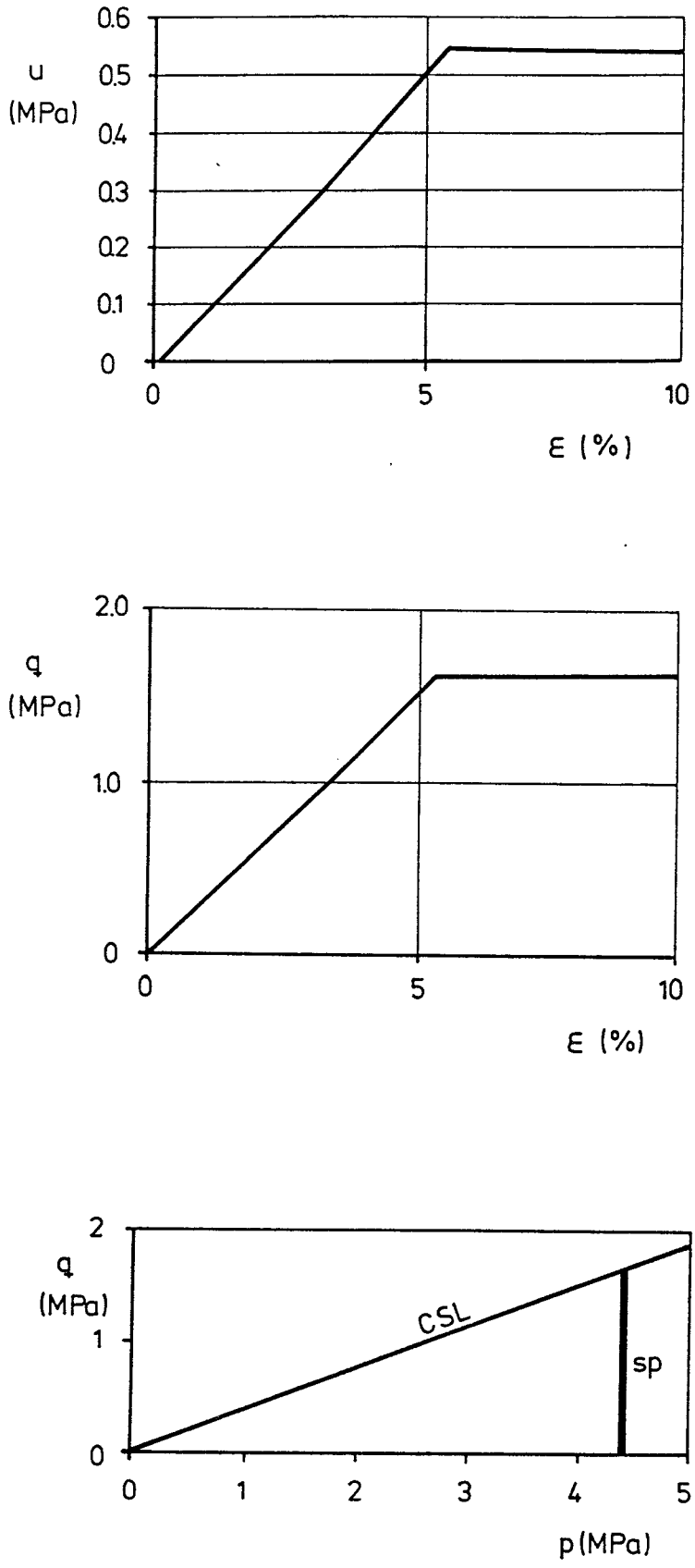

Figure 5-2: Results from the idealized one-element test

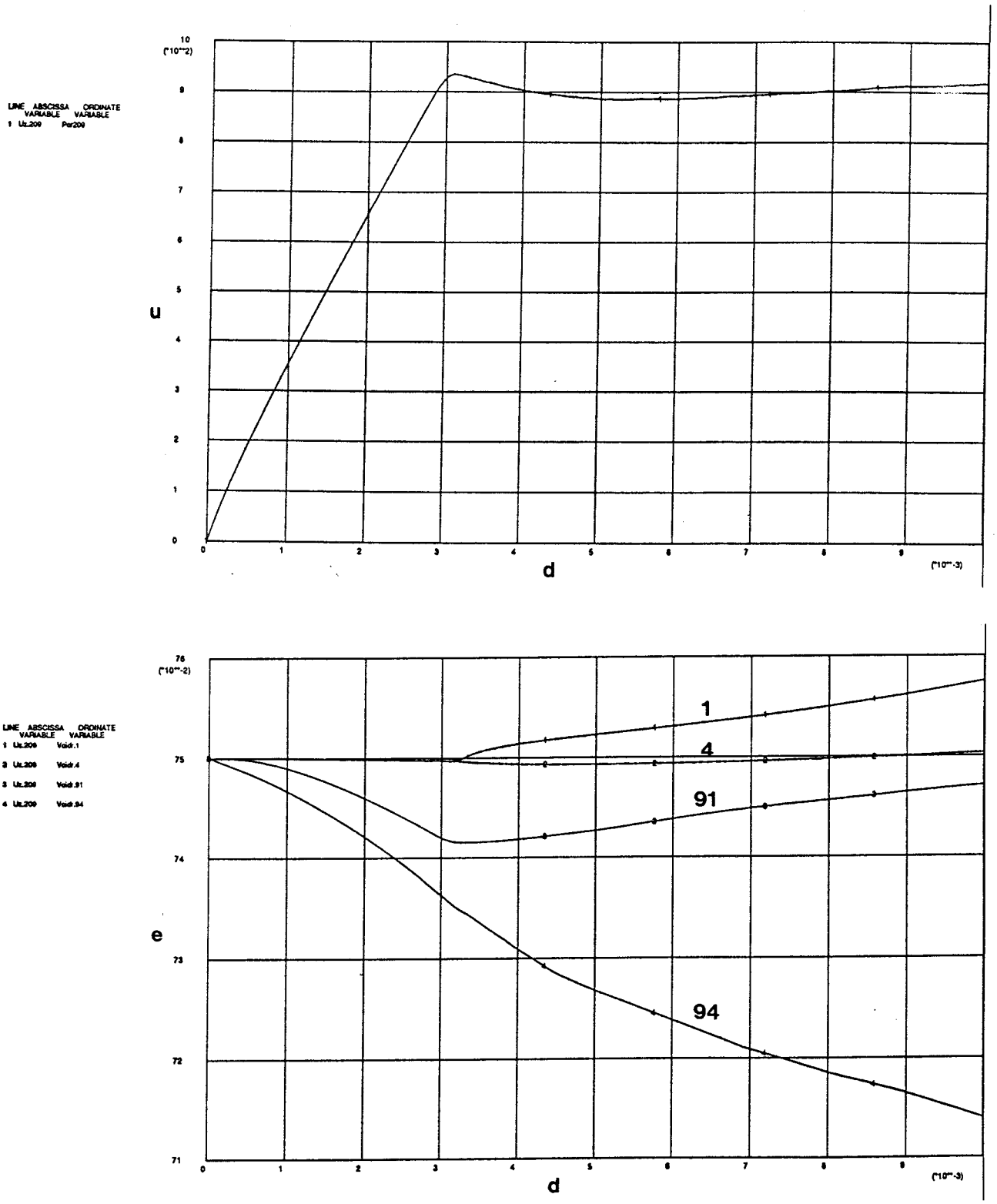

Figure 5-3: Results from the calculation.

Upper: pore pressure (kPa) - axial displacement (m)

Lower: Void ratio - axial displacement (m) in elements 1, 4, 91 and 94

(*10**X) means 10^{x}

while Fig 5-3b shows the void ratio in four of the elements (marked in Fig 5-1). It is interesting to see that the void ratio is changing a little, especially in element 94 which has an challenging position, in spite of the undrained condition. The reason for this is of course the uneven stress distribution in the sample.

The stress-strain relation and the stress path of the same elements are shown in Fig 5-4. Elements (1 and 4) behave similarly to the element in the idealized test.

Figs 5-5 and 5-6 show contour plots of

- deformation δ
- void ratio e
- pore pressure u
- deviator stress q

after 8% and 20% deformation in the right upper quarter of the sample. The contour plots show that the sample is deformed like a barrel due to the friction between the sample and the filter stone. The e-plots show that the change in void ratio is concentrated to the upper right corner. The q-plots show that the deviatoric stresses in the upper 25% of the sample differ very much from the average, while the u-plots show that there is a pore pressure difference between the centre of the sample and the filter stone of about Δu=300 kPa.

In a real triaxial test all these things are not measured. The only parameters that are recorded are

- the total deformation ε
- the total axial force (yields $q_{average}$)
- the pore pressure in the filter stones u

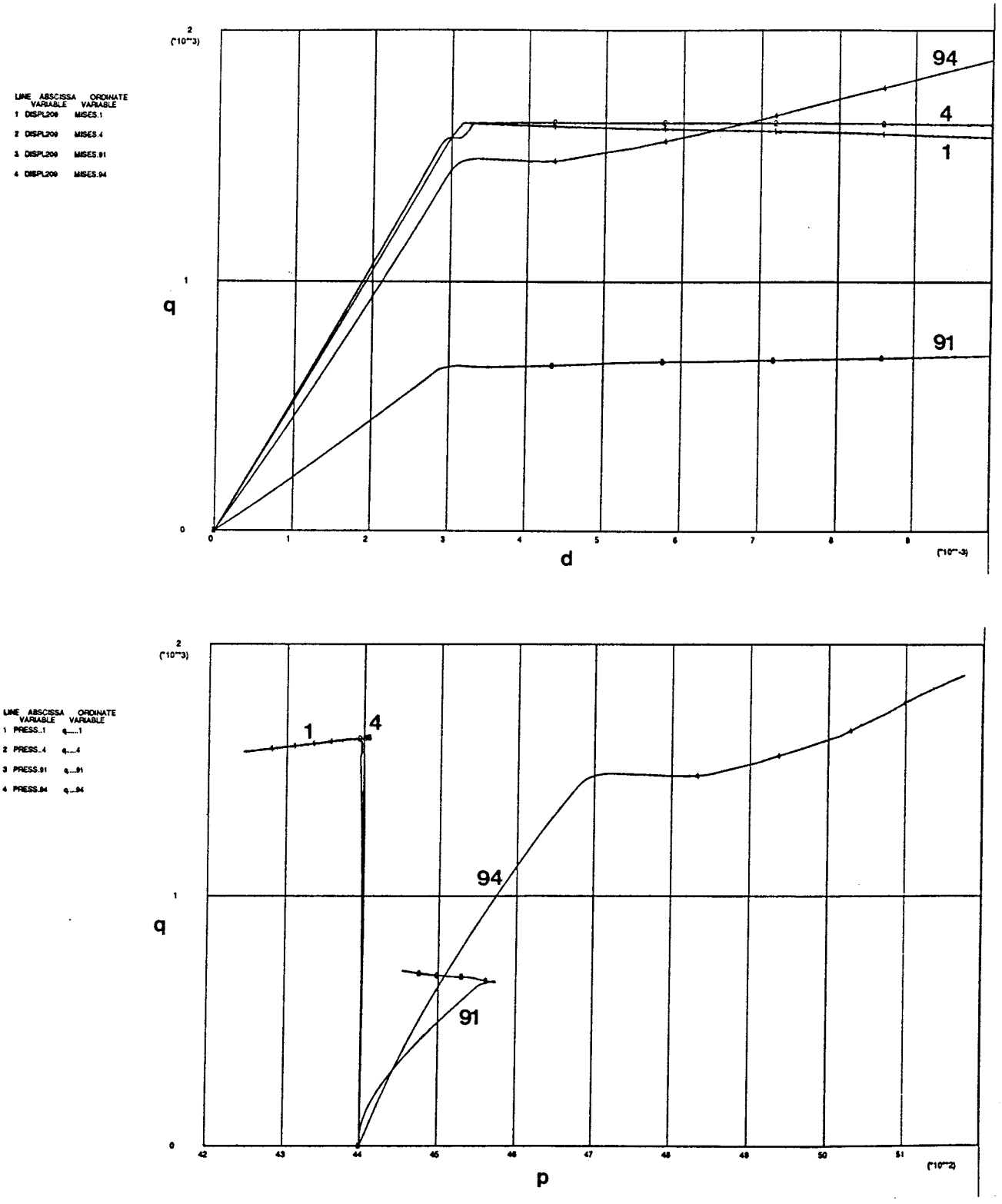

Figure 5-4: Results from the calculation in elements 1,4,91 and 94 using the CS model
Upper: Mises stress (kPa) - displacement (m)
Lower: Mises stress (kPa) - average stress (kPa)

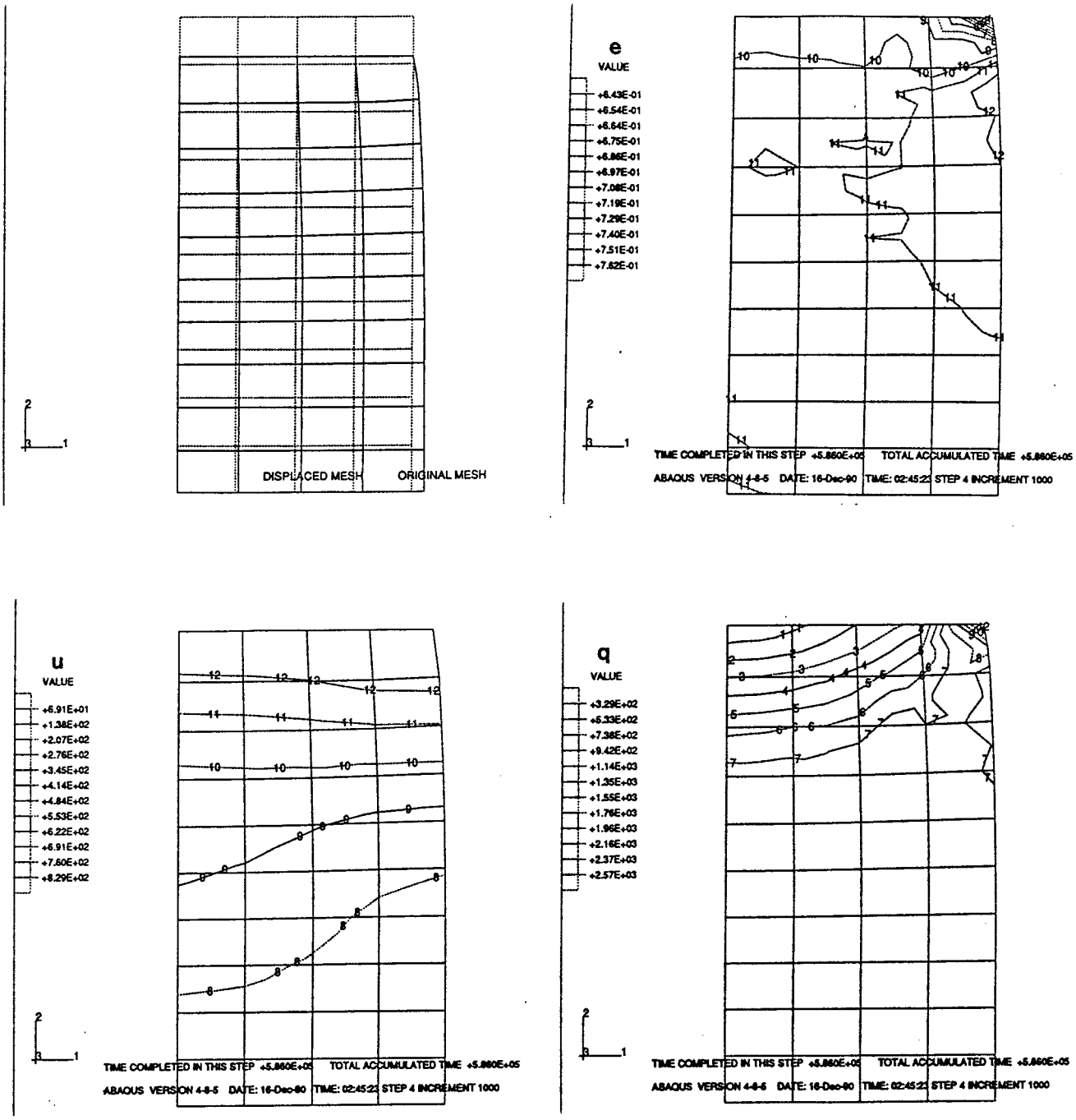

Figure 5-5: Contour plots of: Displacements (upper left), void ratio (upper right), pore pressure in kPa (lower left) and Mises stresses in kPa (lower right) at 8% axial deformation. CS model

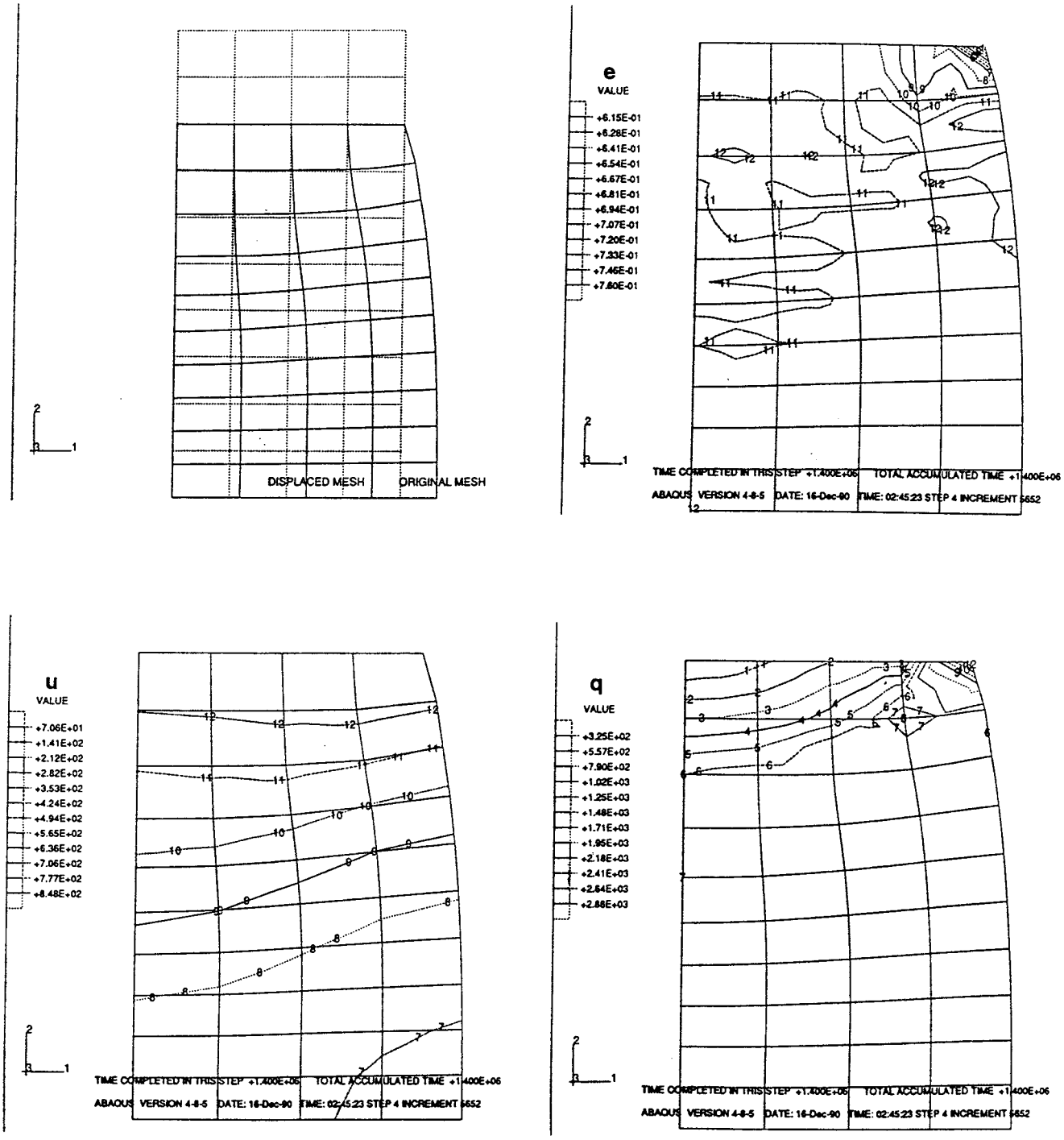

Figure 5-6: Contour plots of: Displacements (upper left), void ratio (upper right), pore pressure in kPa (lower left) and Mises stresses in kPa (lower right) at 20% axial deformation. CS model

The plots from a real test is thus based on these measurements. If the simulated test is evaluated in the same way the results would be those indicated in Fig 5-7 (and the relation u-ε in Fig 5-3).

The big difference between the first, idealized calculation with one element and the latter, realistic one, is the stress path and the pore pressure development. The reason for this difference is, as was shown in the u-plots, that the pore pressure measured in the filter stones is higher than in the centre of the sample and the evaluated effective stress path is thus not correct. The rate of deformation in the real tests are therefore too high according to this calculation.

5.1.2 Drucker-Prager model (DP-model)

The indata for this model is

Plasticity: $\beta=20^{\circ}$
$d=100$ kPa
$\psi=20^{\circ}$
$K=1.0$

Yield function: See Table 4-1 chapter 4.2.3

Porous elasticity: $K=0.21$
$\nu=0.4$

Pore properties: $k=1.0\cdot10^{-13}$ m/s
$\rho_w=1.0$ t/m^3
$B_w=2.1\cdot10^{6}$ kPa

Initial conditions: $e_0=0.79$
$p_0=4400$ kPa

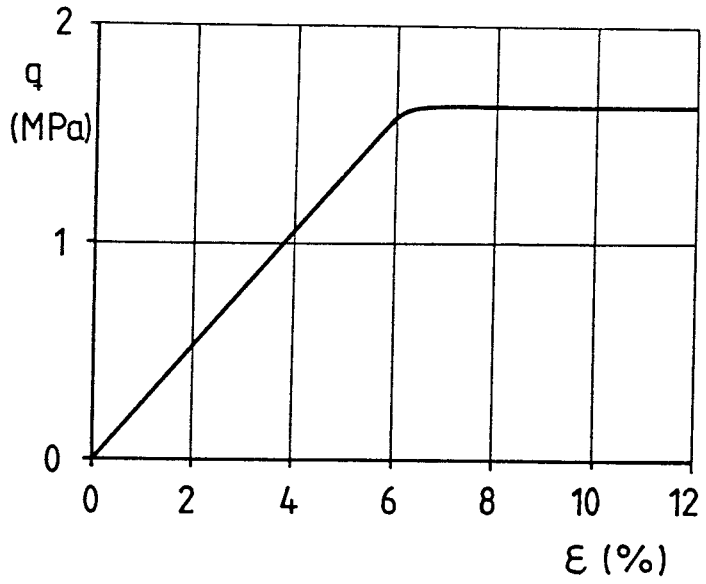

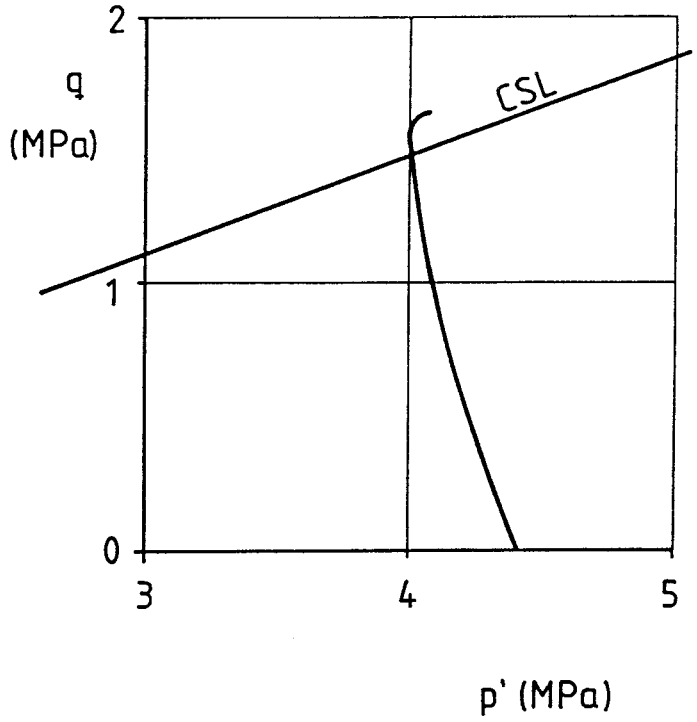

Figure 5-7: The calculated undrained test evaluated in the same way as a real test. The stress path and the stress-strain relation are shown. CS model

Some results from the calculation are shown in Figs 5-8 to 5-11. The pore pressure development shown in Fig 5-8a is different from the one obtained from the CS-model. After reaching the yield surface at 6% strain at a similar pore pressure, the sample starts to dilate, the pore pressure decreases and becomes negative after large strain.

The dilation is reflected in the q-ε and q-p plots. The sample never comes to failure but follows the failure surface towards high average stresses. Fig 5-10 shows the same four contour plots as was shown from the CS-model, but only after completion at ε=20%.

If the test is evaluated in the same way as a real test, the results shown in Fig 5-11 would be obtained. The dilation obviously yields a behavior that is not recorded in real tests.

5.1.3 Comparisons with the real test

In Fig 5-12 the calculated stress paths are plotted in the same diagram as the measured stress paths. The plot shows that:

- The calculated stress paths are more inclined towards the q-axis. This is because the calculated pore pressure is higher than the measured.

- The D-P calculation goes beyond the failure line while the CS calculation gives a correct failure.

-The tendency of the sample to dilate at failure is in agreement with all measurements but exaggerated in the D-P calculations.

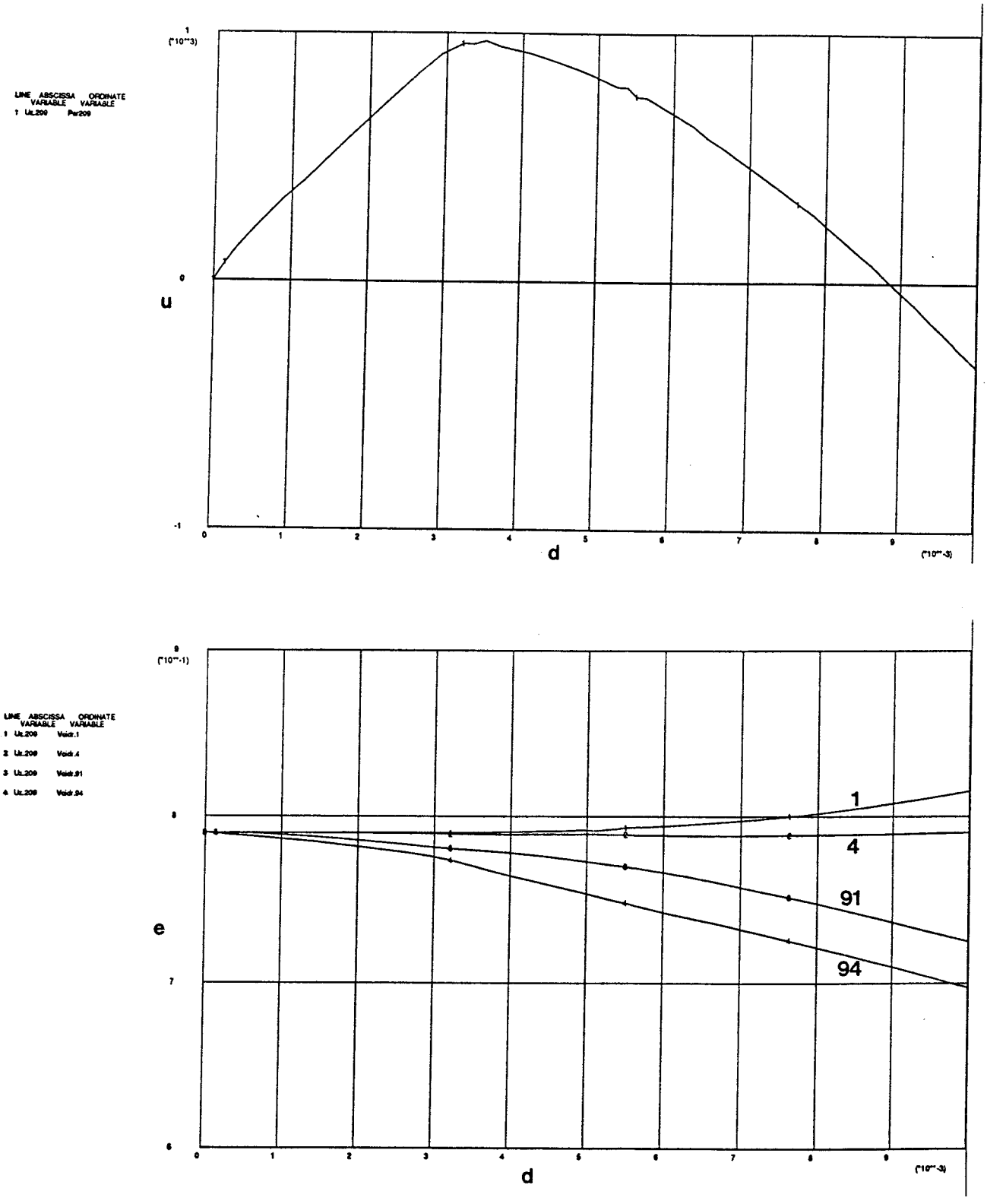

Figure 5-8: Results from the calculations using the D-P model.
Upper: Pore pressure (kPa) - axial displacement (m)
Lower: Void ratio - axial displacement (m) in elements 1, 4, 91, 94

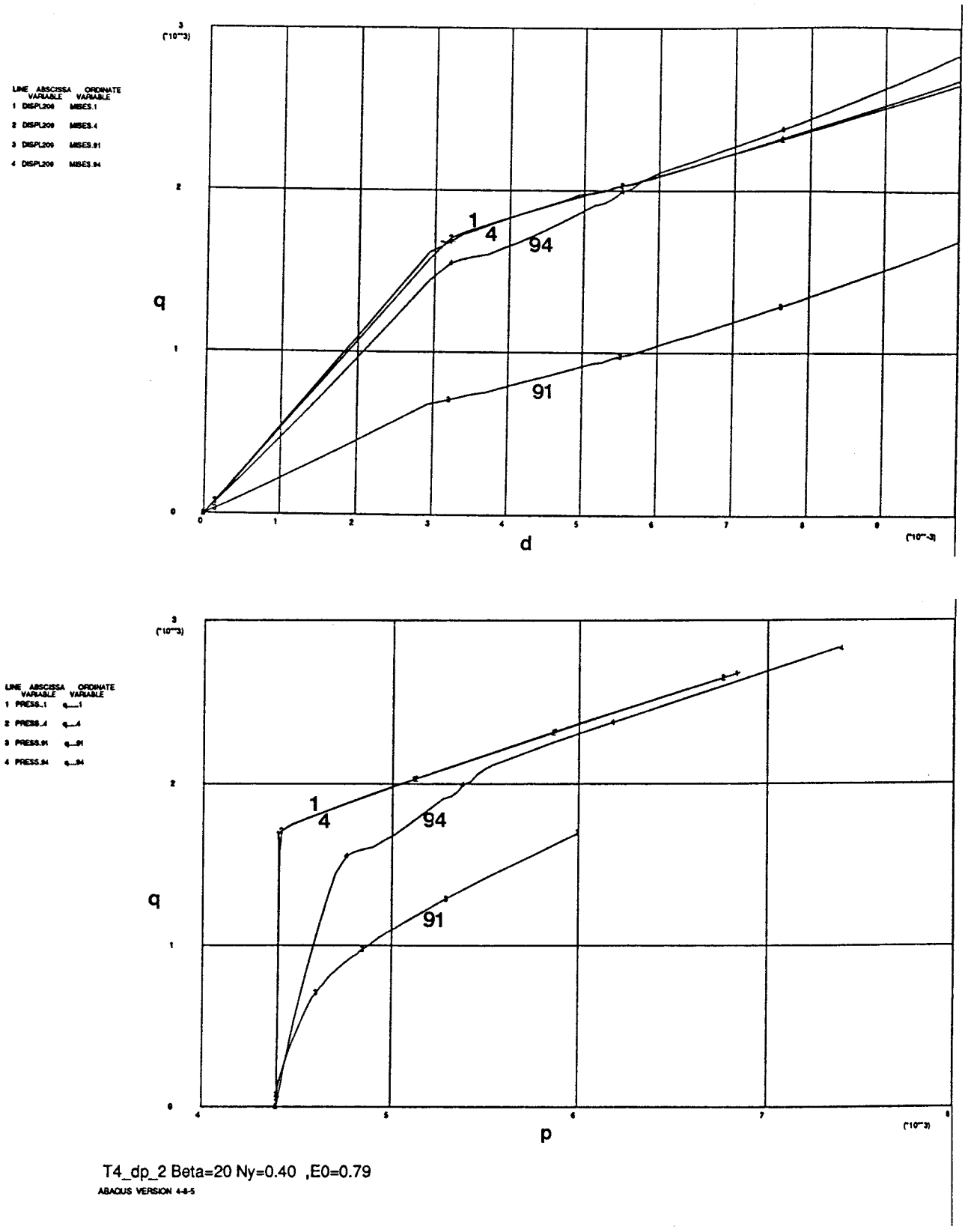

Figure 5-9: Results from the calculations in elements 1, 4, 91 and 94 using the D-P model.
Upper: Mises stresses (kPa) - axial displacement (m)
Lower: Mises stresses (kPa) - Average stress (kPa)

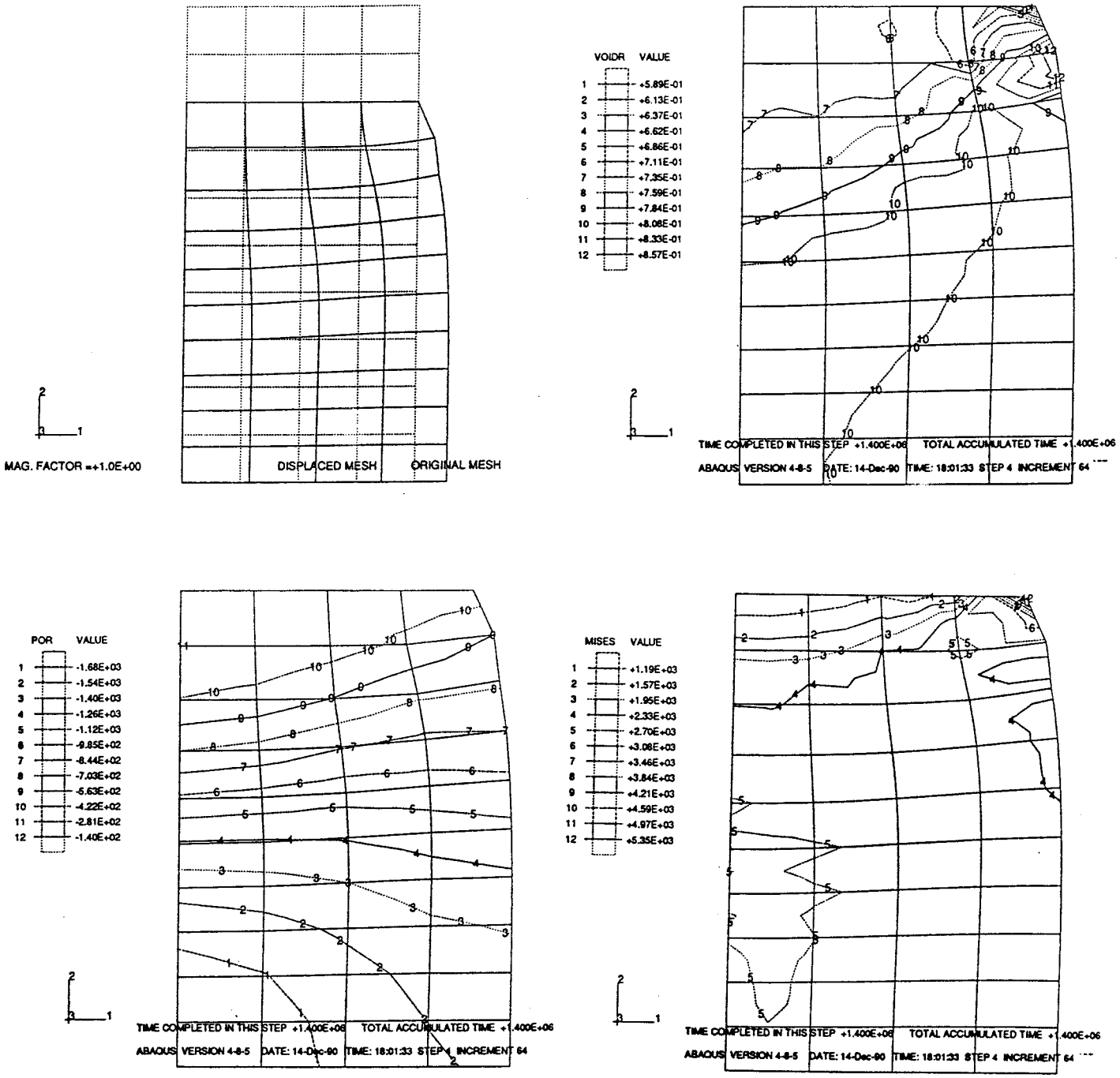

Figure 5-10: Contour plots of: Displacements (upper left), void ratio (upper right), pore pressure in kPa (lower left) and Mises stresses in kPa (lower right) at 20% axial deformation. D-P model

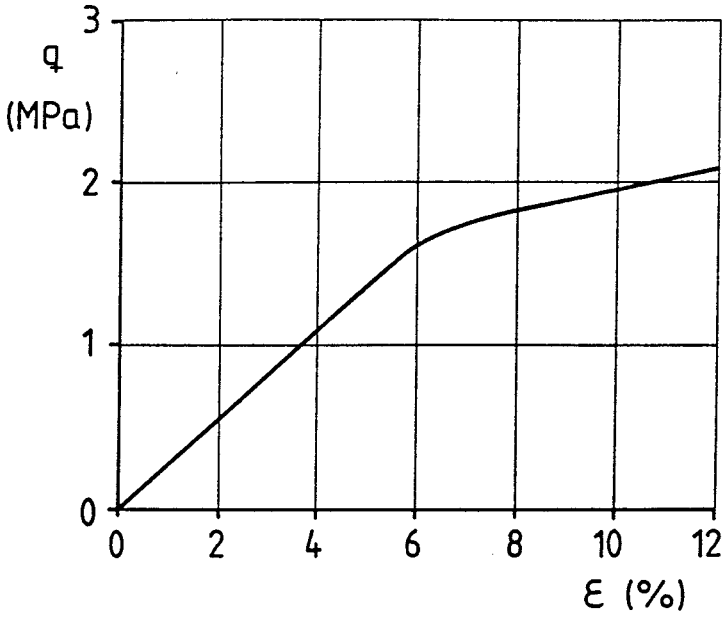

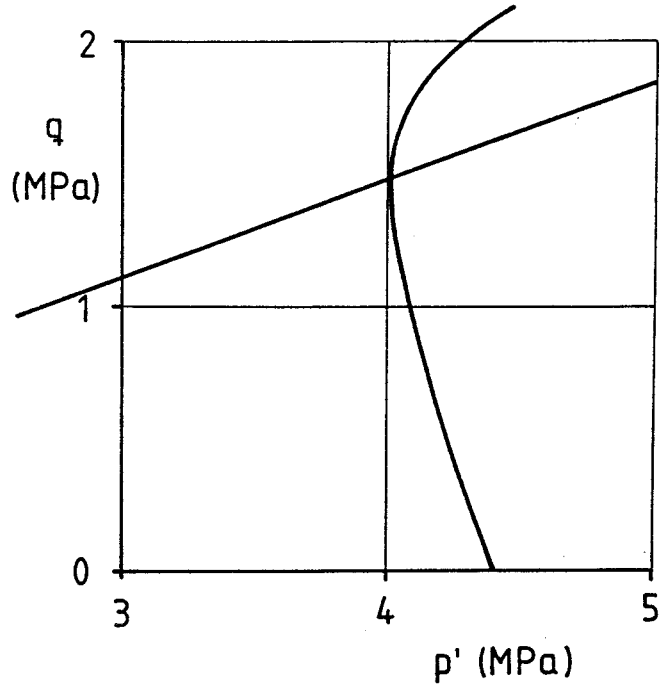

Figure 5-11: The calculated undrained test evaluated in the same way as a real test. The stress path and the stress-strain relation are shown. D-P model

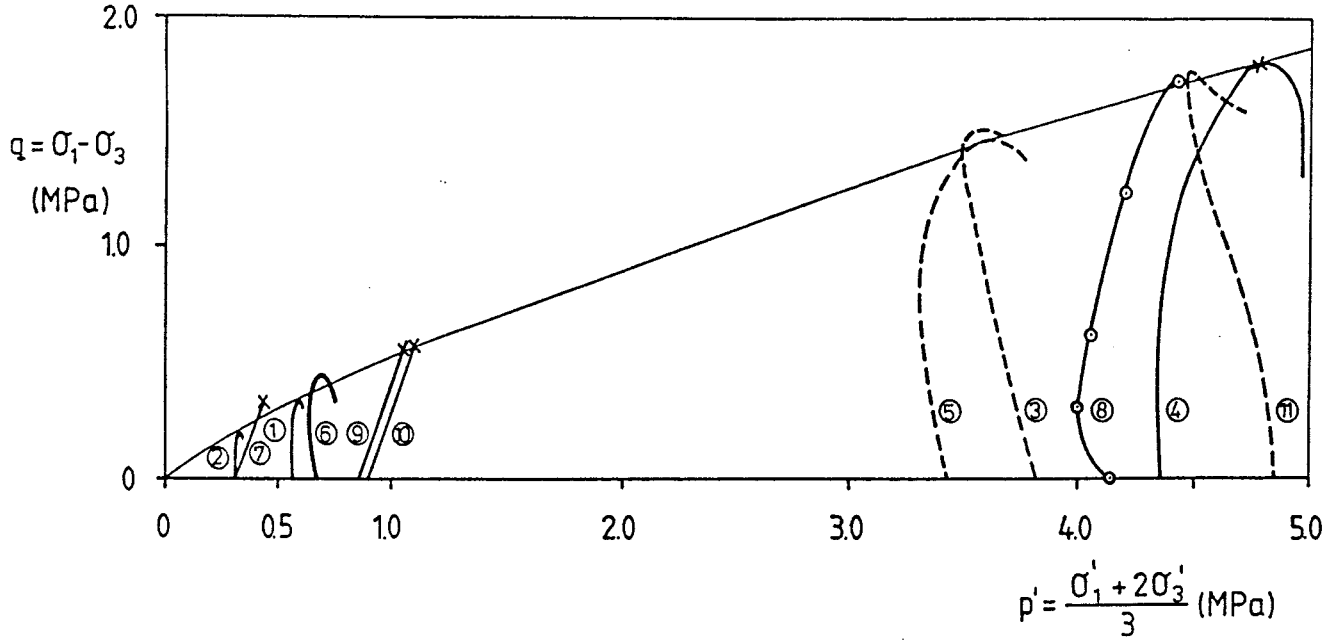

Figure 5-12: The two calculated stress paths plotted among the measured stress paths

- There is a scatter in stress path inclination before failure among the real tests but two of these tests behave according to the calculations.

The measured q-ε and u-ε relations are shown in Fig 5-13. The dilation is obviously quite large and, in at least one of the filter stones, the pore pressure becomes negative in relation to the start value. The low residual q-value is caused by slip failure in the sample, a process that cannot be achieved in the calculations since the element mesh is axisymmetric.

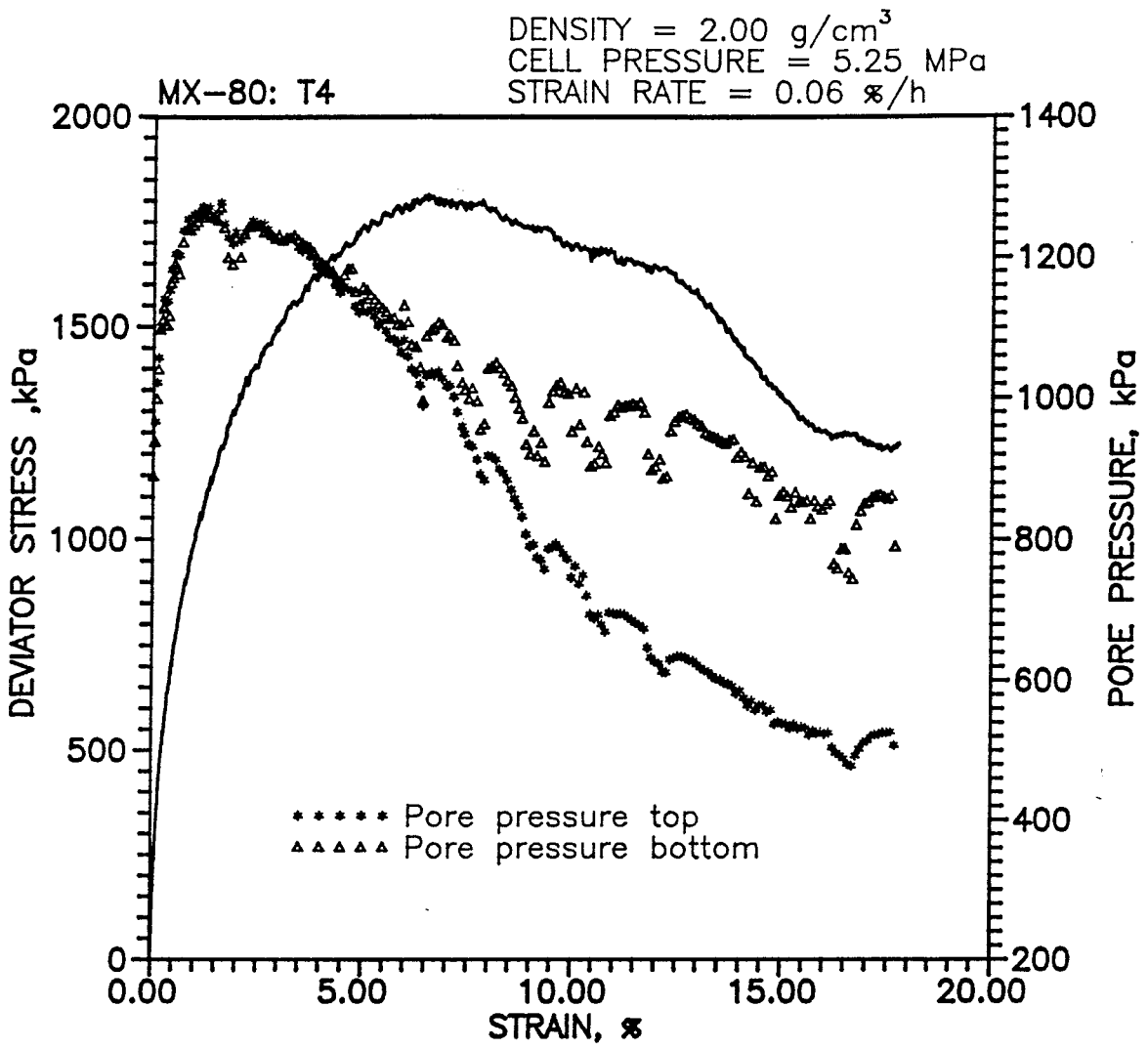

Figure 5-13: The measured deviator stress and pore pressure as a function of the strain in the real test

5.1.4 Conclusions

The calculations agree fairly well with the measurements, although the DP-model dilates too much. Adjustments of the existing models can probably improve the results considerably. The high dilatancy of the DP-model can be decreased by putting $\psi<\beta$ and thus making the plastic flow non-associated. Another conclusion is that the rate of strain in the real tests are probably too high.

Attempts will be made to integrate the "physico/-chemical" models, as outlined in a parallel study and the present rheological models.

5.2 DRAINED TESTS

The oedometer swelling and compression tests have been simulated. Swelling is a problem for the CS-model in the present form because of the elliptic yield surface that allows very high deviator stresses on the dry side. The CS-model is obviously not a good one when swelling is involved. For this reason, the CS calculations in swelling tests will not be presented in detail. Attention will instead be paid to the calculations in which the DP-model was used.

The swelling/compression test shown in Fig 4-6 has been simulated. Several calculations have been made using different element models, different material models and different friction models. These calculations are not finished yet and the test is thus not completely analyzed.

Two examples will be shown in this chapter. The first one simulates the whole test with unloading and reloading but without analyzing the time-dependent evolution of each load step. It assumes that there is no friction between the walls in the oedometer ring and the sample. The second one simulates one load step including the time process. In this simulation friction as well as absence of friction have been analyzed.

5.2.1 The complete unloading and reloading oedometer test

The element mesh shown in Fig 5-14 has been used in the calculations. The elements are axisymmetric

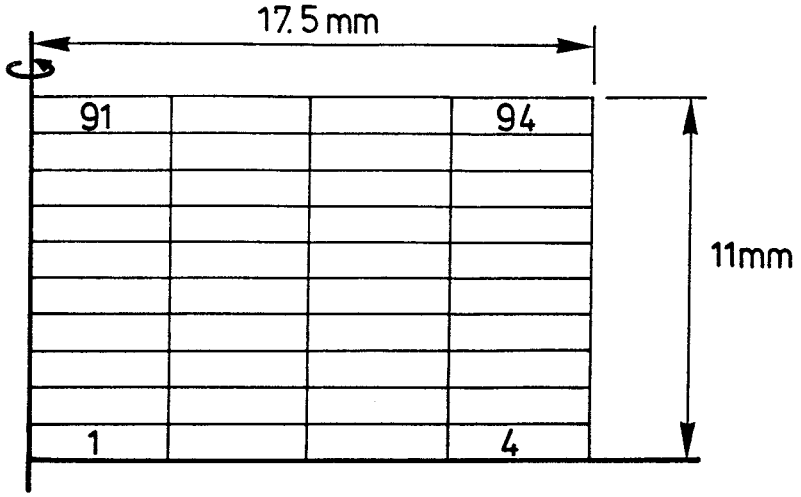

Figure 5-14: Element mesh in the oedometer calculation

around the left boundary and the bottom boundary is a plane of symmetry.

The calculation using the Drucker-Prager plasticity model and the porous elasticity model will be reported. The model parameters are:

Plasticity:	$\beta=20^{\circ}$
	$d=100$ kPa
	$\psi=20^{\circ}$
	$K=1.0$
Yield function:	See Table 4-1 chapter 4.2.3
Porous elasticity:	$K=0.21$
	$\nu=0.4$
Pore properties:	$k=1.0\cdot10^{-13}$ m/s
	$\rho_w=1.0$ t/m^3
	$B_w=2.1\cdot10^{6}$ kPa
Initial conditions:	$e_0=0.77$
	$p_0=5000$ kPa

The sample is initially 22 mm high and 35 mm in diameter. It is allowed to swell 10 mm and is then compressed back to its original height. Fig 5-15 shows the results of the calculation. The upper diagram shows the stress path in p-q diagram form, while the lower one shows the stress-void ratio relations.

The stress path diagram shows that the devatoric stresses are quite high in the test, while the σ-e diagram shows that the resulting axial and radial stresses differ very much at high void ratios. The latter diagram also shows that there is a considerable hysteresis in axial stress while the hysteresis is smaller in radial stress.

In the real test the radial stress was measured in the centre of the sample. If the influence of friction against the oedometer ring is neglected (as in the calculation) and if the radial and axial stresses are considered principal stresses, the same stress path from the test can be plotted. Fig 5-16 shows the measured and evaluated stress path together with the measured relation between the void ratio e and the radial and axial stress.

It is interesting to compare the measurements and the calculations. Although there are some differences in absolute values, the form of the p-q diagrams and the e-σ diagrams is very similar. The stress path goes up to the yield surface and approaches the failure line at unloading. At reloading the principal stresses change sign and the stress path goes up to the failure line and follows it. The measured stress path apparently goes outside the failure line but this is probably an effect of uneven stress distribution in the sample due to friction between the sample and the walls.

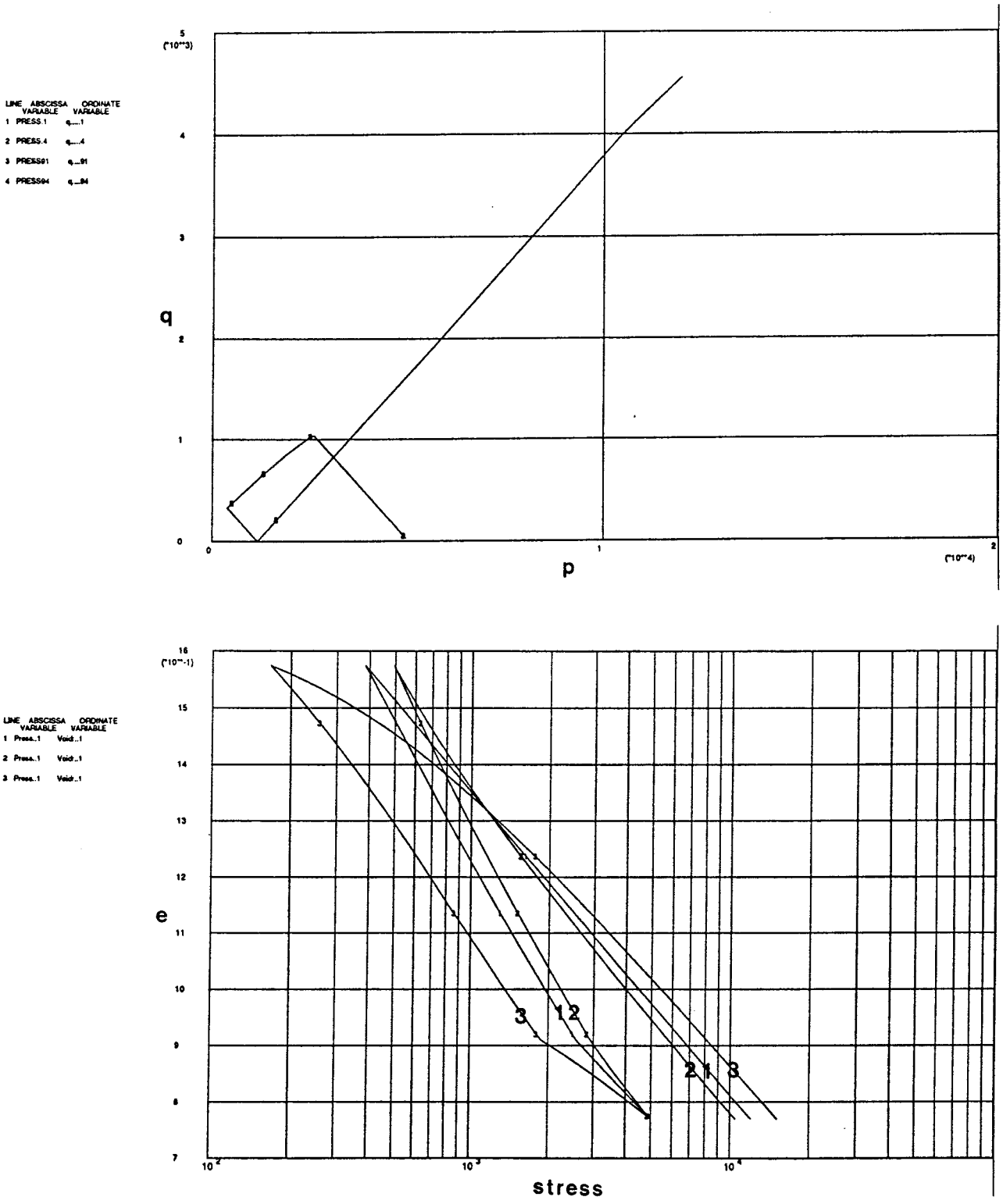

Figure 5-15: The calculated oedometer test

Upper: Mises stress (kPa) - Average stress (kPa)

Lower: Void ratio - Average stress (curve 1)

- Radial stress (curve 2)

- Axial stress (curve 3)

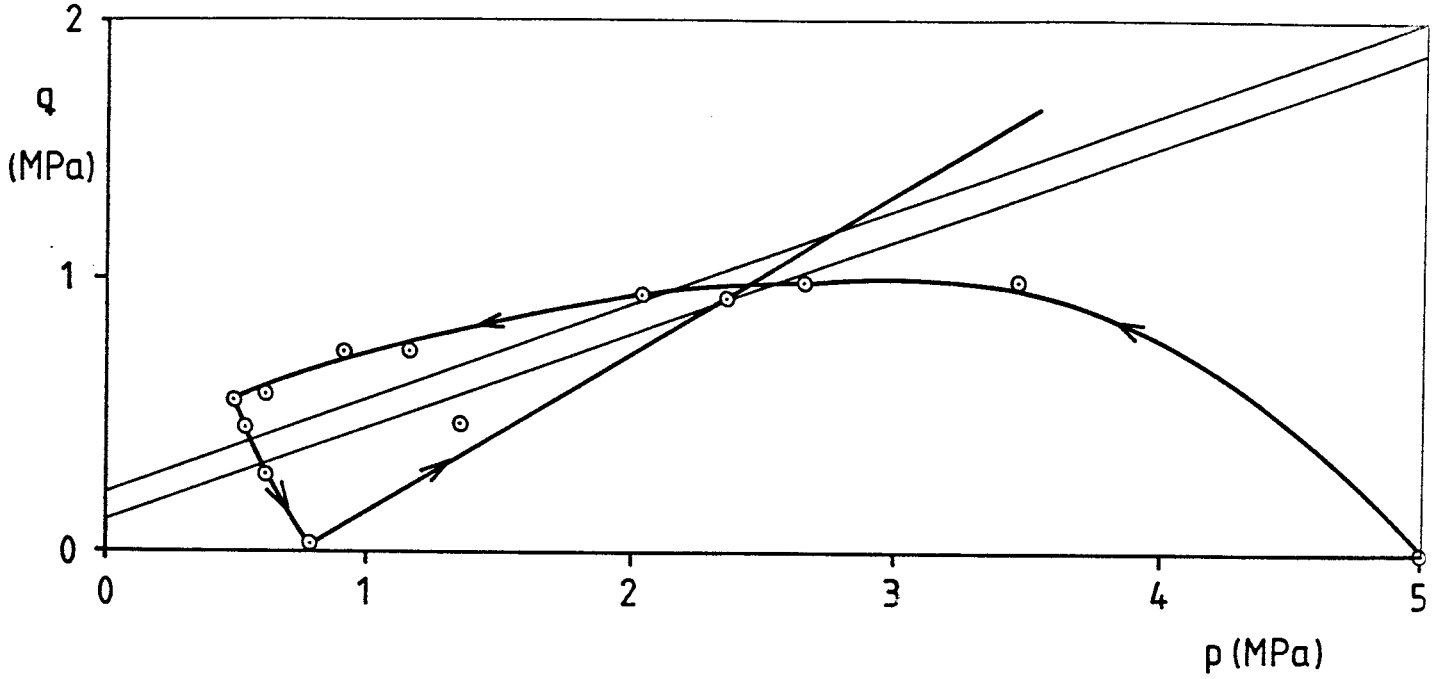

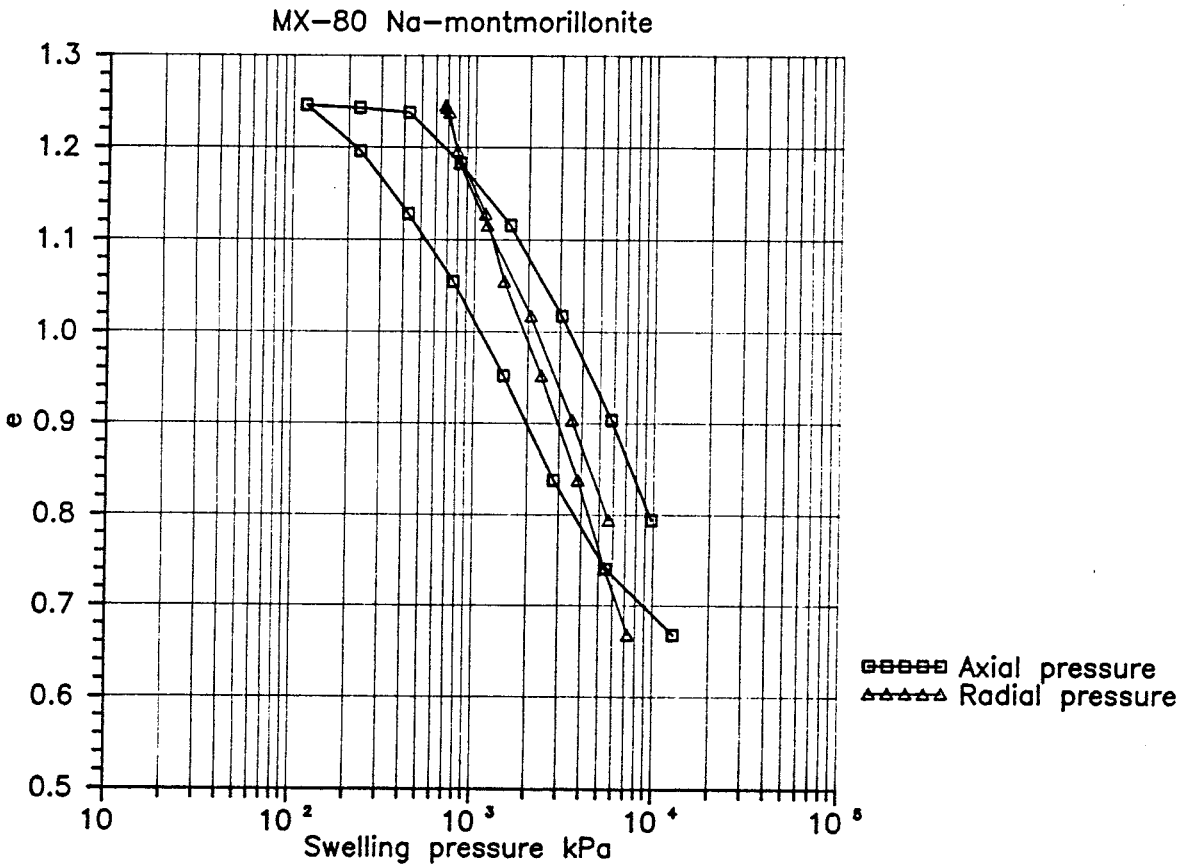

Figure 5-16: Results from the real oedometer test.
Upper: Measured stress path
Lower: Measured relation between the void ratio and the axial and radial pressure

The e-σ relations also agree very well. The drop in axial stress is significant at high void ratios and there is considerable hysteresis in axial stress but the hysteresis is quite small in radial stress.

5.2.2 The time process at one load step

The first step of unloading from 5 MPa to 3 MPa is calculated using the same element mesh and the same material model. Friction elements were used between the filter stone and the sample and between the oedometer ring and the sample. The following friction angles were used:

Oedometer ring/sample: $\phi=6.0^{\circ}$
Filter stone/sample: $\phi=9.7^{\circ}$

The results are summarized in Fig 5-17 together with the measured change in height. The diagram shows the result of two calculations, one without friction and the other one with friction. The difference resulting from the influence of friction is about 15%, but the expansion is too small since the real change in load was from 5.5 MPa to 2.8 MPa. If the expansion is corrected for this difference, the calculated relation will agree quite well with the measured one.

Fig 5-18 shows the void ratio distribution in the sample after swelling. The influence of friction is obvious close to the wall. Measurement of the real void ratio in a sample after swelling in an oedometer, confirm the pattern shown in Fig 5-18. While the difference between the measured upper and middle void ratios was very small in the centre of the sample, (upper and lower left quarters in the figure) the difference was about 5% in the outer part (upper and lower right quarters).

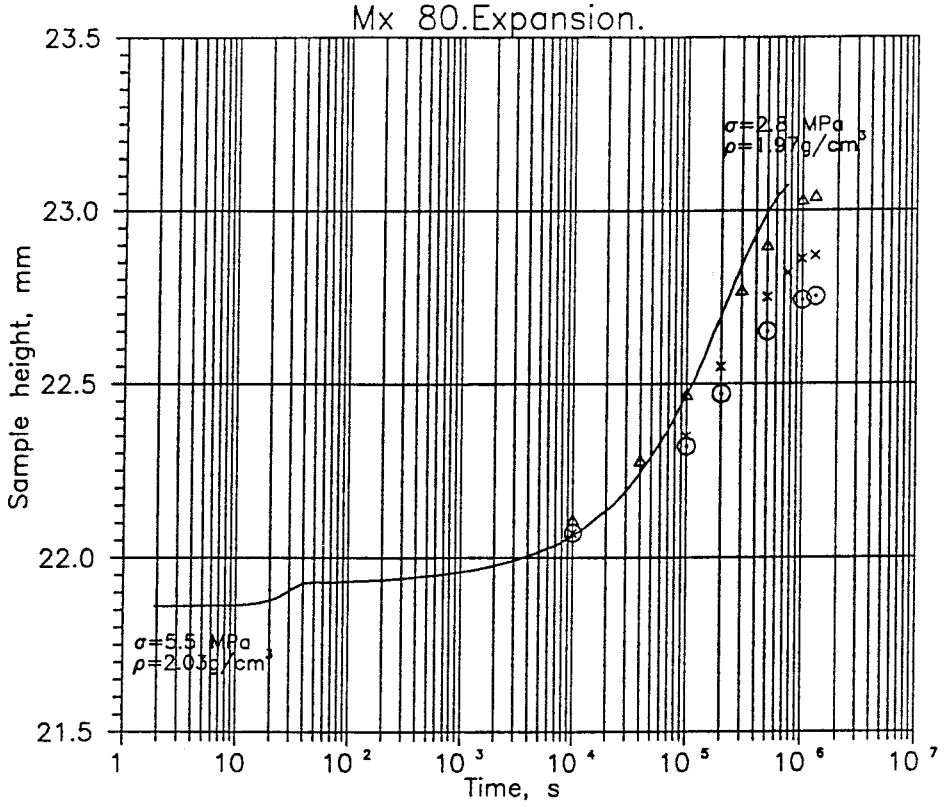

Figure 5-17: The calculated expansion as a function of time compared to the measured in the oedometer test
⊙ with friction
x without friction
Δ with friction and corrected for load

5.2.3 Conclusions

The porous elastic model and the Drucker-Prager model in combination seem to give quite reliable results when swelling and compression take place inside very stiff boundaries. However, drained triaxial test results, good enough for comparison with calculations, have not been received yet. Such tests are running at present and the results may entail some changes of the model (like the results from the undrained tests).

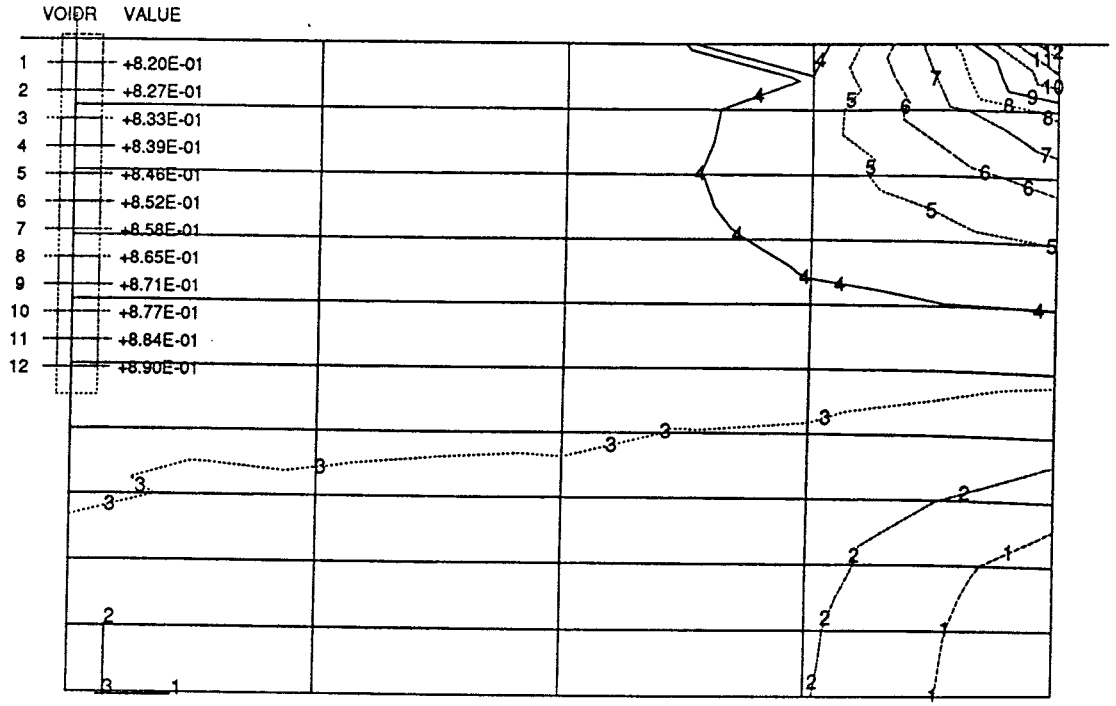

Figure 5-18: Calculated void ratio in the sample after the first step of swelling

5.3 FRICTION TESTS

The friction tests accounted for in chapter 4.2.1.5 have been simulated in order to see if the mechanism of friction works all right. The sample with 35 mm diameter and 10 mm height has been modeled with 5x5 elements with the following properties:

Plasticity:
λ=0.17
M=0.35
α=0.04
a_0=4800 kPa
K=1.0

Porous elasticity:
K=0.18
ν=0.3

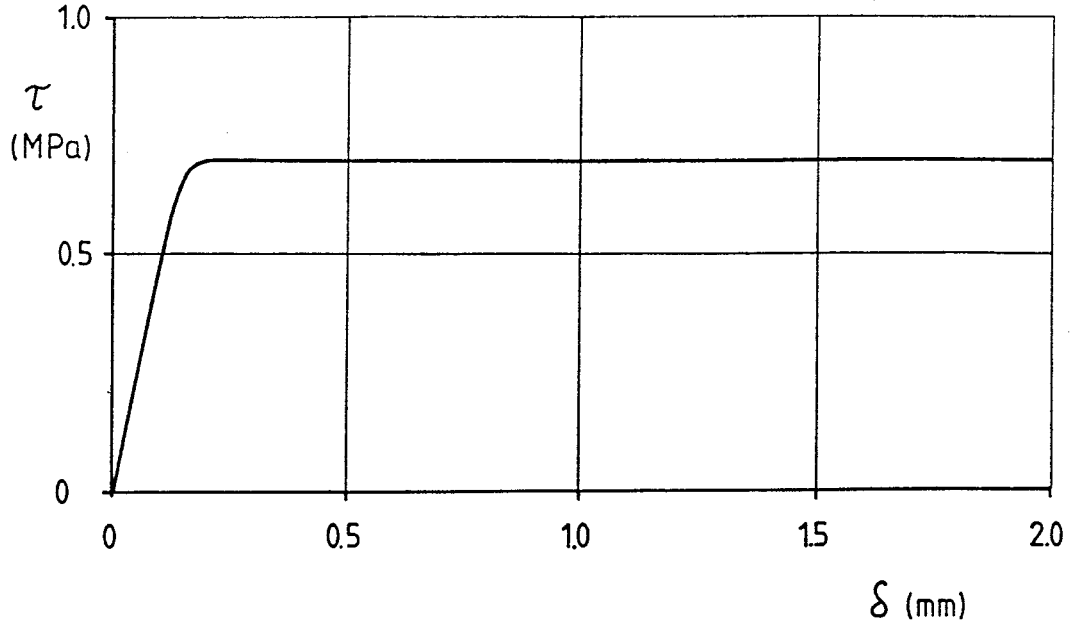

Figure 5-19: The calculated stress-strain relation in the friction tests using ϕ=8°.

Pore properties: $k=1.0\cdot10^{-13}$ m/s
$\rho_w=1.0$ t/m^3
$B_w=2.1\cdot10^6$ kPa

Initial conditions: $e_0=0.72$
$p_0=5000$ kPa

Friction: $\phi=8^\circ$
$G_s=1.0\cdot10^8$ kPa

The friction elements are located at the bottom of the sample and the surface moves with a constant rate of strain of 1 mm/h.

Fig 5-19 shows the stress-deformation relation. The shear stress is the average stress calculated as in the real test, i.e. based on the total shear force. Failure occurs at τ=0.7 MPa, which corresponds to the given friction angle 8° in the friction element. The deformation is 0.2 mm at failure, which is about half the measured deformation.

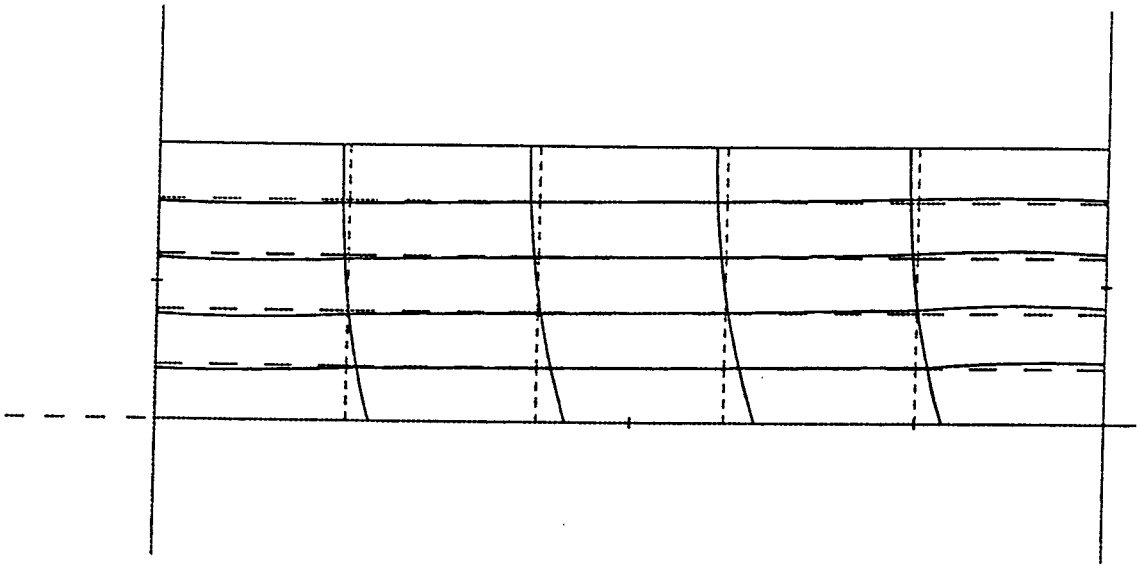

Figure 5-20: The deformed sample in the friction calculation. The displacements are enlarged 10 times

Fig 5-20 shows the deformed sample after 1 hour and 5 minutes. The strains in this figure are enlarged by 10 times. As can be seen in the figure, the sliding makes the sample deform and it is the sample deformations that control the appearance of the stress-deformation curve in Fig 5-19.

It is interesting to study the stress and pore pressure distribution in the sample as well. Fig 5-21 shows the Mises' stresses and the pore pressure after 1 hour and 5 minutes of shear (corresponding to 1.1 mm deformation). As expected, the Mises' stresses are very heterogeneously distributed, giving stresses that are high but not yielding failure close to the surface. The pore pressure is symmetric with negative values in the front of the moving sample and up to 2 MPa (positive) in the back part.

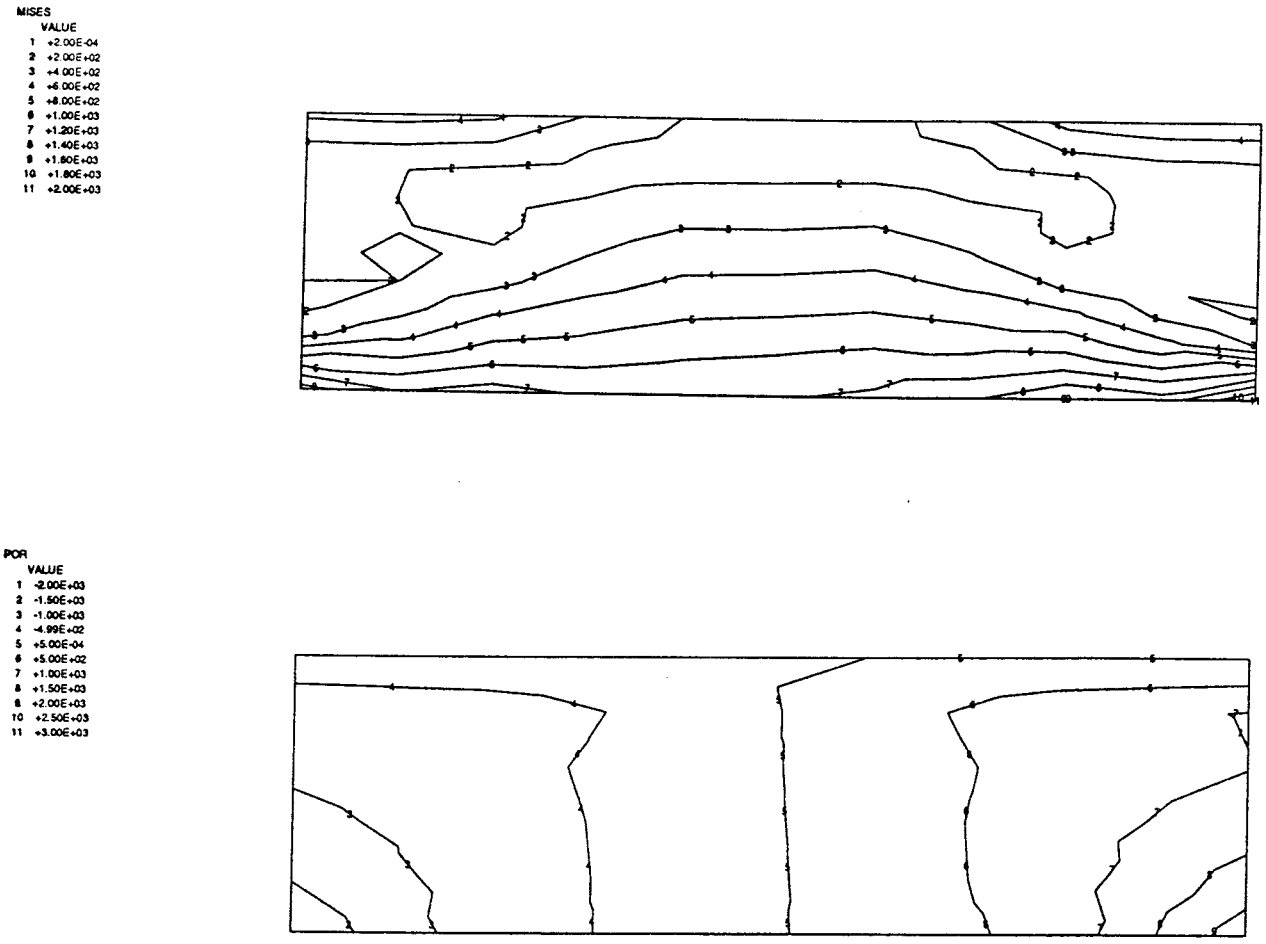

Figure 5-21: Contour plots after 1.05 mm shear in the friction tests.
Upper: Mises stresses (kPa)
Lower: Pore pressure (kPa)

Conclusions

The mechanism of sliding between a clay and some adjacent surface, seems to work when using the friction model. However the total deformation before slip seems to be too small. Whether this is due to the properties of the clay or to the properties of the friction element is not quite clear. However, the calculated behavior can be made to agree better with the measured one if the "stiffness in sticks" G_s is decreased.

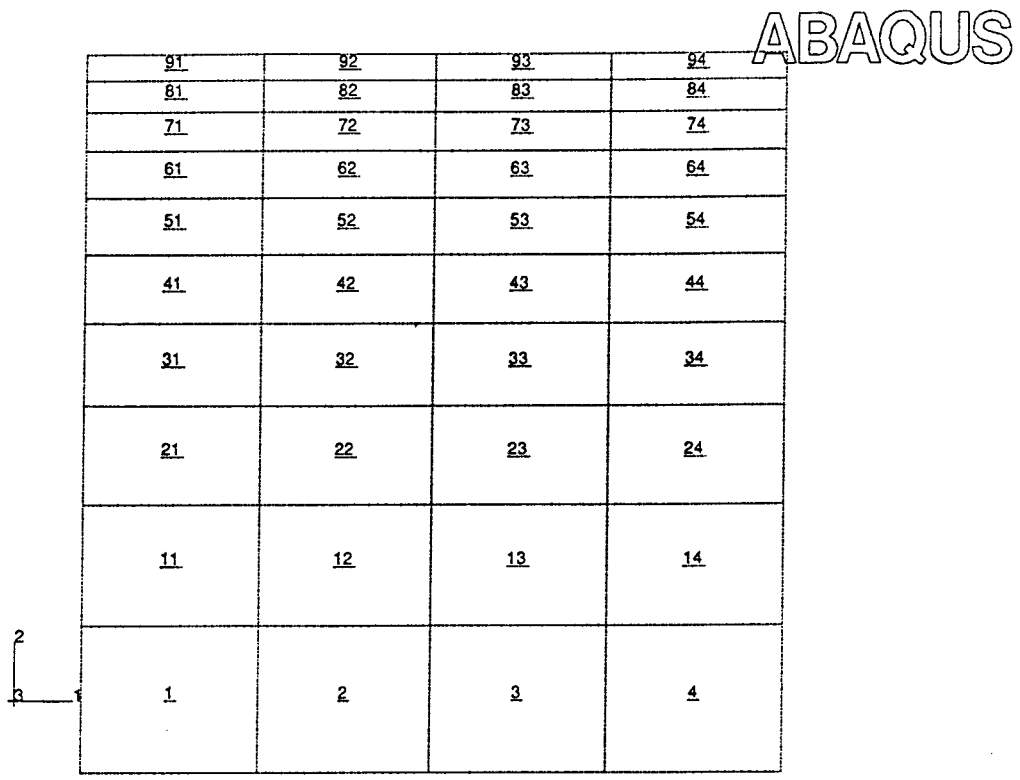

Figure 5-22: Element mesh in the thermomechanical calculation. Only the upper right quarter of the sample is modeled.

5.4 THERMOMECHANICAL TESTS

The thermomechanical tests described in chapter 4.2.1.4 have been modeled and calculated. Fig 5-22 shows the element mesh used in the calculations. Only the upper quarter of the sample is modeled. The left boundary is a symmetry axis and the bottom boundary is a symmetry plane. The upper boundary is drained and the right boundary is locked. The sample is completely confined meaning that no expansion is allowed for.

The Drucker-Prager model is used for the calculations shown here. Very little difference was obtained when the Critical State model was used. The indata are:

Plasticity:	$\beta=20^{\circ}$
	$d=100$ kPa
	$\psi=20^{\circ}$
	$K=1.0$
Yield function:	See Table 4-1 chapter 4.2.3
Porous elasticity:	$K=0.21$
	$\nu=0.4$
Pore properties:	$k=1.0\cdot10^{-12}$ m/s
	$\rho_w=1.0$ t/m^3
	$B_w=2.1\cdot10^{6}$ kPa
Initial conditions:	$e_0=1.22$
	$p_0=750$ kPa

The heat is increased $\Delta T=70^{\circ}$ over a period of 2000 seconds which corresponds to what was actually measured during the real tests.

The development of the pore pressure u and the average stress q is shown in Fig 5-23. The increase in pore pressure is very high and the dissipation is quite fast. The u-t relation agrees very well with what was measured during the real tests (shown in Figs 4-15 to 4-17). The calculation corresponds to test TP41 in Fig 4-15 from which it is clear that the calculated pressure increase is higher than the measured one. The reason for this is mainly the degree of saturation which was only $S_r=96.9\%$ for the sample in the test in Fig 4-15 while it was 99.1% and 98.4% in the other two tests. The back pressure 100 kPa was not enough to ensure saturation while the other two samples were probably saturated. (See chapter 2.6.3) Another reason is the expansion of the oedometer that takes place in the real test. This expansion is not taken into account in the calculation.

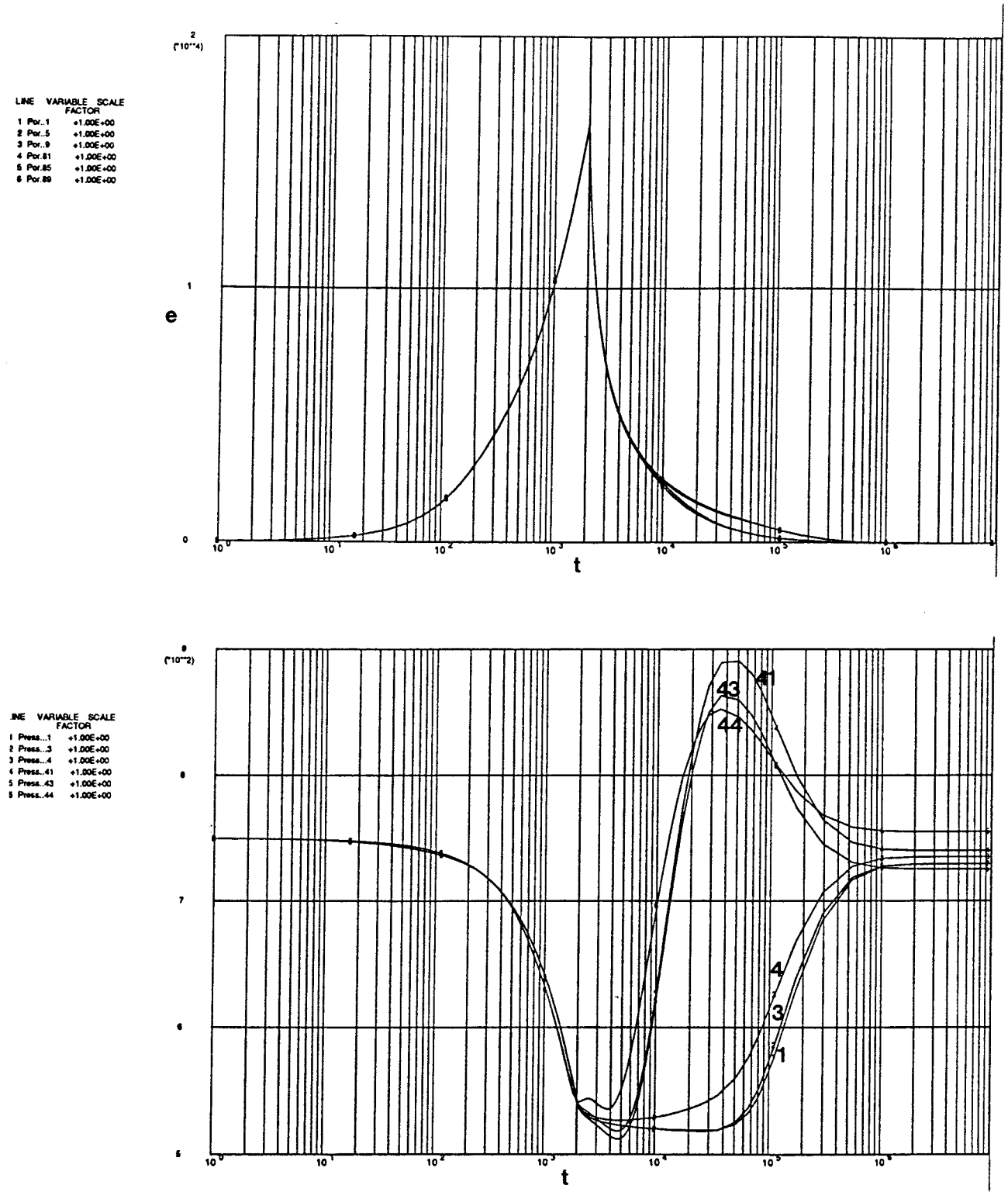

Figure 5-23: Results from the thermomechanical calculation.
Upper: Pore pressure in the nodes (kPa) - time (s)
Lower: Average stress in some elements (kPa) - time (s)

Fig 5-24 shows the stress path of the selected elements and the resulting average stress in the sample after 10^7 seconds. This figure (and Fig 5-23) shows one interesting thing! The average stress is higher in the upper part of the sample than in the lower. It is, in average, p=960 kPa at the top of the sample which can be compared to the original p=750 kPa. The reason for this is consolidation of the upper part of the sample due to the high pore pressure in the centre of the sample. This high pore pressure results in a high total pressure on the upper part and since the pore pressure is lower close to the filter stone, the effective stress will be high there. A resulting higher stress was also measured in the real tests, which confirms this conclusion.

Fig 5-25 shows the influence of the hydraulic conductivity on the results. If k=10^{-13} m/s is used, the pore pressure increase will be ≈50 MPa instead of 15 MPa. k=10^{-13} m/s would correspond to test TP31 in Fig 4-17.

Conclusions

Although the analyses are not complete, the preliminary conclusion is that the models described can be applied to thermomechanical calculations as well. A further conclusion from the calculations is that the increase in swelling pressure observed in some tests on Na-bentonite can be explained by local consolidation of the samples.

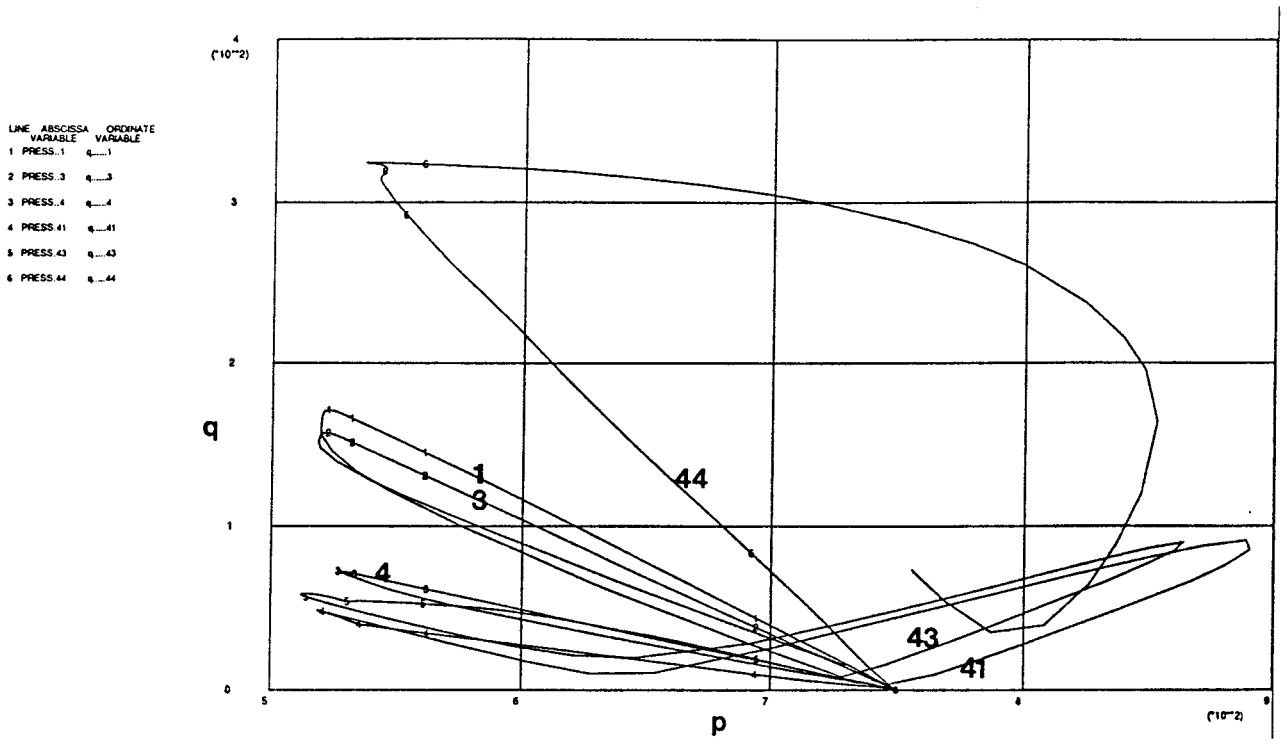

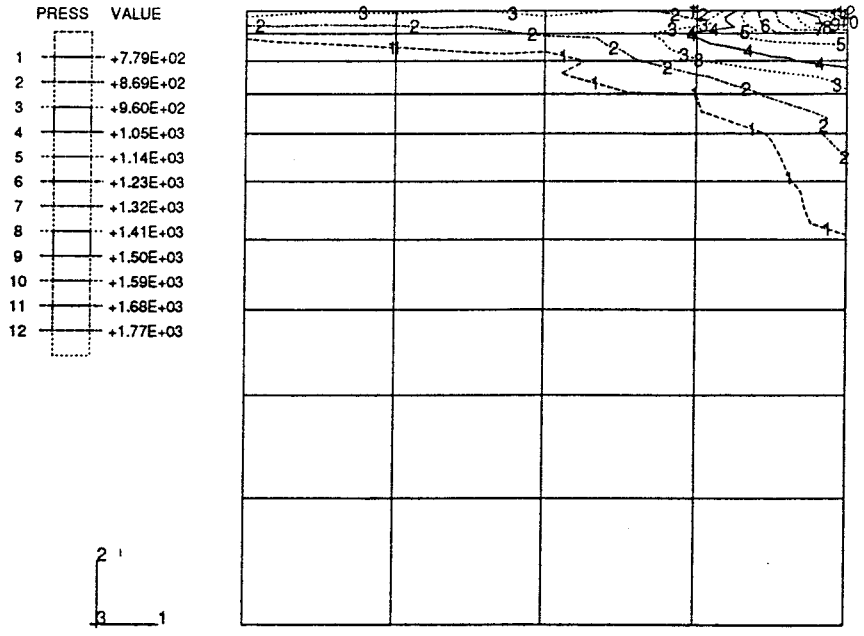

Figure 5-24: Results from the thermomechanical calculation.
Upper: Stress paths for elements 1,3,4,41,43,44 (kPa)
Lower: Contour plot of the average stress at the end of the test

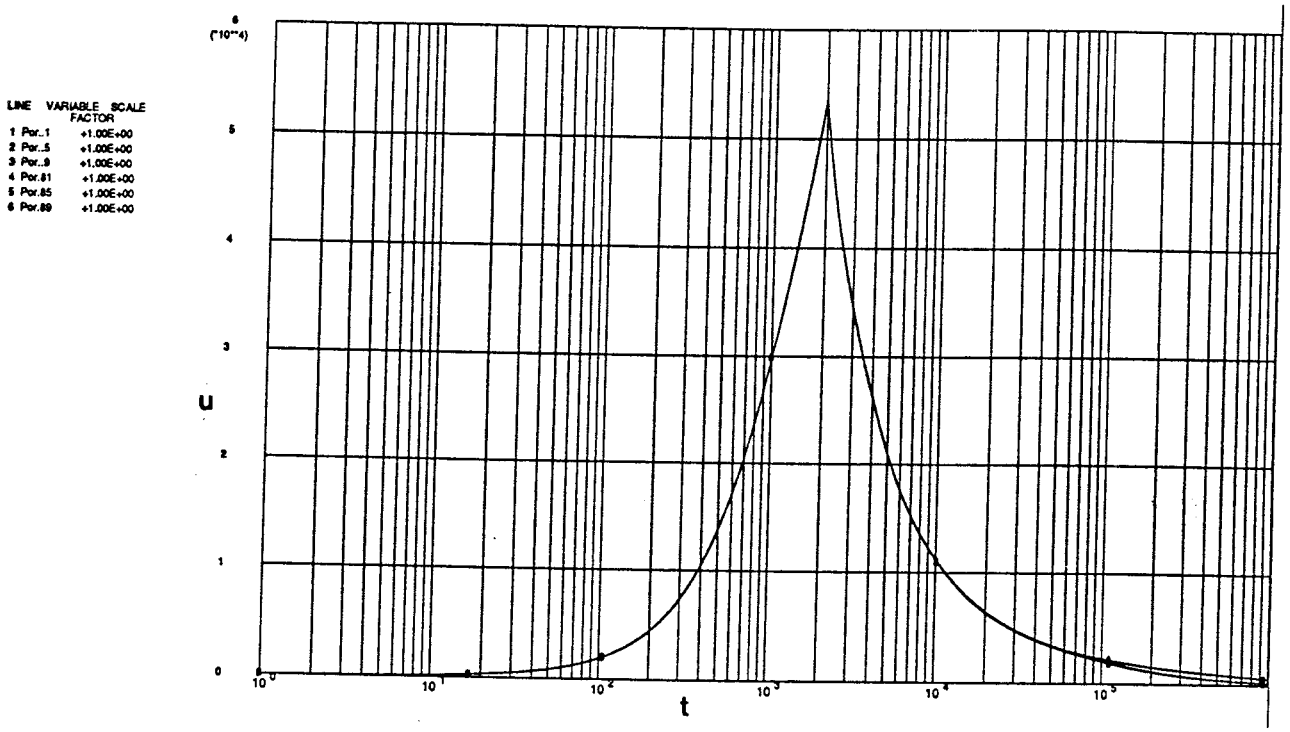

Figure 5-25: Results from the thermomechanical calculation using a lower hydraulic conductivity. The pore pressure (kPa) is shown as a function of the elapsed time (s)

6. SCENARIO CALCULATIONS

The long-range aim of the development accounted for is to develop a basis for performance and scenario calculations. In this chapter two examples of such calculations will be shown. They should be considered as examples of how such calculations can be made and not true descriptions of the performance. The effective stress models have been used, although they are not fully developed and verified at present.

6.1 BENTONITE INTRUSION

The swelling properties of bentonite makes it intrude potential cracks and openings in the rock as well as in the canister. The consequence of such intrusion is of importance for the function of the buffer material. The friction between the clay and the fractured material as well as the internal friction in the clay, prevents complete homogenization of the clay and means that some part of the clay can have a low density.

The scenario of bentonite intrusion is difficult to calculate for two reasons:

1. The density is changing from very high to very low and the material models are not sufficiently generalized to be applicable, independently of the density.

2. The sharp corners in the beginning of the opening are difficult to simulate, since the stresses and strains in the elements around a corner will be very high. Theoretically they are infinite.

3. The intrusion means that the element mesh and the elements themselves are extremely deformed. The finite element method is not suited for handling very deformed elements.

The first two difficulties can be overcome by making approximations. Some average values for the material models can be used and the geometry can be modeled, with rounded corners instad of sharp ones.

The difficulties with deformed elements can be overcome by remeshing, which means that a new element mesh is replacing the old one while the stress and strain situation is kept the same. It also means that the material properties are maintained constant applying also the stress-strain history of the old mesh.

6.1.1 Element and material models

Fig 6-1 shows the scenario of bentonite intrusion into a canister with a circumferential crack. Fig 6-1 also shows the axisymmetric element mesh and an enlargement of the mesh close to the opening. The penetration is assumed to start half a cm inside the opening in order to facilitate the calculations. The bentonite is simulated with the Porous Elasticity model and the Drucker-Prager Plasticity model with the following indata:

Plasticity:	$\beta=20^{\circ}$
	d=100 kPa
	$\psi=20^{\circ}$
	K=1.0
Yield function:	See Table 4-1 chapter 4.2.3
Porous elasticity:	K=0.21
	ν=0.4

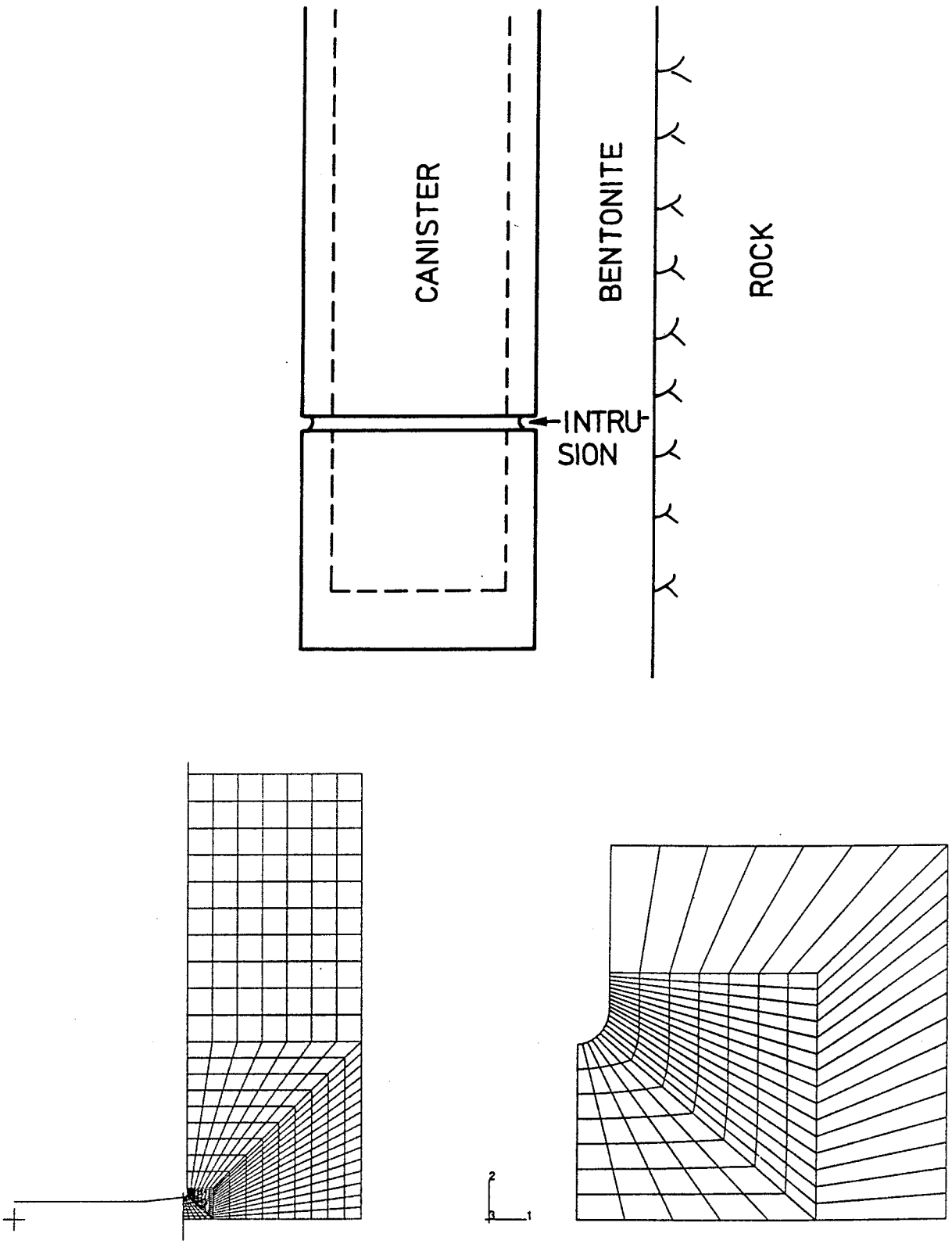

Figure 6-1: The scenario of bentonite intrusion. The complete element mesh and a close up of an area about 10x10 cm^2 are shown as well

Pore properties: $k=1.0\cdot10^{-13}$ m/s
$\rho_w=1.0$ t/m^3
$B_w=2.1\cdot10^6$ kPa

Initial conditions: $e_0=0.77$
$p_0=5000$ kPa

Friction: $\phi=6^\circ$

The contact between the clay and the canister was simulated by friction elements.

6.1.2 Calculations

The calculations have been performed in several different ways. The results of two of the calculations will be briefly presented.

Fig 6-2 shows the penetrated and deformed bentonite mesh in one of the calculations. The total penetration was about 8 cm when the calculation stopped. The mesh and many of the elements are strongly deformed and some problems with the upper front elements have appeared.

In the other calculation the remeshing technique was applied and a new element mesh was created on three occasions. The calculation was stopped after about 12 cm intrusion. Fig 6-3 shows the deformed element mesh after the last calculation while Fig 6-4 shows the deformed element mesh and the void ratio distribution at different times.

An increase in void ratio with increased penetration can be seen. A special phenomenon can be observed in the corner with strongly increased void ratio. This phenomenon is caused by the very strong dilatancy in the material model. Since the dilatancy is smaller in

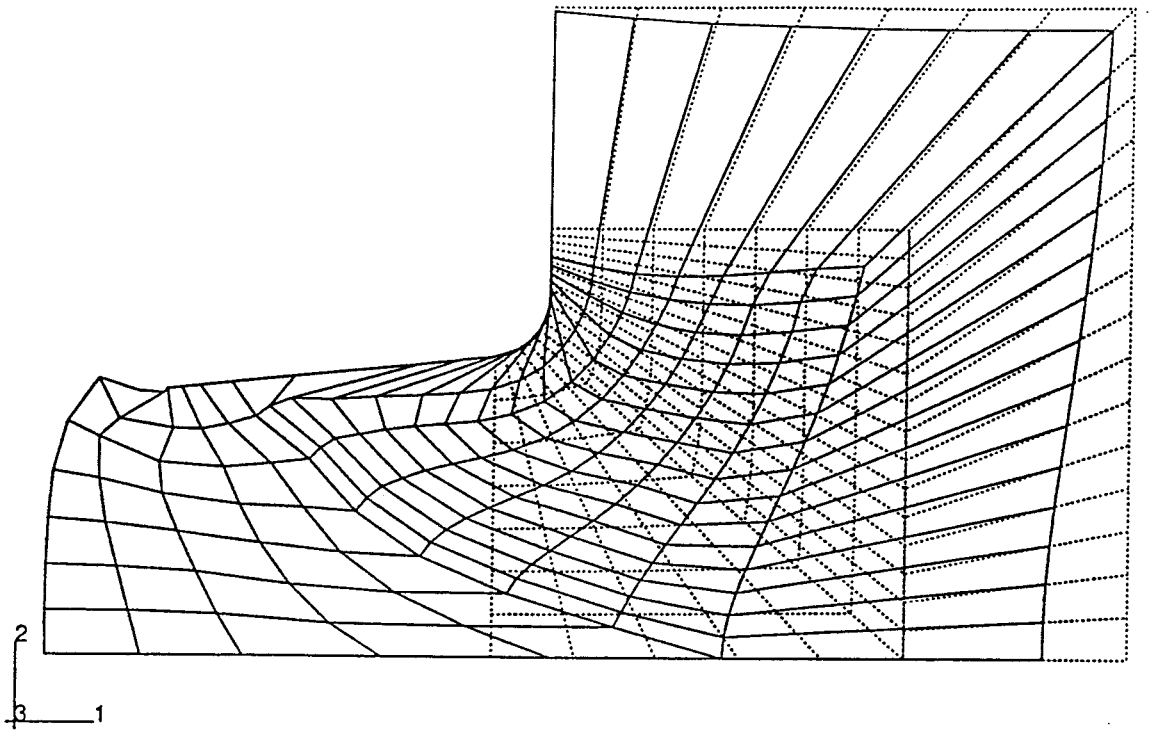

Figure 6-2: The deformed element mesh in the first calculation. The bentonite intrusion is about 8 cm

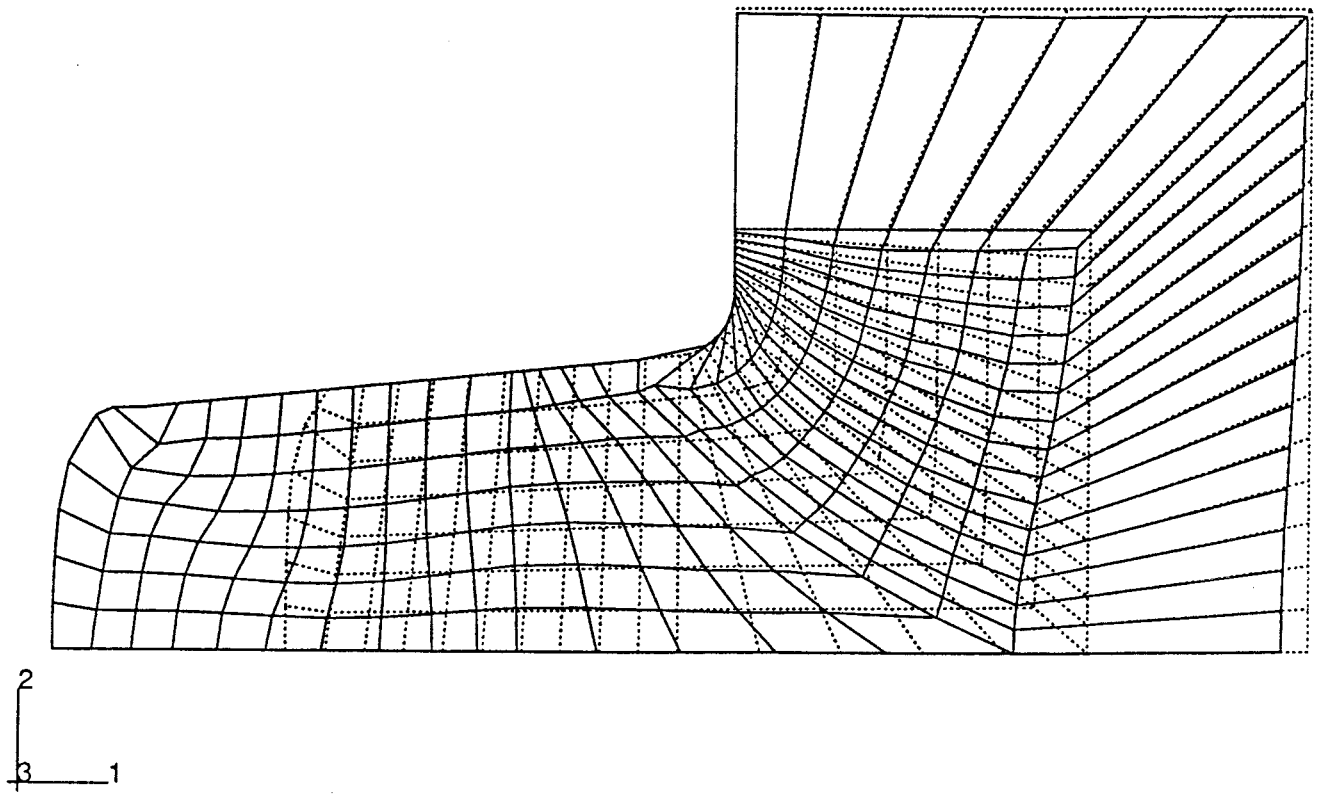

Figure 6-3: The deformed element mesh in the remeshing calculation. The bentonite intrusion is about 12 cm.

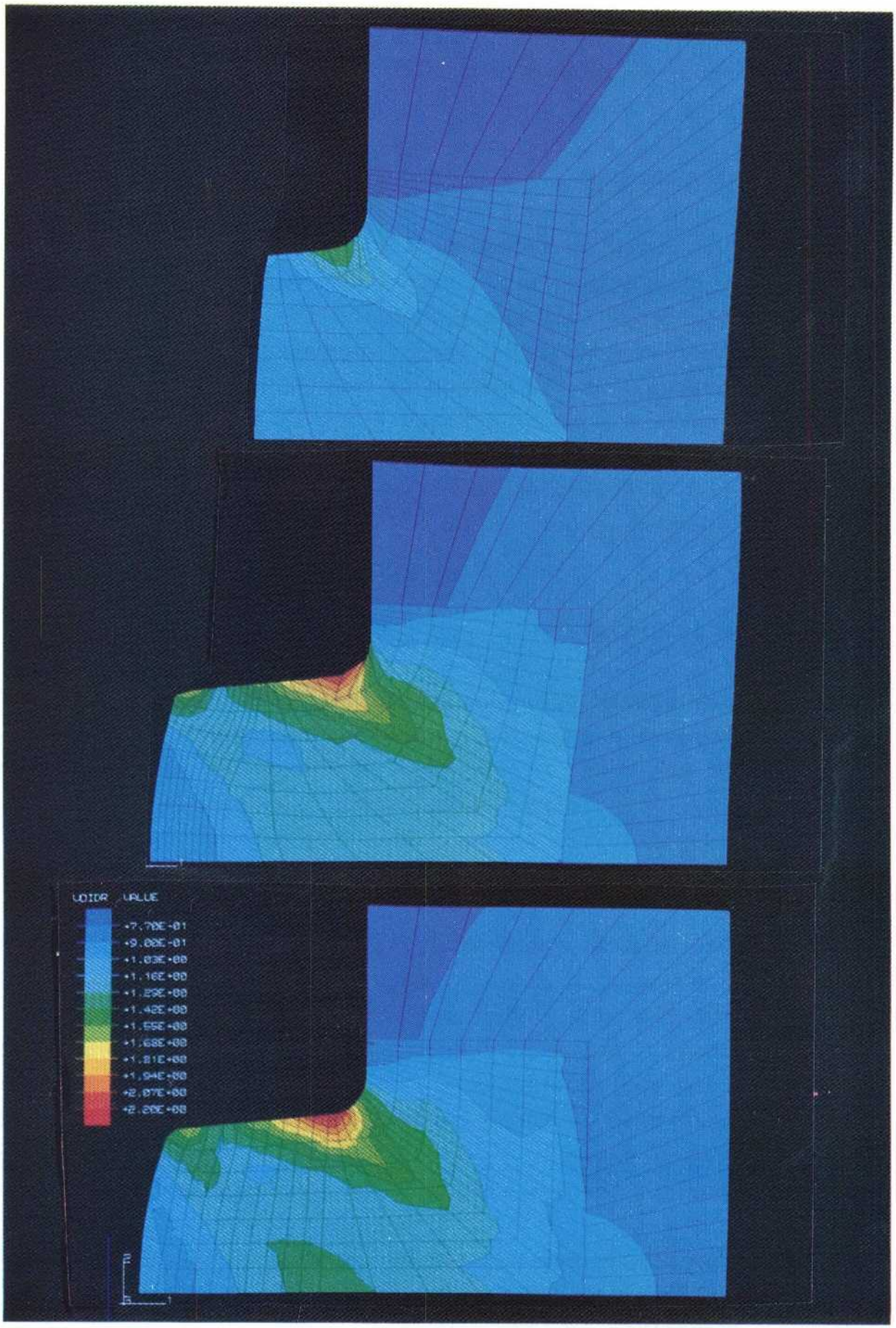

Figure 6-4: Contour plots of the void ratio in the second calc.

the real material, the calculation example does not show the real behavior at bentonite intrusion.

6.1.3 Conclusions

The examples of bentonite intrusion illustrates the difficulties in performing the calculations. They also show that the problems with large deformations can be overcome by proper geometry design and remeshing. The technique of remeshing is possible to handle although it means a lot of work and difficulties. The calculations also confirm the conclusion that the ψ-value in the D-P model needs to be modified to a lower value.

6.2 ROCK SHEAR

The effect of a shear deformation along a fracture through a deposition hole has been calculated by use of the total stress model and verified in model tests [1],[3]. Similar calculations have been made using the effective stress model. Two examples of these calculations will be shown in this chapter.

The general geometry and the element mesh after shear are shown in Fig 6.5. Only the upper quarter was modeled with a vertical symmetry plane and a horizontal anti-symmetry plane. The model was approximately scaled 1:10 of a real deposition hole. The clay thickness in these calculations was 6 cm and the solid copper canister 8 cm in diameter. A detailed description of the geometry etc. is given in [3].

The copper was modeled by an "Elastic" and a "Metal Plasticity" model, with the stress strain relations described in [3].

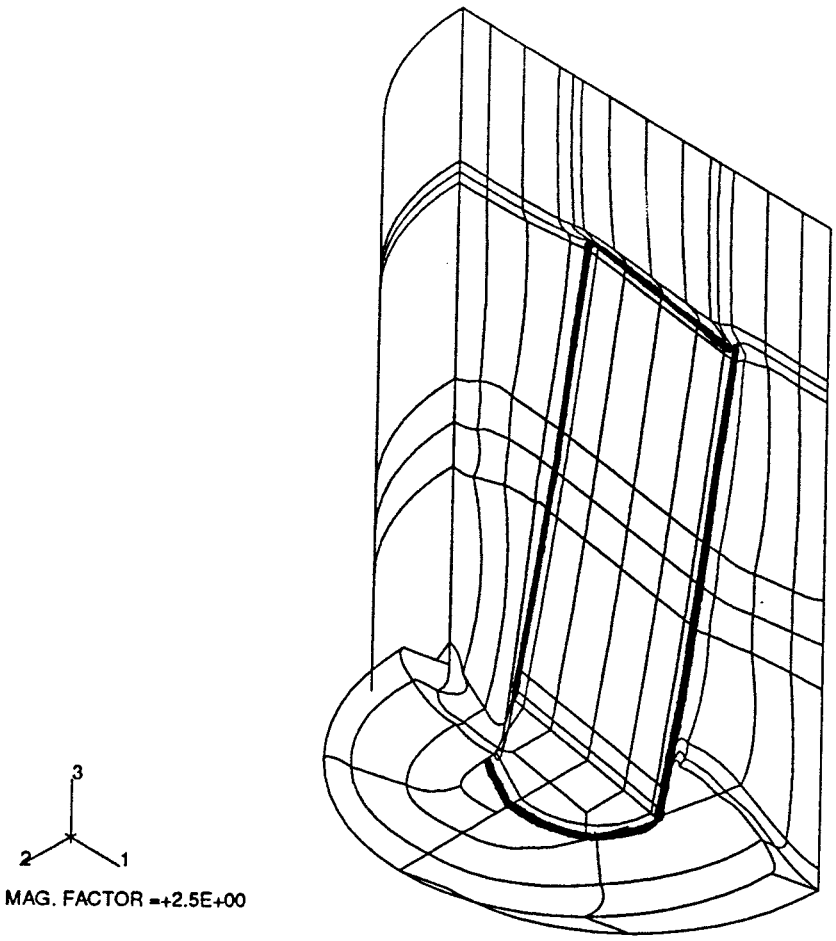

Figure 6-5: The geometry and element mesh after shear

The bentonite was modeled by "Porous Elasticity" and "Critical State Plasticity" models. The indata were:

Plasticity:	λ=0.10
	M=0.36
	α=0.04
	a_0=4327 kPa
	K=1.0
Porous elasticity:	K=0.091
	ν=0.2
Pore properties:	k=2.0·10^{-14} m/s
	ρ_w=1.0 t/m^3
	B_w=2.1·10^6 kPa

Initial conditions: e_0=0.54
p_0=4500 kPa

The clay was thus modeled with high stiffness, low void ratio, and low permeability in relation to the swelling pressure. The bentonite/rock and bentonite/-copper interface was assumed to be friction-free.

6.2.1 Undrained analysis

In the undrained analysis the rock was assumed to be non-permeable. A similar analysis with a completely drained rock was also performed but the difference in results was small.

The rate of shear was quite slow, i.e. 1 mm per year. The total displacement was 10 mm and the total time thus 10 years.

Fig 6-6 shows contour plots of the pore pressure and the void ratio at the end of the shear. The pictures show that in spite of the slow shearing, the pore pressure is far from evened out with a highest value of about 5 MPa. Accordingly, the resulting void ratio is changed very little. Thus, in spite of the slow shearing, the pore pressure differences in the clay are very large, due to the low hydraulic conductivity.

Fig 6-7 shows the Mises stresses in the canister and in the clay. The highest stresses are about 55 MPa in the periphery halfway between the centre and the end of the canister, while the stresses in the centre of the canister are quite low. In the clay the stresses are generally close to the ones of failure at undrained shear.

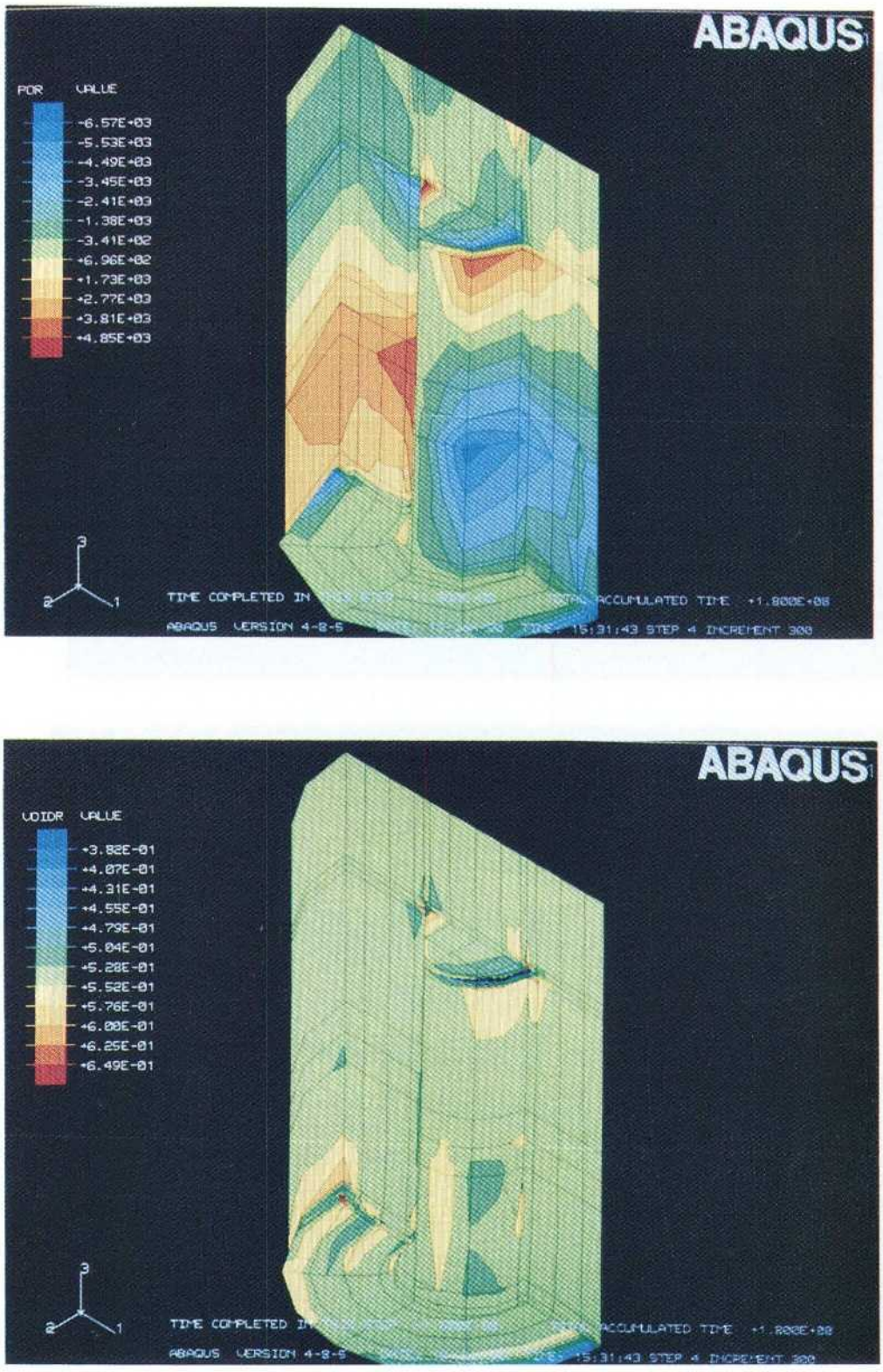

Figure 6-6: Contour plots from the rock shear calculation assuming undrained conditions.
Upper: Pore pressure in the clay (kPa)
Lower: Void ratio in the clay

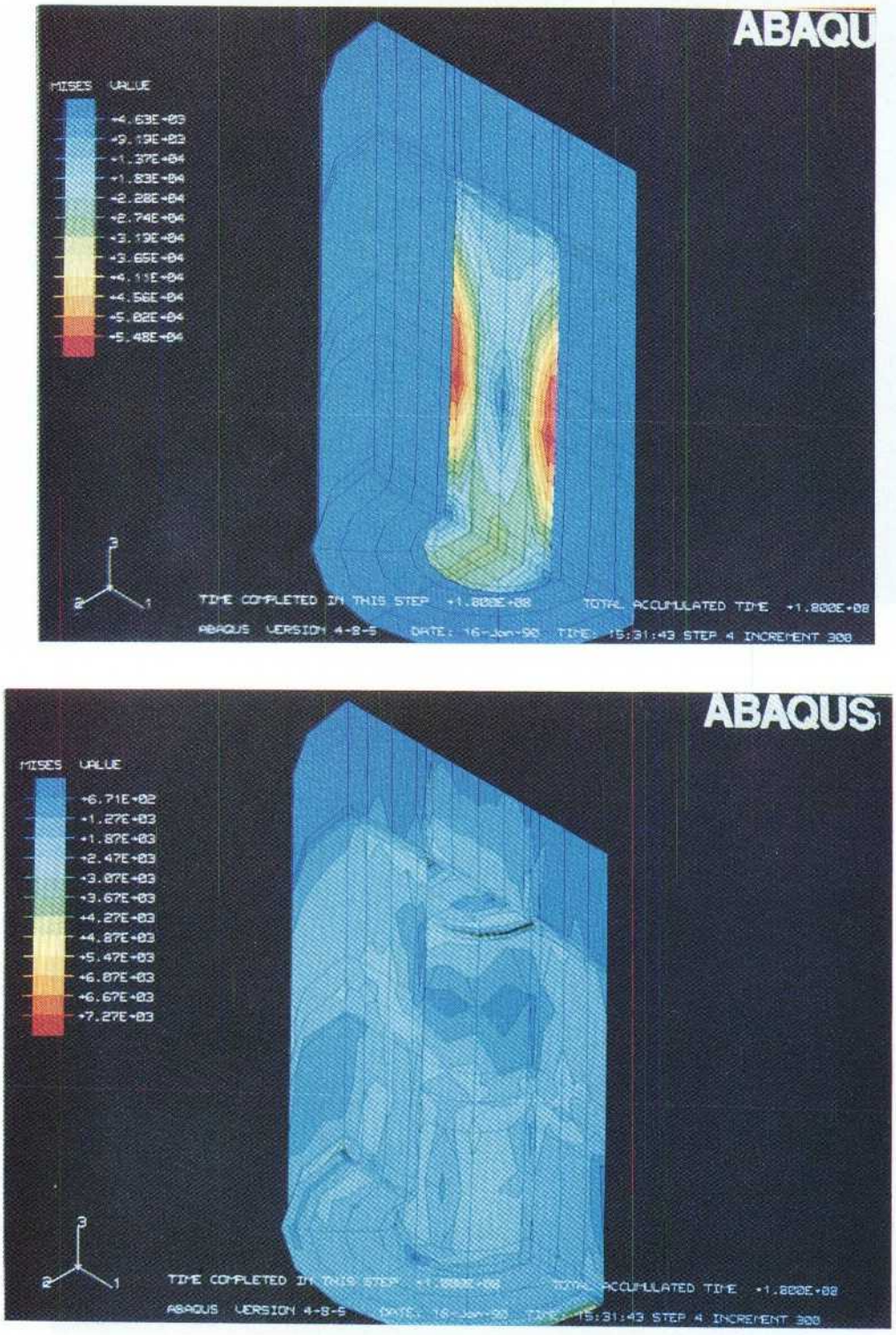

Figure 6-7: Contour plots from the rock shear calculation assuming undrained conditions.
Upper: Mises stresses in the canister (kPa)
Lower: Mises stresses in the clay

6.2.2 Drained analyses

The drained analysis was made without pore pressure, which means that it corresponds to such a slow deformation that no pore pressure will arise.

Fig 6-8 shows some results of this analysis. The Mises stresses in the canister are similar to those obtained in the undrained analysis with one important exception, i.e. that the stresses are up to 100 Mpa in the centre of the canister which can be compared to 25 MPa in the undrained analysis. The reason for this difference is explained by considering the stresses in the clay. The drained condition causes consolidation and swelling of the clay resulting in large differences in average stress as well as in Mises stresses. The picture shows that the average stress is up to 10 MPa and the Mises stresses up to 5 Mpa in the center of clay specimen according to the model, and this can be compared to Mises stresses of only a few MPa in the undrained analyses. This difference is thus causing higher stresses in the canister.

6.2.3 Conclusions

Although the indata and the material models of the rock shear analyses are not completely relevant some conclusions can be drawn:

1. The analyses can be made by use of the effective stress models.

2. Even the slow rate of shear of 1 mm per year produces high pore pressures, meaning that undrained conditions prevail.

3. The drained situation is more detrimental to the canister than the undrained one.

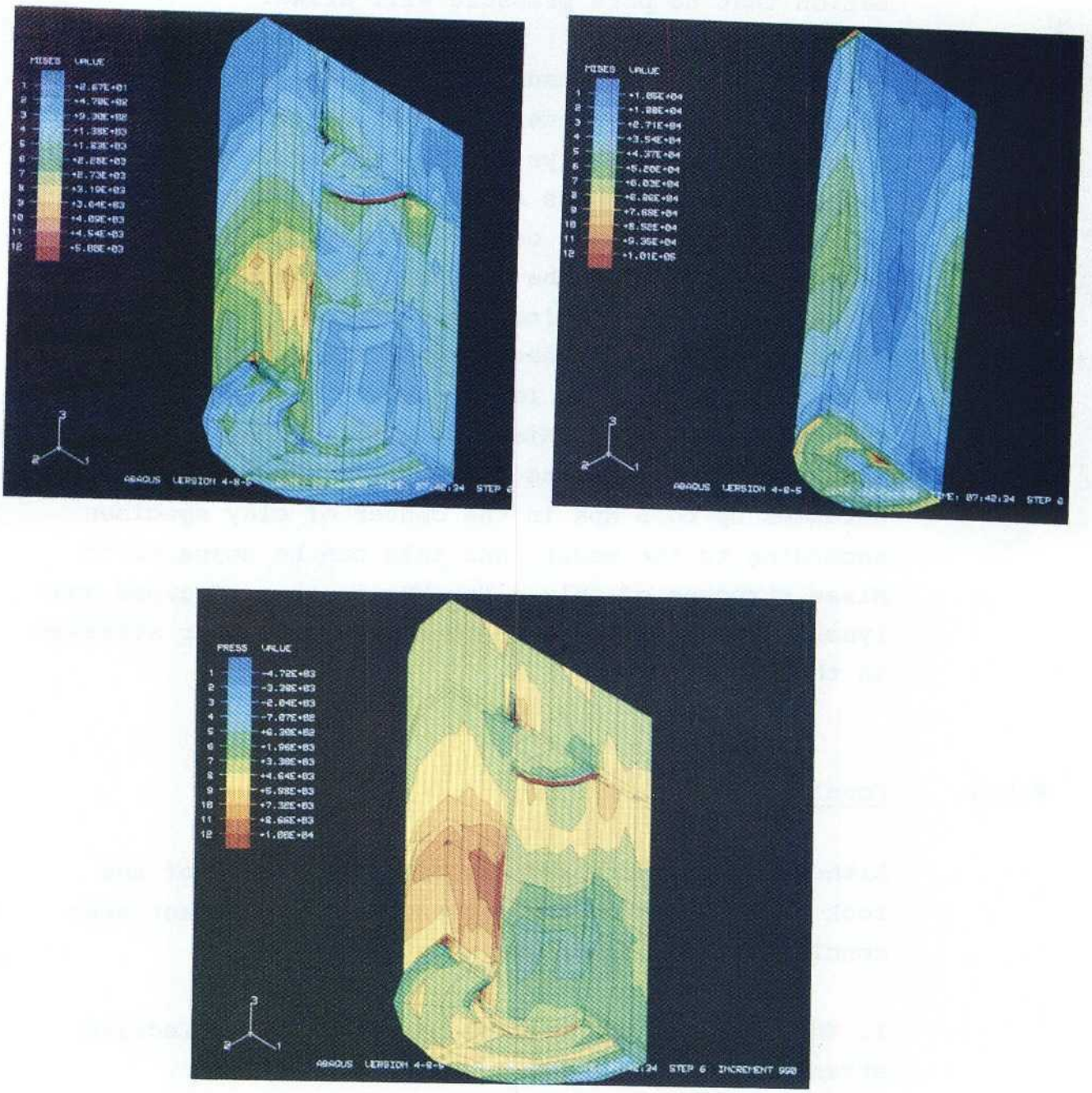

Figure 6-8: Contour plots from the rock shear calculation assuming completely drained conditions
Upper: Mises stresses in the clay and canister (kPa)
Lower: Average stress in the clay (kPa)

7. CONCLUSIONS

This report is a summary of what has been achieved in the continuous work of modeling the geotechnical behavior of the buffer material. Some conclusions, that are of importance for the continuation, are listed below:

1. No results speak against the applicability of the effective stress theory. The bentonite-based buffer materials seem, in all respects, to behave according to the theory. Thus, all calculations that include pore pressure and void ratio, are performed with the assumption that the theory is valid without restrictions.

2. A total stress material model that agrees with the metal elasticity-plasticity model can be applied to the buffer materials at quick undrained events.

3. Two effective stress plasticity models have been applied and tested: a modified Critical State model and the extended Drucker-Prager model.

- None of these two models agrees with the real behavior of the buffer materials in all respects.
- D-P seems to apply better under drained conditions.
- CS seems to apply better under undrained conditions.
- Further testing is required in order to define some of the parameters better.
- Both models would be considerably improved if the shape of the yield surface could be changed

4. The elastic recoverable part of the behavior seems to be well described by the Porous Elasticity model.

5. The thermomechanical behavior seems to be well modeled by assigning to the pore phase and the solid phase relevant properties.

6. Friction between the clay and an adjacent material can be well modeled.

7. The finite element program ABAQUS can well handle these complicated material models and in principle, all types of scenarios can be treated. However, the plasticity models (especially CS) may require much effort and long computer time to handle, especially at large strain.

8. At large swelling, a technique for remeshing has been proven to function, allowing for all types of large strain.

9. The technique used for simulating rock shear is applicable using effective stresses, and the interaction between canister and clay can be well modeled. Preliminary calculations show that drained long time shear might be more dangerous to the canister than undrained quick shear.

10. The material models and calculation techniques are applicable to other smectite-rich buffer materials as well.

11. Data is available for modeling Ca-bentonite but not the behavior of mixtures.

12. Temperatures below 90°C seem to have little effect on the material models. Still, some additional tests are required to settle the matter.

13. The influence of pore water chemistry (esp. salt content) cannot yet be modeled.

REFERENCES

1. Börgesson L. (1986) - Model shear tests of canisters with smectite clay envelopes in deposition holes. SKB Technical Report 86-26.
2. Börgesson L. and Pusch R. (1987) - Rheological properties of a calcium smectite. SKB Technical Report 87-31.
3. Börgesson L. (1988) - Modelling of buffer material behavior. Some examples of material models and performance calculations. SKB Technical Report 88-29.
4. Börgesson L., Hökmark H. and Karnland O. (1988) - Rheological properties of sodium smectite clay. SKB Technical Report 86-26.
5. Börgesson L. (1989) - Shear of a clay-embedded waste canister. Proc. 12th ICSMFE, Rio de Janeiro.
6. Chen W. F. and Mizuno E. (1990) - Nonlinear analysis in soil mechanics. Theory and implementation. Developments in geotechnical engineering vol. 53. Elsevier.
7. Graham J., Saadat F., Gray M. N., Dixon D. A. and Zhang Q.-Y. - (1989) Strength and volume change behavior of sand-bentonite mixture. Can. Geotech. J. 26, 292-305.
8. Hibbit, Karlsson and Sorensen. ABAQUS manuals.
9. Lambe T. W. and Whitman R. V. (1969) - Soil mechanics. John Wiley and Sons Inc., New York.
10. Mitchell J. K. (1976) Fundamentals of soil behaviour. John Wiley and Sons Inc., New York.
11. Schofield A. and Wroth P. (1968) - Critical state soil mechanics. Mc Graw-Hill, London.

List of SKB reports

Annual Reports

1977-78
TR 121
KBS Technical Reports 1 – 120
Summaries
Stockholm, May 1979

1979
TR 79-28
The KBS Annual Report 1979
KBS Technical Reports 79-01 – 79-27
Summaries
Stockholm, March 1980

1980
TR 80-26
The KBS Annual Report 1980
KBS Technical Reports 80-01 – 80-25
Summaries
Stockholm, March 1981

1981
TR 81-17
The KBS Annual Report 1981
KBS Technical Reports 81-01 – 81-16
Summaries
Stockholm, April 1982

1982
TR 82-28
The KBS Annual Report 1982
KBS Technical Reports 82-01 – 82-27
Summaries
Stockholm, July 1983

1983
TR 83-77
The KBS Annual Report 1983
KBS Technical Reports 83-01 – 83-76
Summaries
Stockholm, June 1984

1984
TR 85-01
Annual Research and Development Report 1984
Including Summaries of Technical Reports Issued during 1984. (Technical Reports 84-01 – 84-19)
Stockholm, June 1985

1985
TR 85-20
Annual Research and Development Report 1985
Including Summaries of Technical Reports Issued during 1985. (Technical Reports 85-01 – 85-19)
Stockholm, May 1986

1986
TR 86-31
SKB Annual Report 1986
Including Summaries of Technical Reports Issued during 1986
Stockholm, May 1987

1987
TR 87-33
SKB Annual Report 1987
Including Summaries of Technical Reports Issued during 1987
Stockholm, May 1988

1988
TR 88-32
SKB Annual Report 1988
Including Summaries of Technical Reports Issued during 1988
Stockholm, May 1989

1989
TR 89-40
SKB Annual Report 1989
Including Summaries of Technical Reports Issued during 1989
Stockholm, May 1990

Technical Reports

List of SKB Technical Reports 1990

TR 90-01
FARF31 –
A far field radionuclide migration code for use with the PROPER package
Sven Norman[1], Nils Kjellbert[2]
[1]Starprog AB
[2]SKB AB
January 1990

TR 90-02
Source terms, isolation and radiological consequences of carbon-14 waste in the Swedish SFR repository
Rolf Hesböl, Ignasi Puigdomenech, Sverker Evans
Studsvik Nuclear
January 1990

TR 90-03
Uncertainties in repository performance from spatial variability of hydraulic conductivities –
Statistical estimation and stochastic simulation using PROPER
Lars Lovius[1], Sven Norman[1], Nils Kjellbert[2]
[1]Starprog AB
[2]SKB AB
February 1990

TR 90-04
Examination of the surface deposit on an irradiated PWR fuel specimen subjected to corrosion in deionized water
R. S. Forsyth, U-B. Eklund, O. Mattsson, D. Schrire
Studsvik Nuclear
March 1990

TR 90-05
Potential effects of bacteria on radionuclide transport from a Swedish high level nuclear waste repository
Karsten Pedersen
University of Gothenburg, Department of General and Marine Microbiology, Gothenburg
January 1990

TR 90-06
Transport of actinides and Tc through a bentonite backfill containing small quantities of iron, copper or minerals in inert atmosphere
Yngve Albinsson, Birgit Sätmark,
Ingemar Engkvist, W. Johansson
Department of Nuclear Chemistry,
Chalmers University of Technology, Gothenburg
April 1990

TR 90-07
Examination of reaction products on the surface of UO_2 fuel exposed to reactor coolant water during power operation
R. S. Forsyth, T. J. Jonsson, O. Mattsson
Studsvik Nuclear
March 1990

TR 90-08
Radiolytically induced oxidative dissolution of spent nuclear fuel
Lars Werme[1], Patrik Sellin[1], Roy Forsyth[2]
[1]Swedish Nuclear Fuel and waste Management Co (SKB)
[2]Studsvik Nuclear
May 1990

TR 90-09
Individual radiation doses from unit releases of long lived radionuclides
Ulla Bergström, Sture Nordlinder
Studsvik Nuclear
April 1990

TR 90-10
Outline of regional geology, mineralogy and geochemistry, Poços de Caldas, Minas Gerais, Brazil
H. D. Schorscher[1], M. E. Shea[2]
[1]University of Sao Paulo
[2]Battelle, Chicago
December 1990

TR 90-11
Mineralogy, petrology and geochemistry of the Poços de Caldas analogue study sites, Minas Gerais, Brazil
I: Osamu Utsumi uranium mine
N. Waber[1], H. D. Schorscher[2], A. B. MacKenzie[3], T. Peters[1]
[1]University of Bern
[2]University of Sao Paulo
[3]Scottish Universities Research & Reactor Centre (SURRC), Glasgow
December 1990

TR 90-12
Mineralogy, petrology and geochemistry of the Poços de Caldas analogue study sites, Minas Gerais, Brazil
II: Morro do Ferro
N. Waber
University of Bern
December 1990

TR 90-13
Isotopic geochemical characterisation of selected nepheline syenites and phonolites from the Poços de Caldas alkaline complex, Minas Gerais, Brazil
M. E. Shea
Battelle, Chicago
December 1990

TR 90-14
Geomorphological and hydrogeological features of the Poços de Caldas caldera, and the Osamu Utsumi mine and Morro do Ferro analogue study sites, Brazil
D. C. Holmes[1], A. E. Pitty[2], R. Noy[1]
[1]British Geological Survey, Keyworth
[2]INTERRA/ECL, Leicestershire, UK
December 1990

TR 90-15
Chemical and isotopic composition of groundwaters and their seasonal variability at the Osamu Utsumi and Morro do Ferro analogue study sites, Poços de Caldas, Brazil
D. K. Nordstrom[1], J. A. T. Smellie[2], M. Wolf[3]
[1]US Geological Survey, Menlo Park
[2]Conterra AB, Uppsala
[3]Gesellschaft für Strahlen- und Umweltforschung (GSF), Munich
December 1990

TR 90-16

Natural radionuclide and stable element studies of rock samples from the Osamu Utsumi mine and Morro do Ferro analogue study sites, Poços de Caldas, Brazil

A. B. MacKenzie[1], P. Linsalata[2], N. Miekeley[3], J. K. Osmond[4], D. B. Curtis[5]
[1]Scottish Universities Research & Reactor Centre (SURRC), Glasgow
[2]New York Medical Centre
[3]Catholic University of Rio de Janeiro (PUC)
[4]Florida State University
[5]Los Alamos National Laboratory
December 1990

TR 90-17

Natural series nuclide and rare earth element geochemistry of waters from the Osamu Utsumi mine and Morro do Ferro analogue study sites, Poços de Caldas, Brazil

N. Miekeley[1], O. Coutinho de Jesus[1], C-L Porto da Silveira[1], P. Linsalata[2], J. N. Andrews[3], J. K. Osmond[4]
[1]Catholic University of Rio de Janeiro (PUC)
[2]New York Medical Centre
[3]University of Bath
[4]Florida State University
December 1990

TR 90-18

Chemical and physical characterisation of suspended particles and colloids in waters from the Osamu Utsumi mine and Morro do Ferro analogue study sites, Poços de Caldas, Brazil

N. Miekeley[1], O. Coutinho de Jesus[1], C-L Porto da Silveira[1], C. Degueldre[2]
[1]Catholic University of Rio de Janeiro (PUC)
[2]PSI, Villingen, Switzerland
December 1990

TR 90-19

Microbiological analysis at the Osamu Utsumi mine and Morro do Ferro analogue study sites, Poços de Caldas, Brazil

J. West[1], A. Vialta[2], I. G. McKinley[3]
[1]British Geological Survey, Keyworth
[2]Uranio do Brasil, Poços de Caldas
[3]NAGRA, Baden, Switzerland
December 1990

TR 90-20

Testing of geochemical models in the Poços de Caldas analogue study

J. Bruno[1], J. E. Cross[2], J. Eikenberg[3], I. G. McKinley[4], D. Read[5], A. Sandino[1], P. Sellin[6]
[1]Royal Institute of Technology (KTH), Stockholm
[2]AERE, Harwell, UK
[3]PSI, Villingen, Switzerland
[4]NAGRA, Baden, Switzerland
[5]Atkins, ES, Epsom, UK
[6]Swedish Nuclear and Waste Management Co (SKB), Stockholm
December 1990

TR 90-21

Testing models of redox front migration and geochemistry at the Osamu Utsumi mine and Morro do Ferro analogue sites, Poços de Caldas, Brazil

J. Cross[1], A. Haworth[1], P. C. Lichtner[2], A. B. MacKenzi[3], L. Moreno[4], I. Neretnieks[4], D. K. Nordstrom[5], D. Read[6], L. Romero[4], S. M. Sharland[1], C. J. Tweed[1]
[1]AERE, Harwell, UK
[2]University of Bern
[3]Scottish Universities Research & Reactor Centre (SURRC), Glasgow
[4]Royal Institute of Technology (KTH), Stockholm
[5]US Geological Survey, Menlo Park
[6]Atkins ES, Epsom, UK
December 1990

TR 90-22

Near-field high temperature transport: Evidence from the genesis of the Osamu Utsumi uranium mine analogue site, Poços de Caldas, Brazil

L. M. Cathles[1], M. E. Shea[2]
[1]University of Cornell, New York
[2]Battelle, Chicago
December 1990

TR 90-23

Geochemical modelling of water-rock interactions at the Osamu Utsumi mine and Morro do Ferro analogue sites, Poços de Caldas, Brazil

D. K. Nordstrom[1], I. Puigdomenech[2], R. H. McNutt[3]
[1]US Geological Survey, Menlo Park
[2]Studsvik Nuclear, Sweden
[3]McMaster University, Ontario, Canada
December 1990

TR 90-24
The Poços de Caldas Project: Summary and implications for radioactive waste management
N. A. Chapman[1], I. G. McKinley[2], M. E. Shea[3], J. A. T. Smellie[4]
[1]INTERRA/ECL, Leicestershire, UK
[2]NAGRA, Baden, Switzerland
[3]Battelle, Chicago
[4]Conterra AB, Uppsala

TR 90-25
Kinetics of UO_2(s) dissolution reducing conditions: numerical modelling
I. Puigdomenech[1], I. Casas[2], J. Bruno[3]
[1]Studsvik AB, Nyköping, Sweden
[2]Department of Chemical Engineering, E.T.S.E.I.B. (U.P.C.), Barcelona, Spain
[3]Department of Inorganic Chemistry, The Royal Institute of Technology, Stockholm, Sweden
May 1990

TR 90-26
The effect from the number of cells, pH and lanthanide concentration on the sorption of promethium on gramnegative bacterium (Shewanella Putrefaciens)
Karsten Pedersen[1], Yngve Albinsson[2]
[1]University of Göteborg, Department of General and Marine Microbiology, Gothenburg, Sweden
[2]Chalmers University of Technology, Department of Nuclear Chemistry, Gothenburg, Sweden
June 1990

TR 90-27
Isolation and characterization of humics from natural waters
B. Allard[1], I. Arsenie[1], H. Borén[1], J. Ephraim[1], G. Gårdhammar[2], C. Pettersson[1]
[1]Department of Water and Environmental Studies, Linköping University, Linköping, Sweden
[2]Department of Chemistry, Linköping University, Linköping, Sweden
May 1990

TR 90-28
Complex forming properties of natural organic acids. Part 2. Complexes with iron and calcium
James H. Ephraim[1], Andrew S. Mathuthu[2], Jacob A. Marinsky[3]
[1]Department of Water in Environment and Society, Linköping University, Linköping, Sweden
[2]Chemistry department, University of Zimbabwe, Harare, Zimbabwe
[3]Chemistry Department, State University of New York at Buffalo, Buffalo, NY, USA
July 1990

TR 90-29
Characterization of humic substances from deep groundwaters in granitic bedrock in Sweden
C. Pettersson, J. Ephraim, B. Allard, H. Borén
Department of Water and Environmental Studies, Linköping University, Linköping, Sweden
June 1990

TR 90-30
The earthquakes of the Baltic shield
Ragnar Slunga
Swedish National Defence Research Institute
June 1990

TR 90-31
Near-field performance of the advanced cold process canister
Lars Werme
Swedish Nuclear Fuel and Waste Management Co (SKB)
September 1990

TR 90-32
Radioclide transport paths in the nearfield – a KBS-3 concept study
Roland Pusch
Clay Technology AB and Lund University of Technology
July 1990

TR 90-33
PLAN 90
Costs for management of the radioactive waste from nuclear power production
Swedish Nuclear Fuel and Waste Management Co (SKB)
June 1990

TR 90-34
GEOTAB: User's guide – Version 1.8.2
Ergodata
October 1990

TR 90-35
Dose conversion factors for major nuclides within high level waste
Ulla Bergström, Sture Nordlinder
Studsvik Nuclear
November 1990

TR 90-36
Sensitivity analysis of groundwater flow Licentiate thesis
Yung-Bing Bao
Royal Institute of Technology, Department of Land and Water Resources, Stockholm, Sweden
December 1990

TR 90-37
The influence of fracture mineral/ groundwater interaction on the mobility of U, Th, REE and other trace elements
Ove Landström[1], Eva-Lena Tullborg[2]
[1]Studsvik AB, Nyköping
[2]SGAB, Gothenburg
December 1990

TR 90-38
Solute transport in fractured rock – Applications to radionuclide waste repositories
Ivars Neretnieks
Department of Chemical Engineering,
Royal Institute of Technology, Stockholm
December 1990

TR 90-39
Modelling of the movement of the redox front in the uranium mine in Poços de Caldas, Brazil
Leonardo Romero, Luis Moreno, Ivars Neretnieks
Royal Institute of Technology, Stockholm
June 1990

TR 90-40
Distinct element modelling of the rock mass response to glaciation at Finnsjön, central Sweden
Lars Rosengren[1], Ove Stephansson[2]
[1]Itasca Geomekanik AB, Falun, Sweden
[2]Division of Rock Mechanics, Luleå University of Technology, Luleå, Sweden
December 1990

TR 90-41
Ground water in crystalline bedrock
Kai Palmqvist
BERGAB-Berggeologiska Undersökningar AB
June 1990

TR 90-42
Development of clay characterization methods for use in repository design with application to a natural Ca bentonite clay containing a redox front
Ola Karnland, Roland Pusch
Clay Technology AB, Lund
December 1990

TR 90-43
GMM – A general microstructural model for qualitative and quantitative studies of smectite clays
Roland Pusch, Ola Karnland, Harald Hökmark
Clay Technology AB, Lund
December 1990

TR 90-44
Preliminary report on longevity of montmorillonite clay under repository-related conditions
Roland Pusch, Ola Karnland
Clay Technology AB, Lund
December 1990